This is a non-peer reviewed preprint. The authors welcome comments!

Do 3D Dynamic Rupture Models Capture the Variability in Long-Period Velocity Pulses? Insights from the 2023 M_w 7.8 Kahramanmaraş Earthquake

Rachel Preca Trapani[1], Mathilde Marchandon[1], Kadek Hendrawan Palgunadi[3,4], Baoning Wu[2], Ming-Hsuan Yen[5], Fabrice Cotton[5], Alice-Agnes Gabriel[2,1]

[1]Department of Earth and Environmental Sciences, Ludwig-Maximilian-Universität (LMU), Munich, Germany
[2]Scripps Institution of Oceanography, UC San Diego, La Jolla, CA, USA
[3]Swiss Seismological Service (SED), ETH Zürich, Switzerland
[4]Department of Geophysical Engineering, Institut Teknologi Sepuluh Nopember, Indonesia
[5]GFZ, Helmholtz Centre, Potsdam, Germany

Key Points:

- We test how multi-scale fault roughness, heterogeneous friction and supershear initiation affect long-period velocity pulse variability.
- Our models reproduce pulse amplitude variability well but do not fully capture pulse orientation and pulse period variability.
- Local supershear rupture speeds exert the strongest control on modelled pulse orientation and period.

Corresponding author: Rachel Preca Trapani, R.Preca@lmu.de

Abstract

Capturing ground motion variability, especially in near-fault long-period velocity pulses, is a key challenge for seismic hazard assessment. Observations from the 2023 Mw 7.8 Kahramanmaraş, Türkiye earthquake reveal substantial variability in the near-fault pulses' orientation, period, and amplitude. Physics-based dynamic rupture simulations provide a unique framework for investigating the physical mechanisms responsible for this variability. Here, we systematically investigate the effect of fault geometry and on-fault heterogeneities in a suite of 3D dynamic rupture simulations of the 2023 Mw 7.8 Kahramanmaraş, Türkiye, earthquake. We compare dynamic rupture scenarios that separately incorporate large-scale fault waviness, fractal fault roughness, heterogeneous critical slip-weakening distance, heterogeneous dynamic friction, and supershear versus subshear initiation, each resolving up to at least ~ 1 Hz. We systematically analyse the influence on rupture dynamics, frequency content, and long-period pulse variability, while ensuring all models have comparable seismic moment rate release. While all models capture near-fault pulse amplitude variability, supershear initiation and fracture energy heterogeneity exert the strongest influence on pulse period and orientation. Despite added complexity, most modelled pulses remain predominantly fault-normal, contrasting observed broader ranges of orientations, but supershear rupture speed locally increases variability in pulse orientation. The four other distinct on-fault heterogeneities all fail to broaden the modelled orientation distribution, suggesting that this aspect of near-fault pulse variability is not controlled by on-fault complexity alone. It points instead to processes beyond main-fault rupture, including off-fault damage, fault zone structure or site effects, as necessary ingredients for realistic, non-ergodic ground-motion models and physics-based seismic hazard assessment.

Plain Language Summary

Earthquake shaking can vary a lot depending on how the fault moves, the path seismic waves take, and local ground conditions. Traditional models often simplify these factors and struggle to capture the full range of shaking patterns. In this study, we use advanced 3D computer simulations to examine the 2023 Kahramanmaraş earthquake. We look at how features, such as fault shape, multi-scale roughness, variations in fault friction, and the speed at which the rupture starts, affect the resulting ground motion. We find that while the overall energy release and frequency content of the shaking are relatively stable, certain factors, such as very fast rupture speeds and variations in the fault's resistance to slipping, strongly influence the size, duration, and direction of a specific type of ground shaking known as a long-period velocity pulse. Despite these complexities, the strongest shaking tends to remain aligned roughly perpendicular to the fault. These findings therefore improve our understanding of how earthquake shaking varies, which is important for better predicting earthquake impacts and improving hazard assessments.

1 Introduction

Ground motion variability stems from the non-linear combination of source, path and site effects, which can be difficult to capture through empirical ground motion models (GMMs) (Bommer et al., 2004). This challenge arises as they often rely on simplified empirical and statistical relationships and are constrained by limited near-fault data (Strasser et al., 2009; Somerville et al., 1997; Lin et al., 2011; Bray & Rodriguez-Marek, 2004). Data-constrained 3D dynamic rupture simulations can help address this challenge by simulating realistic, non-ergodic ground motions in a self-consistent way (Aochi & Madariaga, 2003; Harris & Abrahamson, 2014; Wollherr et al., 2019; Z. Hu et al., 2022; Yao & Yang, 2023; Gallovič & Ľ. Valentová, 2023), while reproducing a variety of geodetic, seismic and tsunami data (e.g., Taufiqurrahman et al., 2022; Tinti et al., 2021).

Velocity pulses are long-period and large-amplitude near-fault ground motions, which tend to have highly variable properties when observed within a 20 km distance from the

fault (Withers, Olsen, Day, & Shi, 2019; Baltzopoulos et al., 2023; Yen et al., 2025). Such velocity pulses have been shown to correlate with substantial damage but are challenging to account for in seismic hazard assessment (e.g., Heaton et al., 1995; Strasser & Bommer, 2009; Chioccarelli & Iervolino, 2010; F. Wu et al., 2023; Ertuncay & Costa, 2024). They are mainly due to two distinct source effects (Türker et al., 2023): (i) rupture direction relative to the site, i.e. forward or backward directivity, and (ii) permanent ground displacements known as fling-step effects. They represent the cumulative rupture effect concentrated into a single, high-energy arrival and, contrary to earlier assumptions, occur in multiple orientations beyond the fault-normal direction (Shahi & Baker, 2014; Chang et al., 2025).

Directivity pulses occur when the rupture propagates towards (or away from) a recording site, and have been observed in multiple seismic events, such as the 2016 Meinong, Taiwan earthquake (Lee et al., 2016), the 1999 Chi-Chi earthquake (Akkar & Gülkan, 2002), and the 1995 Kobe earthquake (Strasser & Bommer, 2009). They are typically observed as two-sided, large-amplitude pulses in recorded near-fault velocity waveforms. In contrast, fling-step pulses are characterised by a one-sided large-amplitude velocity pulse. In practice, pulse shapes are more complex and can include ambiguous or multiple-sided forms, occurring at a range of orientations (Chang et al., 2025). Site effects, such as resonance effects, can amplify pulse-like signals, and heterogeneities in fault properties and geometric complexities during dynamic rupture may add variability to their characteristics (Ertuncay & Costa, 2024; Yen et al., 2025).

The 2023 Kahramanmaraş Türkiye earthquake sequence was devastating, causing widespread severe damage and tens of thousands of fatalities (Reitman, Briggs, Barnhart, Hatem, et al., 2023). It comprised a doublet of large earthquakes, the M_w 7.8 Pazarcık and the M_w 7.7 Elbistan events. The Pazarcık earthquake was a left-lateral strike-slip rupture that nucleated on the Nurdağı-Pazarcık splay Fault (NPF) at $\sim$ 10 km depth, before branching onto the East Anatolian Fault (EAF) and rupturing a total length of $\sim$350 km (Figure 1a, Jia et al. (2023); Melgar et al. (2023); Delouis et al. (2024)). About 9 hours later, the Elbistan earthquake, also a left-lateral strike-slip event, nucleated 90 km north of the EAF at 7 km depth and ruptured $\sim$ 170 km of the Sürgü-Çardak Fault (SCF) (Mai et al., 2023; Barbot et al., 2023; Chang et al., 2025).

The earthquake doublet struck densely populated regions, causing structural damage, including failure of some recently constructed buildings (Ertuncay & Costa, 2024). Several studies suggest that near-fault velocity pulses may have contributed to this damage, although their role and prevalence remain debated (e.g., Silahtar et al., 2025; Varolgüneş, 2026; Chang et al., 2025). Observed ground motions in parts of the affected region exceeded the demands anticipated by building codes, particularly at longer periods where empirical models tend to underestimate response spectra (Baker, 2007; Ozkula et al., 2023; Akinci et al., 2025). It was a complex rupture sequence that potentially reached supershear rupture speeds at different fault segments (Abdelmeguid et al., 2023; Ren et al., 2024; Delouis et al., 2024; Gabriel et al., 2023; Rosakis et al., 2025). Supershear rupture speeds have been suggested to be responsible for the plenitude of impulsive motion (Ertuncay & Costa, 2024), as have other source mechanisms and near-fault complexities (Graves & Pitarka, 2016; Withers, Olsen, Day, & Shi, 2019; Lozos et al., 2025).

A recent analysis by Yen et al. (2025) highlights the lack of pulse property variability captured in dynamic rupture models of the 2023 Kahramanmaraş earthquake (Figure 1b and c, (Jia et al., 2023)). Recent near-fault strong-motion analysis by B. Wu et al. (2025) of the M_w 7.8 Kahramanmaraş earthquake shows a loss of horizontal polarity and reduced between-component coherence, implicating small-scale source and near-fault structural processes not captured by dynamic rupture models either. This motivates this study focusing on the physical controls of velocity pulses and high-frequency radiation, aiming to advance realistic, non-ergodic ground motion models and physics-based seismic hazard assessment.

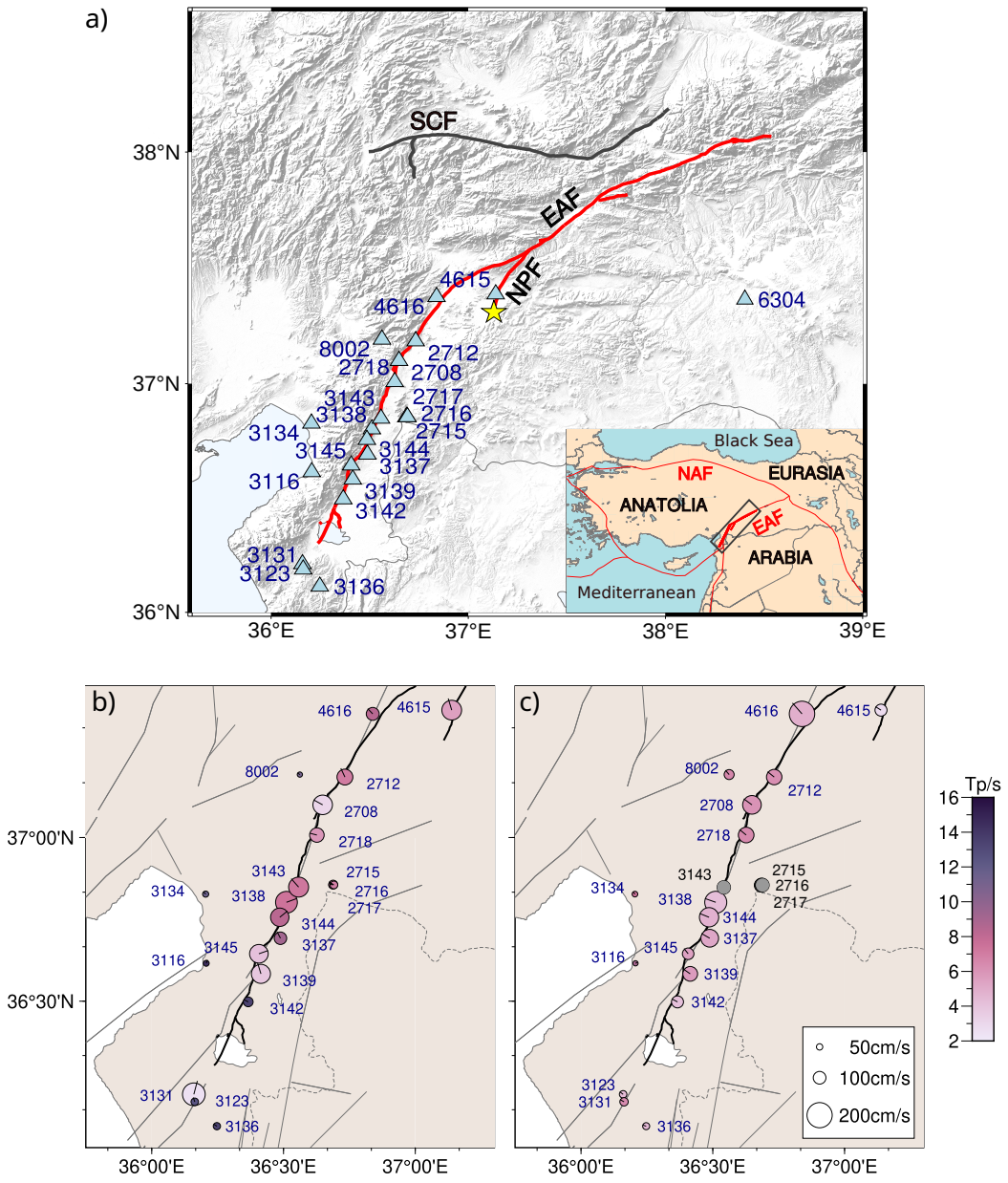


Figure 1: a) The study area highlighting the 2023 M_w 7.8 Kahramanmaraş earthquake surface rupture (red lines, (Reitman, Briggs, Barnhart, Jobe, et al., 2023)). The earthquake initiated on the Nurdağı-Pazarcık splay Fault (NPF) and continued onto the East Anatolian Fault (EAF) in a bilateral manner. For completeness, the grey lines show the surface rupture of the 2023 Mw 7.7 Elbistan earthquake that broke the Sürgü–Çardak Fault (SCF, (Reitman, Briggs, Barnhart, Jobe, et al., 2023)). The yellow star depicts the AFAD epicentre, and the blue triangles represent the AFAD near-fault stations (see Open Research Section) used in this study. The inset shows the regional tectonics and major plate boundary faults (red lines), including the North Anatolian Fault (NAF) and EAF. The rectangle highlights the study area. b) Reproduction of Yen et al. (2025)'s results showing long-period near-fault pulse properties extracted from observational data (ESM, Mascandola et al. (2026)) and c) from the dynamic rupture model of (Jia et al., 2023) for the 2023 Kahramanmaraş earthquake. The circle size corresponds to the peak rotated velocity (PRV), the colour corresponds to the pulse period (T_p), and the lines within the circles represent the pulse orientation. Black lines show the surface rupture trace (Reitman, Briggs, Barnhart, Jobe, et al., 2023), grey lines show the mapped active faults (Styron & Pagani, 2020), and dashed lines show the boundary between Türkiye and Syria. See also Figure S1.

2 Observations of Long-Period Pulses During the 2023 M_w 7.8 Kahramanmaraş Earthquake

The observational waveforms of the 2023 Mw 7.8 Kahramanmaraş earthquake that we retrieved are 3-component accelerograms from the ESM database (Mascandola et al., 2026). The waveforms were preprocessed by ESM following (Paolucci et al., 2011). These were bandpass filtered between 0.03 and 40 Hz, baseline corrected, tapered and linearly de-trended. Analysis of the seismic velocity records reveals that many near-fault stations exhibit pronounced pulse-like ground motion (Figures S6–S12; Ertuncay & Costa, 2024; Akinci et al., 2025; J. Hu et al., 2025; Yen et al., 2025). At several stations (e.g., 4615, 4616, 3142 and 3143), a large fraction of the seismic energy is concentrated within a single dominant impulse occurring early in the ground motion record, rather than spread out over time. Following pulse identification using the procedure of Shahi and Baker (2014), pulse-like motion was detected at 21 near-fault stations. The extracted pulses display large variability in their properties (Yen et al., 2025, Figures 1b, S13–S31). Peak rotated velocities range from approximately 40 to 180 cm/s, pulse periods from about 2 to 16 s, corresponding to wavelengths of $\sim 4 - 64$ km, assuming characteristic wave speeds of $2 - 4$ km/s, and pulse orientations span a wide range (approximately $\pm 25°$ to $\pm 75°$), indicating that the strongest pulse is not systematically aligned with a single direction.

3 Methods

This section details the setup of the reference 3D dynamic rupture model (Model 1), which forms the basis for all subsequent model variants. We first briefly introduce the reference model (section 3.1), then detail the numerical method used to perform the simulations (section 3.2), followed by the definition of the fault geometry (section 3.3), computational mesh characteristics (section 3.4), and on- and off-fault dynamic rupture model properties. This includes the frictional properties (section 3.5), the initial stress distribution (section 3.6), the nucleation procedure (section 3.7), and the off-fault medium properties (section 3.8). The parameterisation of the reference model is summarised in Table 1. Finally, we describe the velocity pulse analysis applied to the observed and simulated ground motions in Section 3.9.

3.1 3D Dynamic Rupture Model Setup

We focus on dynamic rupture models of the M_w 7.8 Kahramanmaraş earthquake, the first event of the 2023 Türkiye doublet. Our 3D dynamic rupture models are based on the setup presented in Gabriel et al. (2023). Their models link 3D dynamic rupture scenarios of the M_w 7.8 Pazarcık earthquake and the M_w 7.7 Elbistan earthquake, such that each earthquake scenario is dynamically consistent with respective seismic, geodetic and optical observations. In contrast to the dynamic rupture models in Jia et al. (2023), no smaller-scale initial prestress or fault strength heterogeneity is prescribed in the reference model. The M_w 7.8 earthquake scenario, hereafter referred to as the "reference model" (Model 1), is characterised by three distinct rupture phases. The rupture nucleates as a subshear crack-like rupture on the NPF, it crosses the NPF-EAF junction, where it almost arrests, continuing in the northeast direction before rupturing to the southwest after a pronounced delay.

In this study, in addition to the reference model (Model 1), we conduct and analyse a set of new 3D dynamic rupture models, each differing from Model 1 by one added source of physical or geometrical complexity (Figure 2), exploring a total of six models in the main text and an additional four models in the Supplementary Information. These variants will be referred to as: Model 2 ("supershear initiation model"): includes supershear rupture speed initiation, from Gabriel et al. (2023); Model 3 ("roughness model"): includes multi-scale on-fault roughness; Model 4 ("D_c model"): includes a heterogeneous distribution of the critical slip-weakening distance (D_c); Model 5 ("μ_d model"): includes a heterogeneous distribution

of the dynamic friction coefficient (μ_d); and Model 6 ("waviness model"): includes what we refer to as large-scale fault waviness, i.e. large-wavelength geometric undulations of the fault surface. The specific parametrisation of each model variant is detailed in Section 4. Our model modifications are motivated by the need to understand what drives the generation and variability of long-period velocity pulses ranging between periods of 2 s and 16 s (corresponding to frequencies of $\sim$ 0.06–0.5 Hz) (e.g., Yen et al., 2021; Türker et al., 2023; Yen et al., 2025). Such heterogeneities may also influence the higher-frequency content (e.g., Vallée et al., 2008; Shi & Day, 2013; B. Wu et al., 2025), which in this study refers to frequencies of 0.5 – 1 Hz. The upper limit of 1 Hz is resolved throughout the computational domain, including its coarser regions (Section 5.3).

In all six models considered in this study, rupture is initiated on the NPF at the hypocentral location of the Disaster and Emergency Management Authority (AFAD) of Türkiye (see Open Research Section) (37.043°N, 37.288°E) and then ruptures across the EAF (Figure 1a). All models share the same numerical setup, including the computational mesh and nucleation procedure. Exceptions include the larger meshes required by Models 3 and 6 (Section 4.2) and minor adjustments to the prestress ratio and initial stress in Models 3, 5, and 6 to ensure comparable dynamic rupture propagation across the fault system (Section 3.6).

3.2 Numerical Method

We use the open-source software package SeisSol (Gabriel et al., 2025) to solve the 3D spontaneous dynamic rupture and seismic wave propagation problem. SeisSol uses the Arbitrary high-order accurate DERivative Discontinuous Galerkin (ADER-DG) finite element method (e.g., Dumbser & Käser, 2006; Pelties et al., 2012). SeisSol combines non-linear on-fault frictional failure and high-order accurate propagation of seismic waves and is optimised for modern high-performance computing infrastructure (e.g., Breuer et al., 2014; Heinecke et al., 2014; Uphoff et al., 2017; Krenz et al., 2021). It has been verified through several dynamic rupture benchmark problems (Pelties et al., 2014; Harris et al., 2018; Taufiqurrahman et al., 2022; Vyas et al., 2023).

3.3 Fault Geometry

We adopt the same fault geometries as in Gabriel et al. (2023), which are informed by space geodesy and seismicity, including aftershock locations. This fault system geometry consists of five intersecting segments with a dip of 90° for the NPF and the EAF, reaching a depth of 20 km, that capture large-scale geometrical complexities, such as fault bends, step-overs and secondary segments, across which the earthquake propagated (Figure 1b).

3.4 Mesh and Resolution

The meshes used in this study are generated using SimModeler 11.0 (Simmetrix Inc., 2017) and PUMGen. The structural model is first constructed in SimModeler and then discretised into unstructured tetrahedral elements of variable size using PUMGen. PUMGen embeds MeshSim from SimMetrix, the underlying mesh generator of SimModeler and exports the mesh into the efficient Parallel Unstructured Mesh Library (PUML) format used by SeisSol. All models include the ground surface topography from the Shuttle Radar Topography Mission (SRTM) Digital Elevation Model (DEM) (Farr et al., 2007) downsampled at 450 m. The smallest on-fault element edge length is $h = 300$ m in all models, while element sizes gradually increase with distance from the faults. A high-resolution region of $400 \times 200 \times 25$ km is defined for all models, encompassing the entire fault system together with the local strong-motion stations. Within this region, we resolve seismic wave propagation up to frequencies of at least 1 Hz.

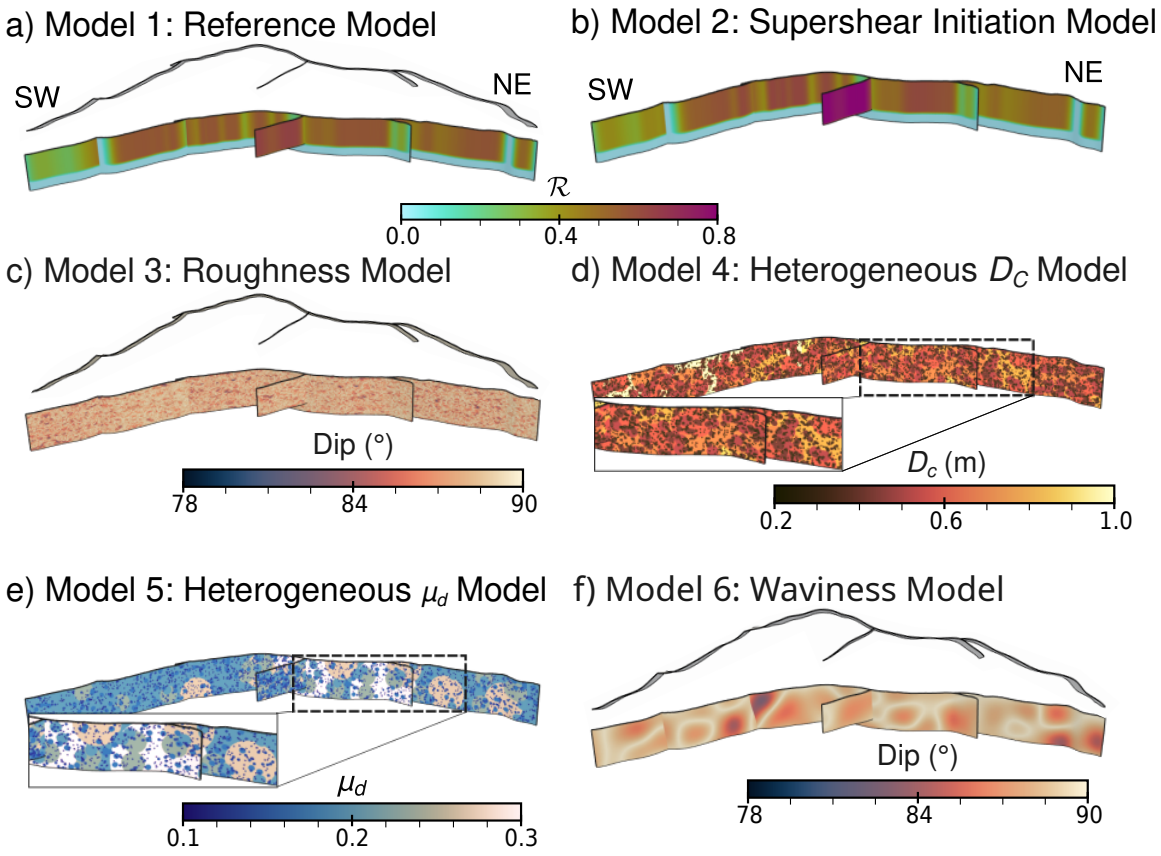


Figure 2: Overview of the reference and five new dynamic rupture models of the 2023 M_w 7.8 Kahramanmaraş earthquake analysed in this study. a) Model 1: the reference model by Gabriel et al. (2023); b) Model 2: supershear initiation c) Model 3: multi-scale fault roughness d) Model 4: heterogeneous D_c, where the inset shows a close-up of the heterogeneities applied e) Model 5: heterogeneous μ_d, the inset also showing a close-up of the heterogeneities f) Model 6: large-scale fault waviness.

The reference model and models 2, 4, and 5 share the same unstructured tetrahedral mesh, consisting of ∼30 million elements. In contrast, Models 3 and 6, which incorporate fault roughness and large-scale fault waviness, require re-meshing to represent the more complex fault geometries whilst maintaining the same on-fault resolution used in the other models. This involves incorporating on-fault geometrical complexities whilst preserving the map-scale fault trace geometry across all models. For these two models, we generate a larger mesh consisting of ∼ 50 million elements that covers a slightly larger area than the other models. The larger domain size is not required by the fault roughness or waviness, but results from the larger bounding area used when clipping these meshes during the meshing procedure. The meshes adapt to the band-limited self-similar fractal fault surfaces (see Sections 4.2 and 4.5, and Table S1).

3.5 Fault Strength and Friction

In all simulations, fault strength, τ, is governed by a linear slip-weakening friction law (Ida, 1972; Palmer et al., 1973; D. J. Andrews, 1976; Day, 1982). The fault strength is defined as:

$$\tau = c + \mu\sigma_n' \,. \tag{1}$$

where c is the frictional on-fault cohesion, the part of fault strength that does not depend on effective normal stress, μ is the friction coefficient, and σ_n' is the effective normal stress accounting for pore fluid pressure P_f. A fault begins to slip when the shear stress locally exceeds the peak fault strength τ_p. The fault strength τ then decreases linearly from a static peak value, τ_p, to a dynamic level, τ_r, over a critical slip-weakening distance, D_c, as:

$$\tau = \begin{cases} \tau_p - (\tau_p - \tau_r)\frac{u}{D_c}, & u < D_c \,, \\ \tau_r, & u \geq D_c \,. \end{cases} \tag{2}$$

where $\tau_p = c + \mu_s\sigma_n'$ and $\tau_r = \mu_d\sigma_n'$. μ_s is the static coefficient of friction, μ_d is the dynamic coefficient of friction, and u is the accumulated fault slip. Therefore, μ in Equation 1 is equal to μ_s before slip and to μ_d after slipping the critical slip-weakening distance, D_c.

In the reference model, the static coefficient of friction is set to $\mu_s = 0.6$, the dynamic coefficient of friction to $\mu_d = 0.2$ and the critical slip-weakening distance to $D_c = 0.5$ m (see Table 1). We set the on-fault frictional cohesion c to 0.5 MPa below 6 km depth and increase it linearly up to 1.5 MPa at a depth of 0 km to prevent unrealistically low shallow fault strength (Gabriel et al., 2023).

3.6 Initial Stress

In all models, we expose the fault system to an Andersonian stress regime representing strike-slip faulting, i.e. the intermediate compressive stress σ_2 is vertical (Anderson, 1905, 1951). As in Gabriel et al. (2023), the orientation of the maximum horizontal compressive stress, SH_{max}, is variable and constrained by a regional stress tensor inversion from focal mechanisms (Güvercin et al., 2022) (Figure S2a). The magnitudes of the principal stresses σ_1, σ_2, and σ_3 (with $\sigma_1 > \sigma_2 > \sigma_3$) are controlled by the relative prestress level $\mathcal{R}_0$ of a (virtual) optimally oriented fault, the effective lithostatic stress σ_{zz}' and the stress shape ratio ν (Ulrich et al., 2019).

Up to 6 km depth, the effective lithostatic stress σ_{zz}' increases linearly with depth and is equal to the lithostatic stress σ_{zz} reduced by the effect of P_f. P_f is assumed proportional to the lithostatic stress, $P_f = \gamma\sigma_{zz}$, with γ the fluid-pressure ratio (Ulrich et al., 2019):

$$\sigma_{zz}(z) = \rho\, g\, z\,. \tag{3}$$

$$\sigma'_{zz}(z) = (1-\gamma)\,\sigma_{zz}\,. \tag{4}$$

where $\rho = 2670$ kg m^{-3} is the overburden rock density, g is the acceleration due to gravity, and z is the depth. We assume an over-pressured pore fluid state with γ=0.66. Although observations constraining the pore fluid pressure at seismogenic depths are not readily available, this assumption is helpful to reproduce realistic stress drop as well as the observed amount of surface slip (Ulrich et al., 2019; Biemiller et al., 2022). Below 6 km depth, the pore fluid pressure gradient mirrors the lithostatic stress gradient, leading to a constant effective lithostatic stress of 52 MPa (Rice, 1992; Suppe, 2014; Madden et al., 2022).

From the orientation and magnitude of the three principal stress components, the full 3D initial stress tensor is computed. The shear and normal stresses acting on the non-planar fault surfaces are then obtained by projecting the resulting tensor onto the non-planar fault segments, naturally producing spatial variations in τ_0 and σ_n.

Local fault strength and dynamic stress drop are governed by the relative prestress ratio, $\mathcal{R}$ (Aochi & Madariaga, 2003; Ulrich et al., 2019), which varies across the fault system (Figure S3). $\mathcal{R}$ represents the fault-local ratio of the maximum potential stress drop over the frictional breakdown strength drop, as:

$$\mathcal{R} = \frac{\tau - \mu_d \sigma'_n}{(\mu_s - \mu_d)\sigma'_n}\,. \tag{5}$$

When $\mathcal{R}$=1, the fault is critically stressed and optimally oriented. The $\mathcal{R}$ ratio is related to the seismic S ratio (Das & Aki, 1977) as $S = 1/\mathcal{R} - 1$. We prescribe $\mathcal{R}_0$, the maximum value of $\mathcal{R}$ of an optimally oriented fault segment in a given stress regime. The fault local $\mathcal{R} \leq \mathcal{R}_0$ varies with fault geometry, initial stresses and frictional heterogeneities (Figure S3). In the reference model, $\mathcal{R}_0 = 0.62$ across the NPF and varies across the EAF (Figure 3a). Figures 3b–g illustrate the prescribed $\mathcal{R}_0$ in our six dynamic rupture models.

Parameter	Notation	Reference Model
Static friction coefficient	μ_s	0.6
Dynamic friction coefficient	μ_d	0.2
Critical slip weakening distance	D_c [m]	0.5
Maximum cohesion	c [MPa]	1.5

Table 1: Dynamic rupture parameter values for the reference model.

3.7 Nucleation

Dynamic rupture simulations require prescribed nucleation in order to initiate spontaneous rupture propagation (e.g., Bizzarri, 2010; Galis et al., 2015). We use a smooth nucleation procedure for all simulations that involves a forced rupture across a prescribed patch of 2 km radius (Gabriel et al., 2012; Harris et al., 2018). At the given nucleation time, the friction coefficient is artificially reduced to its dynamic value. The nucleation then grows smoothly in time as a kinematically driven subshear crack-like rupture with rupture

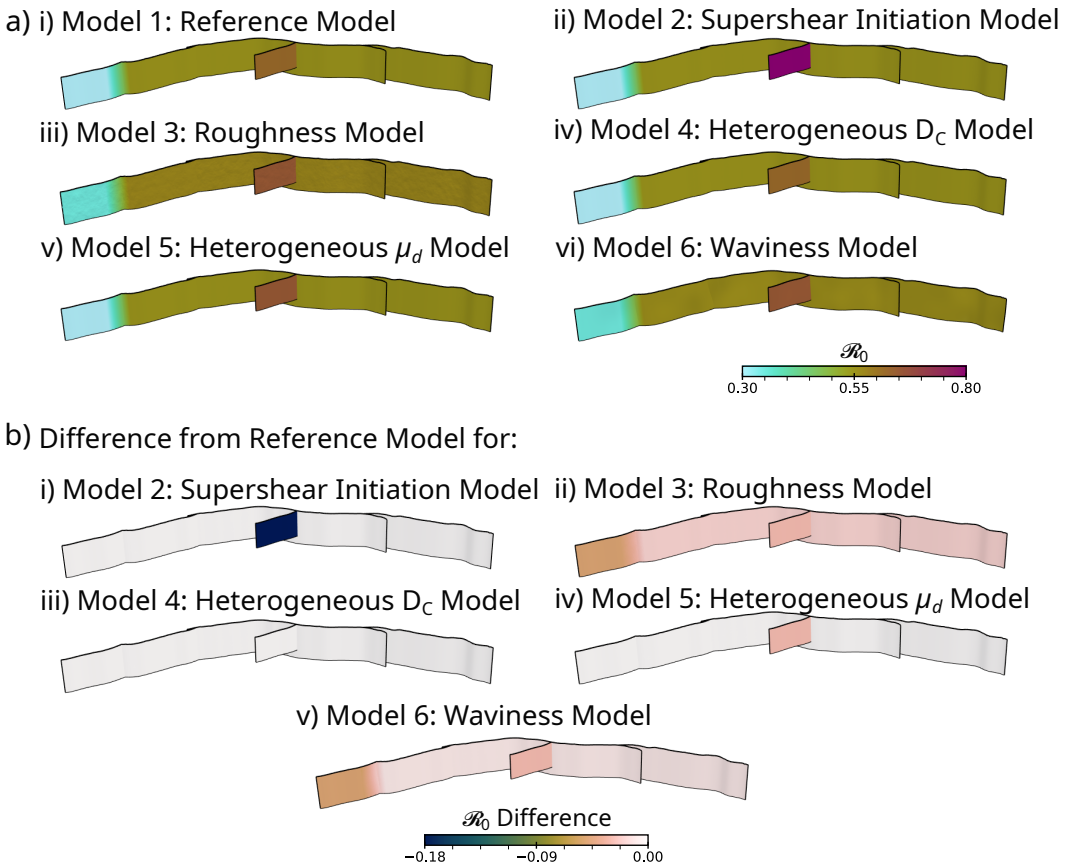


Figure 3: a) $\mathcal{R}_0$ for all six models. b) The difference in $\mathcal{R}_0$ between the reference model and the models with added complexities (Difference = Reference Model - Complexity Model).

speed $V_r \sim 2400$ m/s (Gabriel et al., 2023). All models prescribe nucleation at the AFAD hypocentral location.

3.8 Velocity Model and Off-fault Plasticity

The elastic properties of the medium are constrained by the 1D velocity model of Güvercin et al. (2022). We do not include viscoelastic attenuation. Table S2 details the variation in P-wave c_p and S-wave c_s velocities with depth.

We include non-associative Drucker-Prager off-fault plasticity in all dynamic rupture models (D. Andrews, 2005; Wollherr et al., 2018), without changing its parameterisation between models. The plastic cohesion, C_{plast}, controls how much stress the off-fault medium can withstand before deforming plastically. We follow previous work (e.g., Withers, Olsen, Shi, & Day, 2019; Yeh & Olsen, 2024; Li et al., 2025; Schliwa et al., 2025) and define plastic cohesion to vary with the 1D depth-dependent shear modulus $\mu(z)$, following the plastic cohesion "model 3" described in Roten et al. (2014) for weak rocks, as:

$$C_{plast} = 10^{-4}\mu(z)\,. \tag{6}$$

This description allows for a range of cohesion values between 0 and 10 MPa that are observed in laboratory experiments and are commonly used in dynamic rupture studies in nonlinear media (e.g., D. Andrews, 2005; Dunham et al., 2011), and being depth dependent. At near-surface depths shallower than 2 km, where confinement stresses are low, we taper plastic cohesion to $C_{plast} = 4.85$ MPa as:

$$C_{plast} = 2 \times 10^{-4} \times \max\left(\mu(z),\, 2 \times 10^{10}\right)\,. \tag{7}$$

This tapering is applied to achieve a good match between the measured and modelled surface fault offsets (Gabriel et al., 2023). Models without the tapering (i.e. that assume a lower plastic cohesion value near the surface) underestimate the slip at shallow depths. For numerical reasons (D. Andrews, 2005), the initiation of plastic yielding is governed by viscoplastic relaxation, allowing stress to relax gradually over a constant timescale $T_v = 0.05$ s, independent of spatial discretisation (Wollherr et al., 2018).

We note that off-fault plastic deformation depends on the initial stress state in the volume, which varies slightly between models 2, 4 and 3, 5 and 6. In addition, fault roughness and fault waviness will generate enhanced off-fault plasticity compared to planar fault models (e.g., Dunham et al., 2011). Analysing these differences is beyond the scope of this study and should be addressed in future work.

3.9 Velocity Pulse Analysis

We analyse near-fault, long-period velocity pulses following Shahi and Baker (2014). Their wavelet-based algorithm searches for pulse-like motion in either observed or simulated velocity time histories. This method is therefore capable of classifying observed and modelled near-fault ground motion through a quantitative and reproducible classification (e.g., Yen et al., 2025; Akinci et al., 2025; J. Hu et al., 2025; Yucel et al., 2026) and has been used as an established analysis tool in previous studies (e.g., Panella et al., 2017; Kohrangi et al., 2019; Ertuncay & Costa, 2024). This algorithm identifies ground motions in any orientation most likely to contain directivity pulses by performing a two-component wavelet transform to produce coefficients for every orientation. The corresponding wavelet coefficients are used to extract up to five candidate pulses from the velocity time histories at a given station. The algorithm then classifies the candidate pulses as "pulse-like" or "non-pulse-like" according to the defined threshold, which is related to the peak velocity of the record (Shahi & Baker, 2014). Applying this method to the near-field synthetics of our dynamic rupture models

allows us to account for potential pulses in any orientation, consistent with observational evidence that pulse-like motion is not only confined to the fault-normal direction (Somerville et al., 1997).

In more detail, the discrete wavelet transform is applied to the two horizontal, orthogonal components of the ground motion time histories to obtain wavelet coefficients. These coefficients are formed by representing the signal as a sum of scaled and translated Daubechies mother wavelets (Daubechies, 1993) in the time-frequency domain. This decomposition reveals how strongly each wavelet matches the signal at different times and scales, thereby indicating which frequencies dominate at which points in the record. This means that large coefficients indicate concentrated energy in a narrow time-frequency region, which is characteristic of a strong pulse. Using the coefficients of the two orthogonal components, the maximum wavelet amplitude is efficiently computed across all orientations. The orientation at which this maximum occurs is interpreted as the direction most likely to contain a pulse. The two horizontal components are then rotated into this orientation. The rotated single signal is referred to as the "original signal", following (Shahi & Baker, 2014; Yen et al., 2025). From the original rotated signal, the peak velocity is extracted, referred to here as the "peak rotated velocity (PRV)", followed by a candidate pulse (see Figure S4) to obtain its properties, such as pulse amplitude, period (T_p), and orientation. We caution not to mistake the PRV for the pulse amplitude. The pulse extraction workflow is depicted in Figure 4, where we highlight the difference between the peak velocity of the original rotated signal (PRV), which is what is presented in the reference maps in Figures 1b and c, and the extracted pulse amplitude. Note that the rest of this study explores the behaviour of the pulse amplitude and not the PRV. This procedure is then repeated on the original signal without the initially extracted pulse signal to identify up to five non-overlapping candidate pulses, ensuring that potential pulses at different times or frequencies are also captured.

The "pulse criterion" defined by Shahi and Baker (2014) is then calculated for each identified candidate pulse using a nonlinear Support Vector Machine (SVM)–based pulse indicator, combined with an early-arrival criterion to remove late-arriving pulses. This pulse criterion ranks each candidate pulse. Only the single top-ranked pulse-like identified candidate is retained. As described in Shahi and Baker (2014), the pulse classification is based on the pulse indicator (PI), which combines (i) the energy ratio of the residual to the original signal (ER), (ii) the peak velocity ratio of the residual and original signals ($\mathrm{PGV_{ratio}}$), and (iii) the peak velocity of the original signal (PRV). First, a principal component (PC) of ER and $\mathrm{PGV_{ratio}}$ is formed:

$$\mathrm{PC} = 0.63\,\mathrm{PGV_{ratio}} + 0.777\,\mathrm{ER}\,. \tag{8}$$

Then the pulse indicator is

$$\mathrm{PI} = 9.384(0.76 - \mathrm{PC} - 0.616\,\mathrm{PRV})(\mathrm{PC} + 6.914 \times 10^{-4}\,\mathrm{PRV} - 1.072) - 6.179\,. \tag{9}$$

This formulation creates a curved decision boundary in the feature space, replacing Baker's (2007) linear-regression boundary and avoiding the need for an imposed peak velocity threshold. A ground motion signal is labelled as pulse-like when $\mathrm{PI} > 0$ and non-pulse-like when $\mathrm{PI} < 0$. The principal component formulation ensures that PC captures the dominant variance shared between the energy and peak velocity ratios, making the classifier more robust and reducing dimensionality. To focus on directivity pulses, which typically arrive early in the time history, we apply an additional timing criterion based on the cumulative square velocity (CSV), defined by Shahi and Baker (2014) as:

$$\mathrm{CSV}(t) = \int_0^t V^2(u)du\,. \tag{10}$$

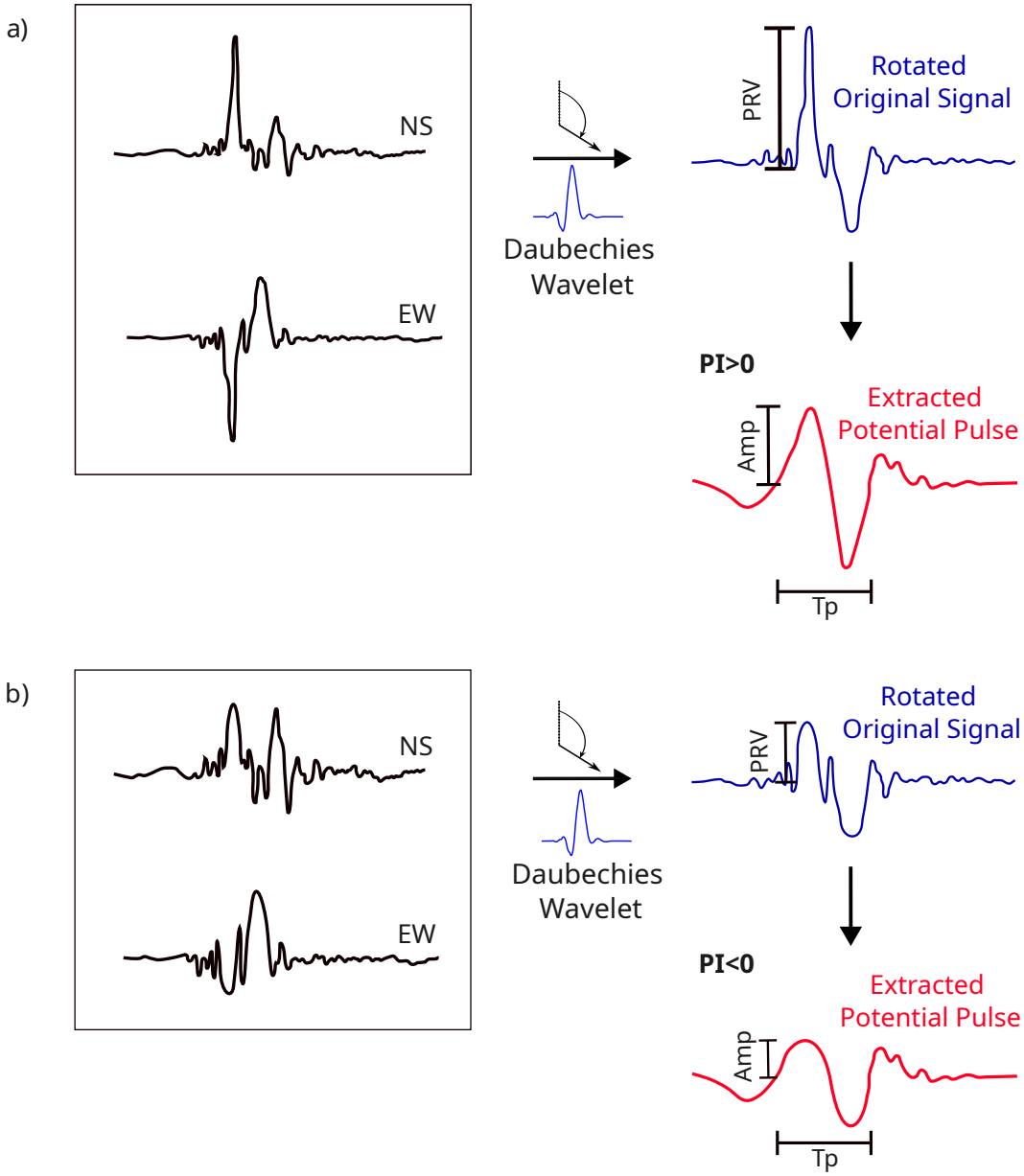


Figure 4: Diagram describing the workflow that the Shahi and Baker (2014) method follows to identify and extract long-period velocity pulses and their corresponding properties: pulse amplitude, period (Tp) and orientation, as well as the peak rotated velocity, PRV. a) Shows a positively identified pulse-like signal, and b) shows a non-pulse-like signal.

Where $V(u)$ is the velocity of the signal at time u. Through this, we search for the time at which CSV(t) is at x% of the total CSV of the signal. This is represented as $t_{x\%,\text{orig}}$ and $t_{x\%,\text{pulse}}$ for the original signal and the extracted pulse, respectively. A pulse is rejected if it occurs too late, specifically when $t_{17\%,\text{orig}} \leq t_{5\%,\text{pulse}}$. Only pulses that pass both the pulse indicator criterion and the timing requirement are considered directivity pulses.

4 Increasing Complexity in Dynamic Rupture Models of the M_w 7.8 Kahramanmaraş Earthquake

In this section, we detail five new dynamic rupture models that we develop and analyse in this study. These follow the same setup as the reference model, along with the changes and increases in complexity that are detailed below. Particularly for the prescribed $\mathcal{R}_0$ (see Figure 3), we prescribe the same values for Model 2 as in the reference model, except along the NPF, where $\mathcal{R}_0$ is increased to initiate at supershear rupture speeds (Section 4.1). Model 4 has identical $\mathcal{R}_0$ and thus $\mathcal{R}$-distribution to the reference model since $\mathcal{R}$ is independent of D_c (Eq. 5). For Models 3, 5 and 6, adopting the same $\mathcal{R}_0$ distribution as used in the reference model prevents dynamic rupture from propagating across the EAF, failing to pass the NPF-EAF junction. We find in trial-and-error simulations (not shown) that achieving comparable rupture dynamics in these models requires a change in the prescribed $\mathcal{R}_0$. Figure S2b shows the rupture speed fault output for one of these trial-and-error simulations for Model 6, in which $\mathcal{R}_0$ is prescribed too large along the eastern portion of the EAF, resulting in supershear rupture speeds in this section. For Models 3 and 5, we additionally prescribe a change in SH_{max} west of the NPF-EAF junction (Supplementary Figure S2a). Varying only $\mathcal{R}_0$ is not sufficient to sustain dynamic rupture across the junction. Compared with the reference model, multi-scale fault roughness (Model 3) and spatial heterogeneity in μ_d (Model 5) add additional shear resistance (Dunham et al., 2011; Fang & Dunham, 2013; Tinti et al., 2021; Taufiqurrahman et al., 2022).

4.1 Model 2: Supershear Initiation

Supershear rupture propagation has been linked to enhanced high-frequency radiation (e.g., Spudich & Frazer, 1984; Bizzarri & Spudich, 2008) and strong directivity pulses (Ertuncay & Costa, 2024), rendering it an interesting candidate mechanism for explaining the observed variability in long-period velocity pulses. We impose a supershear rupture speed initiation along the NPF, using the alternative model presented in Gabriel et al. (2023). This analysis is also motivated by related studies (e.g., Rosakis et al., 2025; Abdelmeguid et al., 2023; Ren et al., 2024) that analyse near-field ground motion records and geodetic data to constrain rupture speed along the NPF and infer local supershear rupture speed.

To achieve supershear rupture speed initiation on the splay NPF, as opposed to subshear initiation in the reference model, we increase the maximum relative stress ratio ($\mathcal{R}_0$) from $\mathcal{R}_0$=0.62 to 0.8 in Model 2. The modified $\mathcal{R}_0$ distribution is shown in Figure 3a.ii and b.i. The rupture nucleates at the prescribed crack-like subshear rupture speed defined within the nucleation patch, as detailed in Section 3.7, and spontaneously reaches supershear as it propagates along the highly pre-stressed splay fault.

4.2 Model 3: Multi-Scale Fault Roughness

In Model 3, we introduce multi-scale fractal fault roughness. The roughness parameterisation follows previous studies (e.g., Candela et al., 2019), and is not intended to represent a specific characterisation for the EAF. Although the effects of fault roughness on high-frequency radiation are well documented in previous simulations (Shi & Day, 2013; Withers, Olsen, Day, & Shi, 2019; Taufiqurrahman et al., 2022), its influence on long-period, near-fault velocity pulses remains largely unexplored. Fault roughness encompasses the natural

variety of geometrical deviations from planarity at different scales along the fault surface. To represent natural fault roughness (W. Power et al., 1987; Renard et al., 2006), we change the originally planar fault surfaces of the NPF and EAF to band-limited, self-similar fractal surfaces (Candela et al., 2009, 2012), while preserving sufficient mesh resolution (see Section 3.4).

Fault roughness can be represented through a fractal fault surface topography (W. Power et al., 1987), described by two parameters. First, the Hurst exponent, which may range between $0 \leq H < 1$, as $H = 1$. This means roughness is self-similar such that it remains statistically invariant at different scales. Second, the amplitude-to-wavelength ratio, α, describes the amplitude of fault roughness and how it varies with wavelength:

$$\alpha = h_{\text{rms}}/L\,, \tag{11}$$

where L is the total along-strike length of the fault and h_{rms} represents the root mean square (rms) roughness of a 2D profile of the fault surface (Dunham et al., 2011; Shi & Day, 2013; Fang & Dunham, 2013). Here, the amplitude-to-wavelength ratio is set to $\alpha = 10^{-2.3}$, consistent with observed roughness of natural faults (W. L. Power & Tullis, 1991). We impose fractal roughness that is band-limited between λ_{min} and λ_{max}. λ_{min} =300 m, corresponding to the smallest on-fault element size, and λ_{max} =10 km (Figure 2c). Compared to the fault system size, the imposed fault roughness remains relatively small-scale, preserving the large-scale reference fault geometries. Figure 2c also illustrates variations of up to $-12°$ in dip angle about the reference value of 90° due to the added roughness.

To sustain rupture across the entire EAF, we slightly adjust the prescribed $\mathcal{R}_0$ and maximum horizontal stress orientation ($SH\text{max}$), based on trial-and-error dynamic rupture simulations (not shown). We increase $\mathcal{R}_0$ from 0.62 to 0.65 along the NPF, from 0.55 to 0.57 along most of the EAF, and from 0.3 to 0.35 on the westernmost EAF segment (Figure 3b.ii). We slightly rotate SH_{max} locally (Supplementary Figure S2a) from $-10°$ to $-8°$ at point iii and from 15° to 17° at point iv to overcome the additional shear resistance due to the 3D "roughness drag" (Fang & Dunham, 2013; Taufiqurrahman et al., 2022). These changes fall within observational uncertainties of the regional stress field (Heidbach et al., 2010).

4.3 Model 4: Heterogeneous D_c

Previous work shows that the acceleration or deceleration phases of a dynamic rupture generate high-frequency content (Madariaga, 1977; Vallée et al., 2008; Li et al., 2022). We introduce a variable critical slip-weakening distance (D_c) value across the fault in an attempt to generate this "stop-and-go" effect of the rupture propagation. We apply this to explore the effects on high-frequency content by generating variable fracture energy by prescribing patches of variable D_c, as well as to explore whether these changes affect directivity pulse characteristics.

In order to simulate variable D_c, following the approach by Ide and Aochi (2005), we define a fractal distribution of frictional asperities with size-dependent D_c, in turn, defining heterogeneous fracture energy along the EAF. This approach defines families of different patch sizes corresponding to different D_c values that are stacked on each other in a hierarchical manner.

There are a total of 8 families with a fractal dimension of $D = 1.52$ along the EAF and 7 families with $D = 1.12$ across the NPF. The smallest patches, which are the most abundant, correspond to D_c values of 0.2 m and a patch radius of 300 m, allowing for patches of faster weakening and more easily propagating rupture fronts. On the other hand, the largest patches have a patch radius of 38,400 m on the EAF and 19,200 m on the NPS. These correspond to D_c values of 0.9 m and are the least abundant, with only two of the

largest patches defined on each fault (Figure 2d). These allow for higher fracture energy patches that slow down the rupture front, therefore creating a variable stop-and-go effect on the rupture propagation. Along with a background value of 1 m, the relationship between the number of patches ranging between 0.2 and 0.9 m is varied to produce an overall average D_c value of 0.5 m, as defined in the reference model for the faulting system of the first event.

4.4 Model 5: Heterogeneous μ_d

Fault stresses and strengths are difficult to constrain from observations and therefore tend to be described as constant or varying linearly with depth (e.g., Galvez et al., 2014; Gabriel et al., 2023; Marchandon et al., 2025). Since frictional fault strength is known to impact rupture propagation (Harris et al., 2018; Tinti et al., 2021), we incorporate a heterogeneous distribution of the dynamic coefficient of friction, μ_d, an often overlooked approach, to explore its effects on rupture propagation speed and, therefore, frequency radiation. We implement this through a similar approach as in Model 4, using the Ide and Aochi (2005) approach.

We define fractally distributed frictional asperities with size-dependent values for μ_d, with μ_d values ranging from 0.1 in the smallest and most abundant patches to 0.3 in the largest and least abundant patches. If μ_d is chosen too large, it becomes close to the static friction value and inhibits dynamic rupture. The background value is set to 0.2 to average to an overall distribution of $\mu_d = 0.2$ as in the reference model (Figure 2e). This setup has a total of 7 families with a fractal dimension $D = 1.6$ along the EAF and $D = 1.1$ on the NPF. The smallest patches are of radius $r_0 = 300$ m and the largest patches of radius $r = 19,200$ m. Similar to Model 3, the prescribed $\mathcal{R}_0$ value for the NPF is changed from 0.62 to 0.65 (Figure 3b.iv) and the SH_{max} value for points iii and iv in Figure S2a are changed to $-6°$ and $19°$, respectively.

4.5 Model 6: Large-Scale Fault Waviness

Given that directivity pulses are of low frequencies, we next include a geometric complexity that is aimed at low-frequency wavefield generation. For example, Withers, Olsen, Day, and Shi (2019) show that the ground motion signature of rupture directivity is predominantly at low frequencies for large magnitude earthquakes. We also investigate the effect of large-scale fault waviness, representing long-wavelength variations in fault geometry. Although implemented using the same approach as for the fault roughness (Model 3), this model targets a much larger spatial scale. Specifically, we prescribe a band-limited self-similar fractal deviation of planarity with wavelengths ranging from $\lambda_{min} = 20$ km to $\lambda_{max} = 60$ km, and an amplitude-to-wavelength ratio of $\alpha = 10^{-2.5}$. The wavelengths are chosen specifically to align with periods between 5 – 16 s. Assuming characteristic wave speeds of 2–4 km/s, pulse periods of 5—16 s correspond to spatial scales ranging from 10 to 64 km, consistent with the prescribed waviness. This model allows us to isolate the influence of large-scale fault geometry on the generation and variability of long-period velocity pulses.

The top figure in Figure 2f shows the map view of the fault geometry, highlighting the added waviness, particularly to the west of the NPF–EAF junction, without altering the overall fault geometry. As in c), the bottom figure depicts dip angle variation due to the applied large-scale waviness. As described in Figure 3b.v, the $\mathcal{R}_0$ value along the NPF is set to 0.65, the majority of the EAF is increased to a value of 0.56, while the westernmost segment is increased to 0.35.

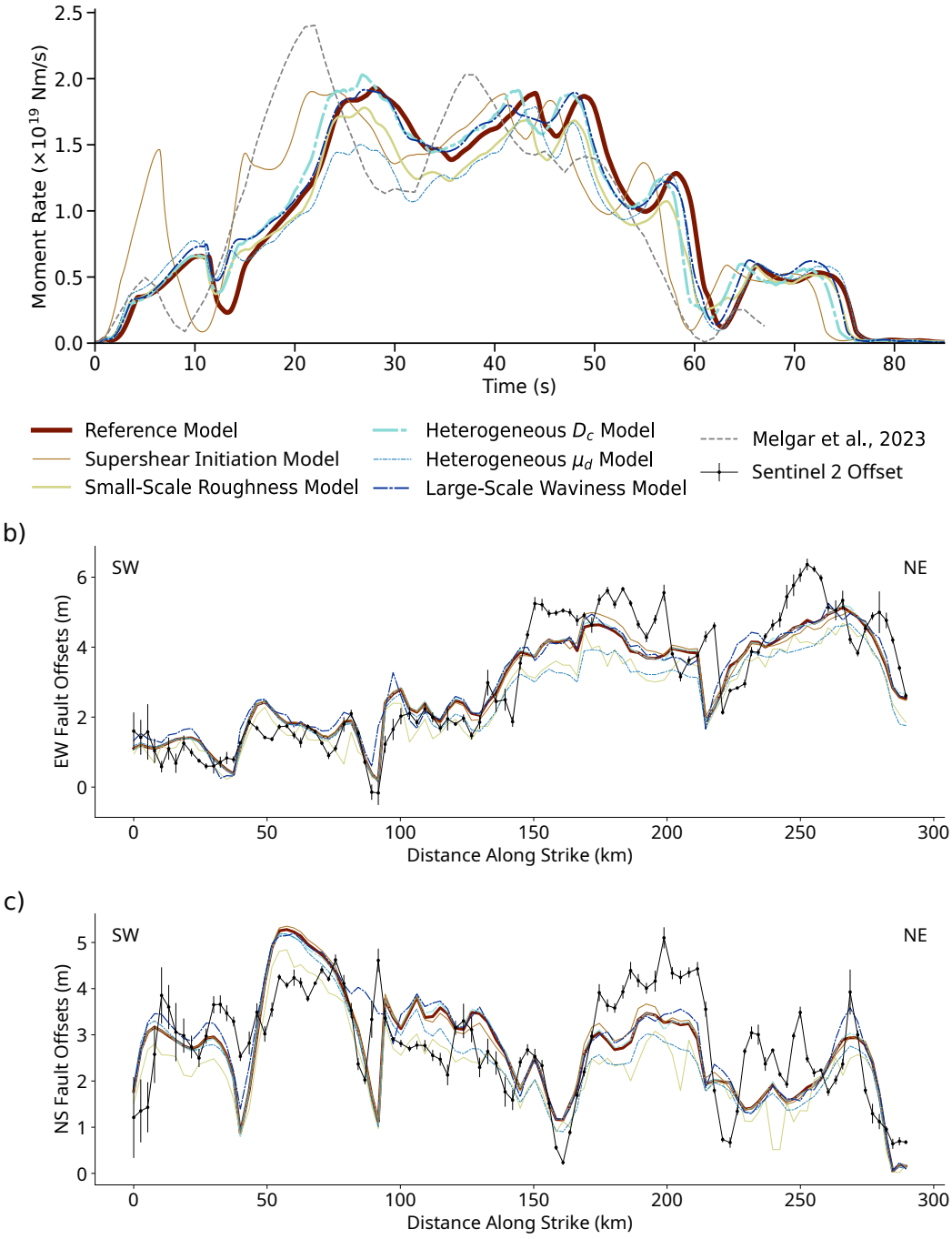


Figure 5: a) Moment rate release of all six dynamic rupture models along with the moment rate release from the kinematic model of Melgar et al. (2023). b) and c) show the NS and EW fault offsets, respectively, for the six models compared to Sentinel-2 data (see Open Research Section.

5 Results

5.1 Effects on Rupture Dynamics

All five new dynamic rupture scenarios of the M_w 7.8 Kahramanmaraş earthquake show overall similar characteristics in rupture dynamics to the reference model, and in turn, to the observations (Gabriel et al., 2023; Melgar et al., 2023). Both the reference model following Gabriel et al. (2023) and the data-informed dynamic rupture simulations from Jia et al. (2023) independently reproduce the main features of the M_w 7.8 Kahramanmaraş earthquake. Both of these studies show that although the slip distribution produced by these synthetic models is rather smooth compared to the data-driven slip models, they compare rather well when considering the timing of the rupture. They produce surface displacements and slip histories that align well with high-resolution geodetic data, kinematic rupture representations of the seismic event and observed ground motions. Figures S6 – S12 show three-component velocity waveforms for all six models at the 18 near-fault stations with synthetics, and the observations at all 21 near-fault stations used in the pulse analysis. Synthetics and observational data are filtered identically with a 1 Hz low-pass filter, a frequency resolved throughout the computational domain, including its coarser regions (Section 5.3). All six models show first-order agreement with the observations. Except for the supershear initiation model, they reproduce the timing of the main impulsive arrival to within ∼2 s, and its amplitude to within a factor of ∼ 2. The differences between models are small, and only the supershear initiation model is distinguishable. On all three components, its arrivals precede those of the other five models and of the observations by ∼ 3 s.

Model	M_0	M_w
Reference	7.778e+20	7.857
Supershear Initiation	7.962e+20	7.864
Small-Scale Roughness	7.053e+20	7.829
Heterogeneous D_c	7.847e+20	7.860
Heterogeneous μ_d	6.964e+20	7.825
Large-Scale Waviness	7.925e+20	7.863

Table 2: Seismic moment and moment magnitude for all models.

Figures 5 to 8 and Table 2, as well as Movies S1 and S2 in the supplementary material, summarise each model's rupture dynamics, discussed in detail in the following. The total seismic moment magnitude and the moment rate release of all six models are comparable, despite the varying model complexities (Table 2, Figure 5). We see almost identical propagation of slip rate when comparing all models in Movie S1. For all models, the moment rate release between 0 and 12 s represents the rupture along the NPF, and a slight decrease in moment rate release at 12 s aligns with the rupture crossing the NPF-EAF junction and continuing at subshear rupture speed. This is followed by an increase in moment rate release at around 20 s, when the rupture also begins to propagate along the western part of the EAF. The moment rate release begins to decrease at around 55 s, when the rupture reaches the end of the eastern part of the EAF, and a final peak can be seen between 60 – 77 s, where the rupture propagates along the final segment of the western part of the EAF. The supershear initiation model (Model 2) stands out with a higher moment rate release at the start of the rupture between 0 and 10 s, representing the supershear rupture along the NPF. This allows it to cross the junction earlier than in the other models, with more energy, while following the same moment rate release pattern after the junction.

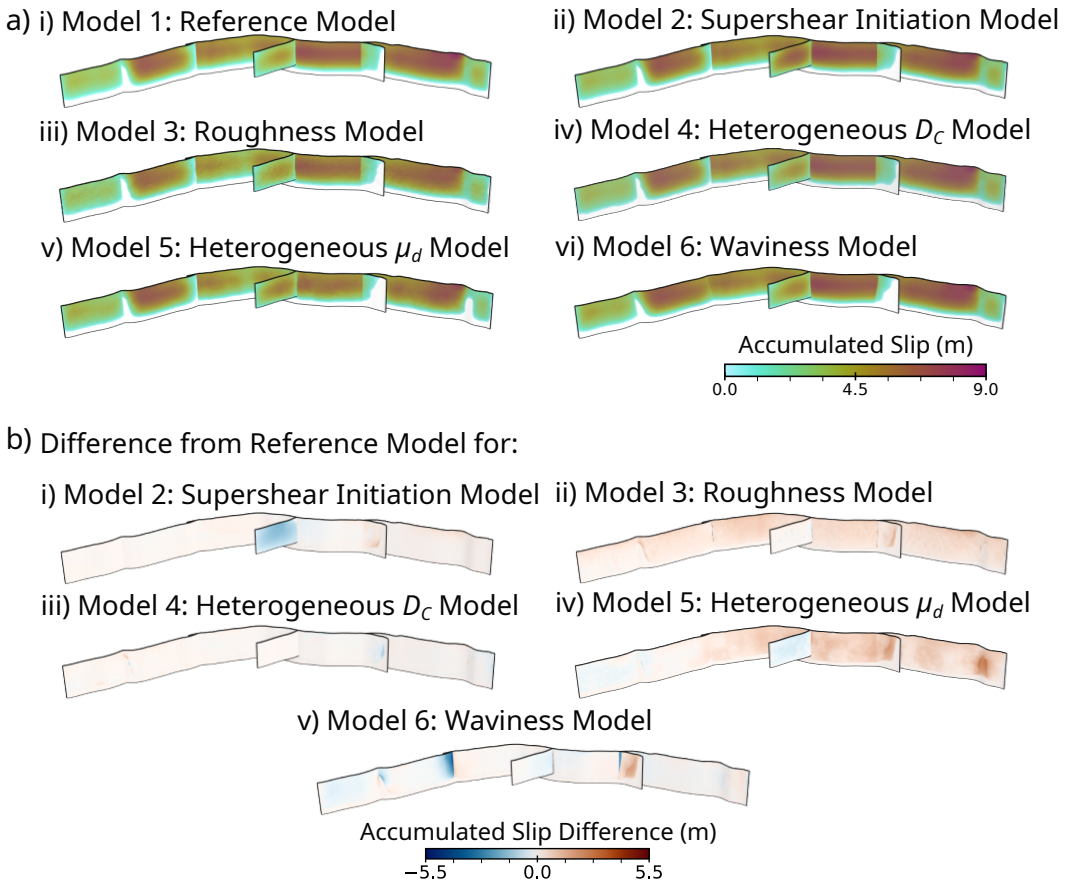


Figure 6: a) Accumulated slip for all six models. b) The difference in the accumulated slip between the reference model and the models with added complexities (Difference = Reference Model - Complexity Model).

The heterogeneous D_c model shows slightly higher energy release ($\sim 0.2 \times 10^{19}$ Nm/s higher) as it traverses the first segment of the eastern part of the EAF compared to the reference model. In contrast, the multi-scale roughness and the heterogeneous μ_d models have a slightly lower seismic moment release ($\sim 0.2-0.5 \times 10^{19}$ Nm/s lower) for the majority of the propagation along the eastern part of the EAF and the start of the western part, and have a slightly lower seismic moment compared to the other dynamic rupture models (Table 2).

Gabriel et al. (2023) highlight the alignment between fault offsets derived from Sentinel-2 data (see Open Research Section) and those from the dynamic rupture models. Similarly, Figures 5b and c highlight how well the synthetic NS and EW offsets of the 5 new models compare to the reference model and the observational data, reproducing the overall offset distribution and along-strike variability. As shown in Figure 6, all models exhibit similar accumulated fault slip (ASl) distributions. The roughness and μ_d models exhibit up to $\sim$ 5 m less total slip, particularly along the western part of the EAF, compared to the reference model (Figure 6b.ii and iv). The supershear initiation model (Model 2) exhibits higher total slip along the NPF of up to $\sim$ 5 m (Figure 6b.i). We also observe an increase of $\sim$ 1.5 m for the μ_d model (Model 5) along the NPF (Figure 6b.iv).

Figure 7 compares the peak slip rate (PSR) of all models. Geometric and frictional complexities in fault roughness, D_c, and μ_d models lead to a more variable peak slip rate.

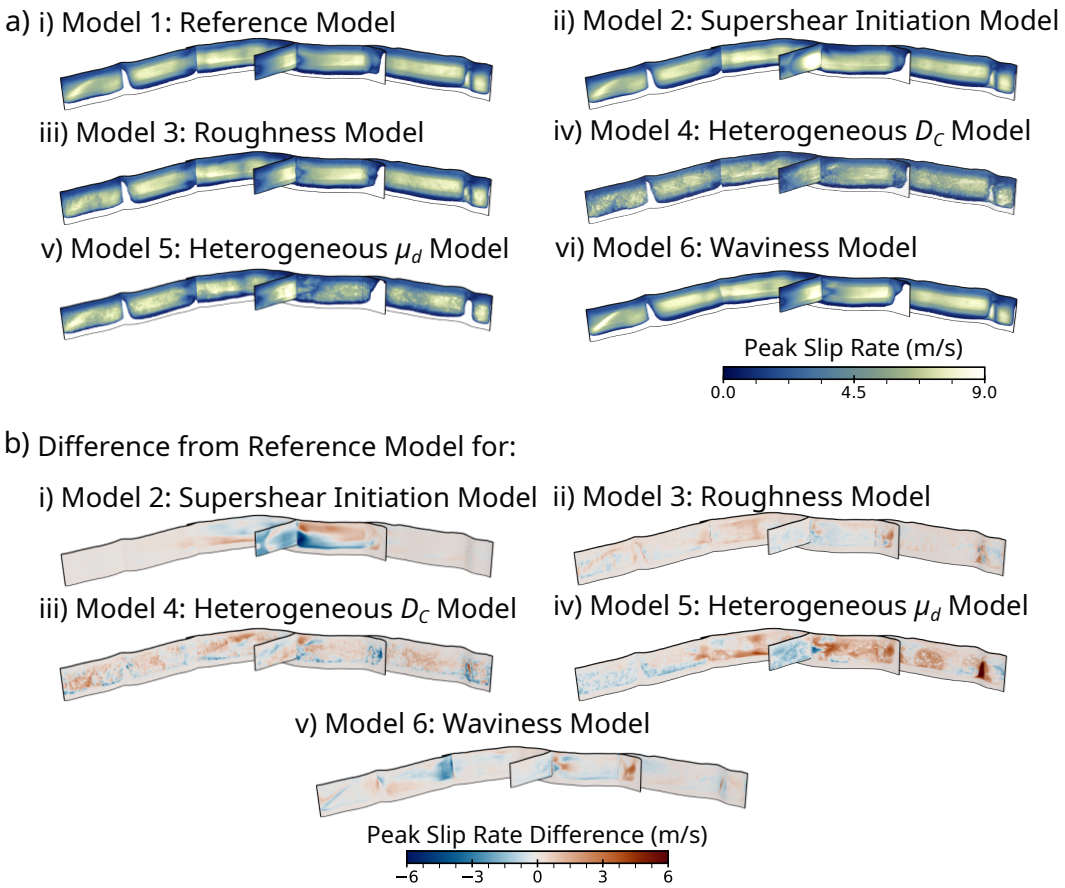


Figure 7: a) Peak slip rate for all six models. b) The difference in peak slip rate between the reference model and the models with added complexities (Difference = Reference Model - Complexity Model). The values range between -7.3 and 9.1 m/s but are saturated between -6 and 6 m/s for better representation of the differences.

PSR increases drastically along the NPF by $\sim 6-7$ m/s for the supershear initiation model (Figure 7b.i), and larger PSR values are also seen in the waviness model compared to the reference model (Figure 7b.v). Interestingly, the impacts of the asperities in the roughness, D_c, and μ_d models are evident in Figure 7. The PSR increases and decreases along the included asperities, particularly in the μ_d model, where the PSR variability pattern appears to follow the pattern of the defined variable μ_d (Figure 2f).

The rupture speed distributions shown in Figure 8 and Movie S2 also demonstrate similarities in rupture dynamics across models. A smooth and relatively constant subshear rupture speed is observed in the reference model (Figure 8a and Movie S2a), which is resembled in the supershear initiation model (Figure 8b and Movie S2b) except along the NPF. Perturbations in rupture speed due to geometry and friction heterogeneities are observed in the roughness and μ_d models (Models 3 and 5), where there are local episodic changes in rupture speed across the entire fault system. Similar perturbations that generate episodic supershear rupture speeds are observed in the D_c model. Lastly, the waviness model shows constant rupture speed similar to that in the reference model, with some minimal variations due to how the different segments are triggered, particularly to the west of the NPF-EAF junction.

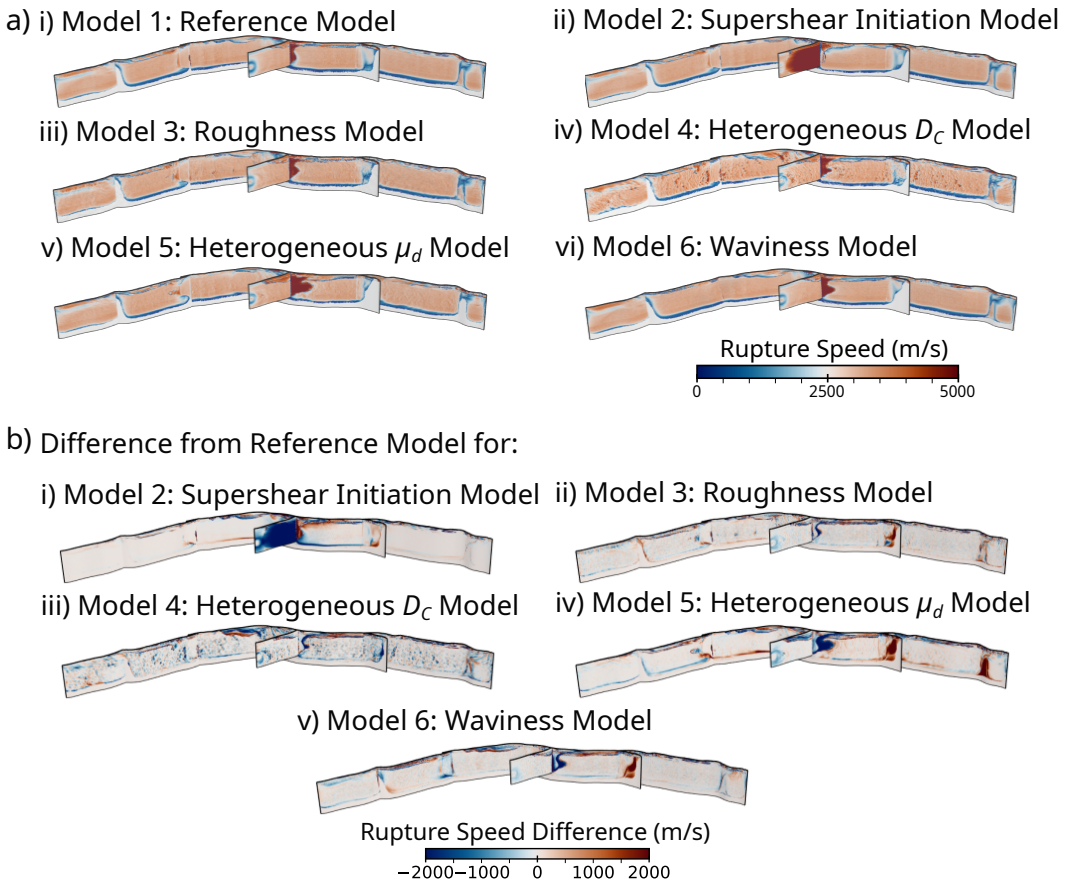


Figure 8: a) The rupture speed along the fault for the six models explored, where the dark red areas highlight supershear rupture speed. b) The difference in the rupture speed between the reference model and the models with added complexities (Difference = Reference Model - Complexity Model).

From Figure 7, we can also observe a correlation between PSR and rupture speed (e.g., Rice et al., 2005; Gabriel et al., 2013). Although the relation viewed here is unclear, the impacted PSR in Model 4 appears on the particular fault segments where transient supershear rupture speeds are observed. This implies that the presence of local transient supershear rupture speeds impacts PSR. We see this in Figure 7a.iv and b.iii in the areas of the previously mentioned rupture speed perturbations along the EAF for the D_c model, oriented at a strike of ~ 26 ° and ~ 80 °.

5.2 Long-Period Velocity Pulse Analysis

The pulse analysis described in Section 3.9 is used to investigate the low-frequency regime of all six dynamic rupture models. Figure 9 illustrates the extracted long-period velocity pulses at all near-fault stations. Because each model generates seismograms that differ from those of the reference model, the number of stations classified as pulse-bearing varies. For example, the roughness model and the D_c model do not produce pulse-like motion at station 3131, whereas the waviness model produces pulse-like motion at an extra southern station, station 3123. Furthermore, the supplementary Figures S1 and S5 show the comparison of pulse maps from the Jia et al. (2023) model and our reference model, where circle size corresponds to PRV and pulse amplitude, respectively. All the original

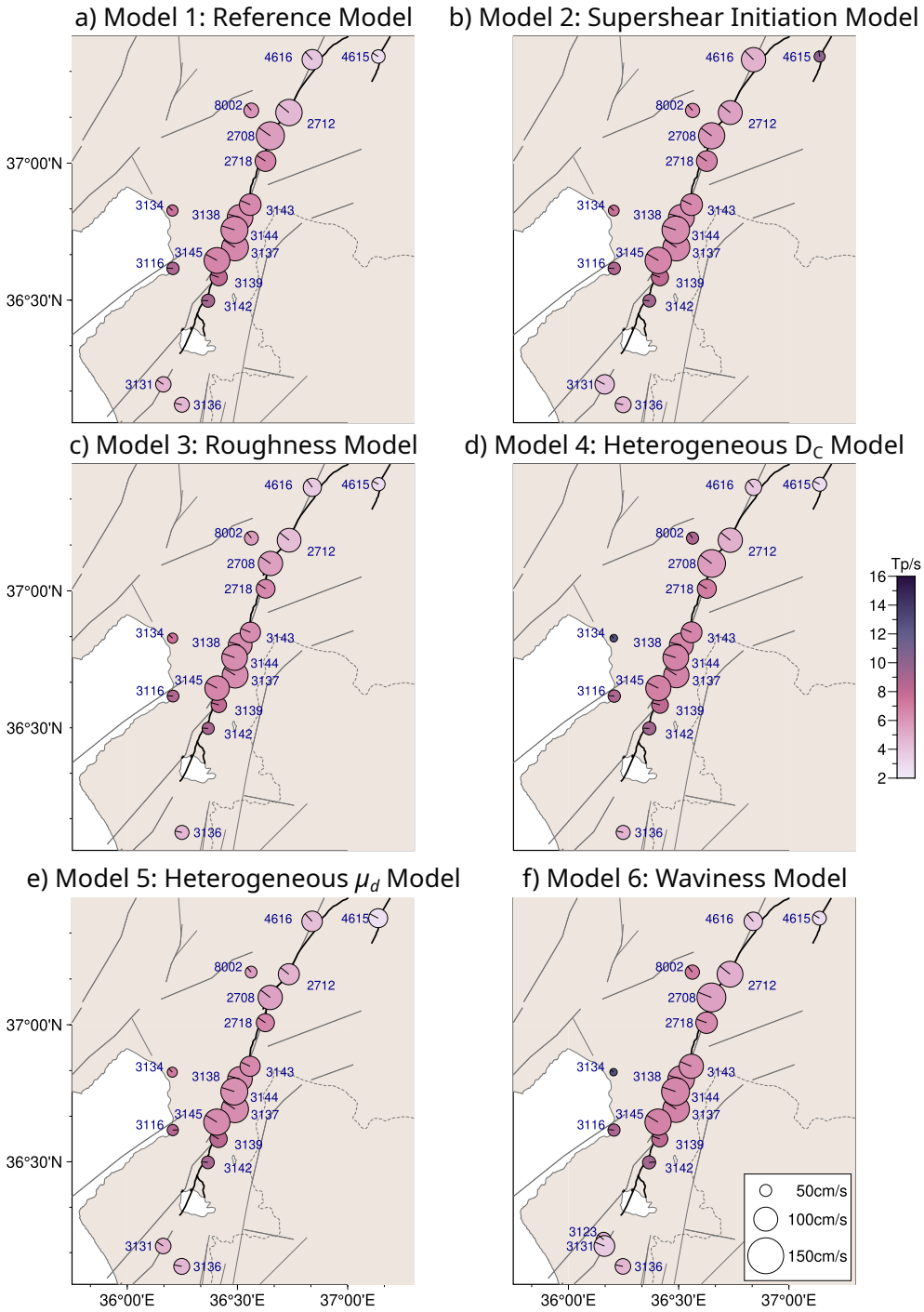


Figure 9: Maps showing velocity pulse properties extracted at various stations for each model. The circle size corresponds to the pulse amplitude, the colour corresponds to the pulse period (T_p), and the lines within the circles represent the pulse orientation. For each model explored, the seismograms at each station differ from those in the reference model, leading to model-dependent variations in the classification of velocity pulses. As a result, each model has a different total number of stations that are classified as containing velocity pulses.

rotated waveforms and extracted pulse waveforms can be seen for all six models and the observational data at all stations in the supplementary Figures S13–S31. Similarly, Tables S3 – S9 show the specific values of the extracted pulse characteristics for the seven datasets.

The reference scenario captures the broad pulse amplitude variability observed in the data (Figures 1b and S5). This variability is reproduced consistently across all models (Figures 9, 10, and S32a). The amplitude distributions for all models across the different stations shown in Figure 10a show that the amplitudes vary within the same range of 30—120 cm/s, and all models follow a spatial trend similar to that of the reference model. Here, the large-scale waviness model generates the largest divergences from the reference pattern. Pulse durations, T_p, show modest sensitivity to the added heterogeneities. The reference model produces T_p values between roughly 2–9 s. Supershear initiation, heterogeneous D_c, and large-scale waviness broaden this range to approximately 2-–13 s at a few stations (Figure 10b). The D_c model leads to the strongest deviations in pulse duration, consistent with its locally episodic supershear behaviour identified in the rupture speed (Figure 8). These changes remain small compared to the variability inferred from observations (Figure S32b).

Pulse orientation remains largely unaffected by the imposed dynamic rupture complexities. Most stations preserve fault normal orientations, as in the reference model. Only three stations in three different models (4615 in Model 2, 3116 in Model 5 and 3142 in Model 6) show orientation changes (Figure 10c). The supershear initiation model modifies both T_p and pulse orientation at station 4615, which rotates toward a more fault-parallel orientation and lengthens in period. Two additional changes of pulse orientation involve 180◦ flips at station 3116 and station 3142 in the heterogeneous μ_d and waviness models, respectively. Aside from these isolated examples, the modelled pulse orientation variability is very minimal in all models, in contrast to the broader range observed in observational data (Figure S32c, Yen et al. (2025)).

Supplementary Figure S33 shows the comparison between the PRV and pulse amplitude for the six models and the observational data. This figure highlights that the extracted pulse amplitude follows the same trend as the PRV, which is the parameter that is commonly presented (e.g., Yen et al., 2025; Yucel et al., 2026; Akinci et al., 2025). Overall, our analysis shows that all dynamic rupture models capture pulse amplitude variability well but generate limited variability in pulse periods and orientations. Supershear rupture and large-scale geometric perturbations exert the strongest influence, although their effects remain localised. The systematic lack of orientation variability suggests that additional physical processes, such as off-fault fracturing or path-dependent modifications, may be required to explain the patterns observed in the recordings.

5.3 Higher-Frequency Analysis

We apply spectral analysis to the synthetic seismograms at all stations for each of the six dynamic rupture models. For each three-component velocity time series, we compute Fourier amplitude spectra and compare the spectral shapes and levels across models and stations (Figure S34). In the near-fault high-resolution region, the simulations numerically resolve frequencies slightly above 2 Hz, whereas in the coarser parts of the mesh, the reliable frequency range extends to about 1.5 Hz.

Inspection of the spectra over the total frequency band shows that all models produce similar spectral shapes at both near- (Figure S34c) and far-fault stations (Figure S34d), with comparable low-frequency plateaus and a similar decay at higher frequencies. Small differences in spectral amplitudes occur from station to station but are not systematic between models. Focusing on the near-fault stations and restricting the analysis to 0–1 Hz (Figures S34a,b), the spectra of the six scenarios nearly overlap at most sites, with only modest deviations that are comparable to the spread between components or neighbouring

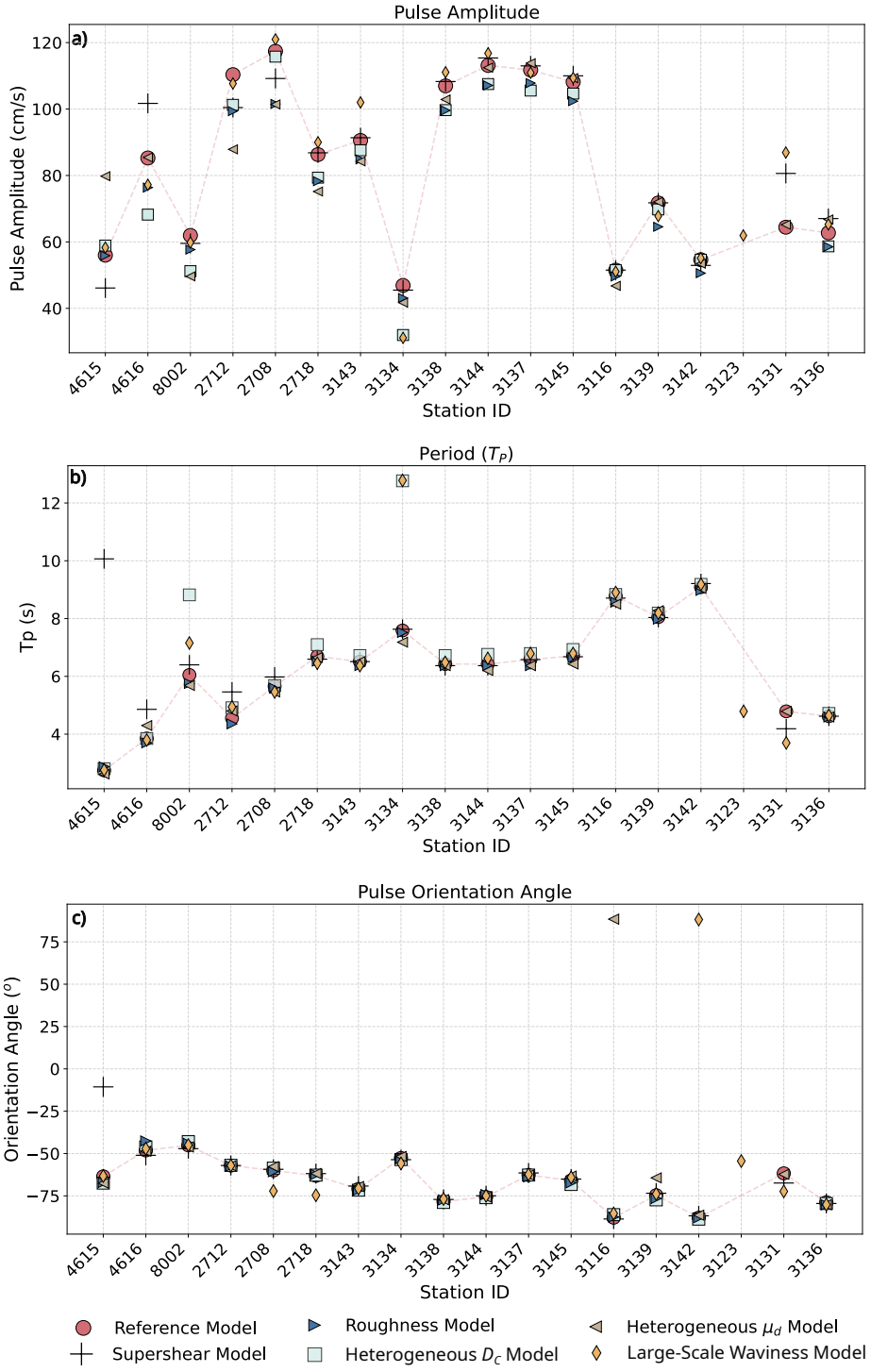


Figure 10: A comparison of a) pulse amplitude, b) pulse period (T_p), and c) pulse orientation for all six models. The pink dotted line represents the reference model variability trend to emphasise differences between models with added variability and the reference model.

stations. Within this band, the heterogeneous models therefore do not exhibit a clear, model-dependent shift in spectral level or corner frequency relative to the reference case.

This analysis contrasts with the imprint of supershear rupture, roughness, and heterogeneous friction on rupture speed, peak slip rate and rupture dynamics (Figures 5, 8 and 7). This may suggest that the main impact of these complexities would be expressed at frequencies approaching or exceeding the upper limit of our resolved range, (e.g., B. Wu et al., 2025). The small-scale features we introduced in the roughness, D_c, and μ_d models following (e.g., Shi & Day, 2013; Graves & Pitarka, 2016; Taufiqurrahman et al., 2022) do not translate into robust differences in spectral amplitudes below about 1 Hz. Additional variability in higher-frequency ground motions is likely to occur at frequencies beyond those analysed here and would require finer spatial resolution and more detailed attenuation structure to be reliably quantified.

6 Discussion

6.1 Validation of Modelled Long-Period Near-Fault Pulse Characteristics

As detailed in Section 5.2, all heterogeneous dynamic rupture models reproduce the same variability in modelled pulse amplitudes that is produced by the reference model. They follow the same fluctuation patterns, which, in turn, when compared to observed data (Figure S32a), align quite well with the variability patterns observed in nature. It is the reference model that appears to perform the most similar to the observed data, whilst the added complexities often cause a deviation from the more optimal variability produced by the reference model. However, all six models appear to overestimate the pulse amplitude values compared to those observed.

On comparing the T_p variability between the models and the observed data in Figure S32b, we see that the synthetics produce values between 3 s and 9 s at most stations, and up to ∼13 s for two models, whereas the observational data show values ranging between 3 s and 15 s, with a very different variability pattern. Although it is understood that the pulse period range is driven by the magnitude of the earthquake (Fayjaloun et al., 2017), substantial within-event variability in T_p has also been reported between stations recording the same earthquake (Yen et al., 2021; Fayjaloun et al., 2017; Cao et al., 2025). Yen et al. (2025) report a broad range of observed pulse periods for the 2023 Kahramanmaraş earthquake doublet. Other factors may also contribute to this variability, including site effects, which can interact with near-field directivity effects (Rodriguez-Marek & Bray, 2006; Yen et al., 2025; Cao et al., 2025) and are not modelled here.

Some models show localised changes in the extracted pulse period. For example, Models 4 and 6 exhibit an approximate 5 s increase in T_p relative to the other models at station 3134 (Figure 10b). The corresponding pulse waveforms (Figure S20) show a more extended and complex pulse-like arrival, suggesting that the increase in T_P reflects an enhancement of longer-period features in the waveform. These changes may be related to modifications in the radiation pattern introduced by the respective heterogeneities, although the sensitivity of the wavelet-based extraction method to the waveform shape should also be considered (Yen et al., 2021).

Figure S32c shows the lack of pulse orientation variability produced by the models compared to what is seen in the observational data, similar to what was observed in Yen et al. (2025) using the dynamic rupture model by (Jia et al., 2023). This limited variability suggests that the heterogeneities we explore may, in general, not be the major factors involved in controlling the pulse orientation. However, a local impact of supershear rupture speeds on pulse properties is seen at station 4615 for the supershear initiation model. Supershear ruptures have been speculated to be responsible for the generation of near-fault pulse-like motion, as such rupture speeds reshape the S-wave radiation pattern. When rupture speed exceeds the S-wave speed of the host rock, shear dislocation on the fault releases some strain

energy as shear Mach wave fronts (Dunham & Bhat, 2008). This may cause most of the near-field seismic energy to arrive in one pulse of motion, expected at the S-wave arrival time (Somerville et al., 1997; Ertuncay & Costa, 2024).

In our results, the supershear initiation model is the only model that produces a distinguishable difference in the three-component waveforms, with the main impulsive arrivals occurring ~ 3 s earlier than in the other models and the observations. This timing difference follows from the imposed supershear rupture propagation along the NPF and is consistent with its earlier crossing of the NPF-EAF junction and enhanced amplitudes in the moment rate release during the initial stage of rupture (Figure 5). Despite this difference in the time domain, this is a phase effect and therefore leaves no signature in the Fourier amplitude spectra, where all six models nearly overlap below 1 Hz (Section 5.3).

At station 4615, the supershear rupture speed locally impacts the generation of pulse-like motion, resulting in a more variable pulse in both period and orientation in this region of the fault. On comparing the variations in pulse amplitude and orientation with the observed data in Figure S32, we can see that the values for station 4615 for the supershear initiation model are closer to those observed. All other models differ from the observed pulse amplitude at this station by ~ 50 cm/s, while Model 2 only differs by ~ 10 cm/s. Similarly, for the pulse orientation, all other models differ by $\sim 50°$, while Model 2 is closer in orientation, differing by $\sim 10°$. This could support the hypothesis of the likelihood of supershear initiation and propagation along the nucleating NPF (e.g., Abdelmeguid et al., 2023; Delouis et al., 2024; Ren et al., 2024; Rosakis et al., 2025).

Although the overall pulse orientations remain relatively consistent between the models, two localised polarity reversals are observed at station 3116 in Model 5 and at station 3142 in Model 6. Examination of the candidate pulses (Tables S10 and S11) and extracted pulse waveforms (Figures S25 and S27) indicates that these changes represent a reversal in the polarity of the dominant pulse. In both cases, the dominant pulse has a similar characteristic period and coefficient magnitudes to that of the reference model, but with opposite polarity (Tables S10, S11 and Supplementary Excel File S1). This suggests that the heterogeneities we investigate in this study may play a role in localised changes in polarity. The observational data similarly includes both positive and negative pulse orientations (Table S9, Figure S32c). While five stations exhibit positive orientations, three of these, stations 3138, 3144 and 3145, show orientations that are broadly similar in magnitude but opposite in sign to those of the reference model.

Upon further investigating the impact of the D_c heterogeneities, we can rule out that the cause of the effects on the pulse properties is due to a changing fracture energy via the changes in D_c. If this were the cause, it would imply that similar results should be obtained from the heterogeneous μ_d model, which only affects the pulse orientation at one station. The impact of D_c heterogeneities is most likely linked to the locally episodic supershear rupture speed perturbations that we observe along the fault system in Model 4 (Figure 8). Such supershear bursts are not observed in any of the other five models presented in this study and are most likely responsible for the T_p and amplitude variability generated in Model 4.

To investigate whether stronger D_c heterogeneities could produce larger changes in rupture propagation and pulse characteristics, we perform additional simulations of models with increased average D_c amplitudes and increased spatial variability (see Supplementary Section 1 and Table S12). These simulations imply that stronger D_c heterogeneity can produce substantially more heterogeneous rupture propagation (Supplementary Figure S35). However, the dynamic models are highly sensitive to these changes, particularly around the fault junction. Increasing the mean D_c sufficiently can prevent rupture from propagating past the junction onto the western portion of the EAF, while other realisations promote more extensive supershear rupture. We therefore focus on those simulations that retain the principal rupture characteristics of the reference scenario (Models R1, R2, R3 and R4).

Among these simulations, the resulting long-period pulses remain remarkably similar to those of the original D_c model (Model 4), except for a few outliers (Supplementary Figure S36). This indicates that increasing the heterogeneity of D_c alone does not necessarily result in a corresponding increase in pulse variability. Interestingly, models R2 and R3 appear to add some variability in the pulse orientation that does not only involve changes in polarity. These changes are apparent at stations 3144, 3145 and 3116 for Model R2 and at stations 3138 and 3144 for Model R3. One possible cause of these local changes in orientation is the more prominent localised bursts of supershear rupture speeds caused by the different distributions of heterogeneous D_c, however, further investigation on the impacts of variable rupture speeds on velocity pulses is required. These two models also correspond to significantly lower pulse amplitudes at these stations compared to the other models, (30 cm/s – 50 cm/s vs ∼110 cm/s). This suggests that these changes in orientation could also be linked to the limitations of the pulse extraction method (see Section 6.2).

As the large-scale waviness model has been designed to introduce a physical on-fault heterogeneity that is comparable to the target long-period characteristics of the pulses, it was expected to influence pulse behaviour. The extent of this model's impact on the pulse period and orientation implies that the waviness wavelengths we use are too large for this target. In the top view of the fault for this model in Figure 2f, the effects of the waviness are minimally observed on a small portion of the south-western end of the EAF. Although the model's influence on the pulse properties could correlate with areas of pronounced waviness on the fault, there is not enough evidence for such a definitive interpretation. This could be further explored through applying waviness wavelengths between 10 and 40 km.

Although the influence of heterogeneities, such as fault roughness and heterogeneous μ_d, on long-period velocity pulses has not been extensively explored, the limited impact observed here is not unexpected. We include these features primarily for their known effects on rupture dynamics and frequency radiation, rather than for an anticipated influence on long-period pulse characteristics (Withers, Olsen, Day, & Shi, 2019; Harris et al., 2018). The roughness and μ_d models do, however, introduce localised changes in rupture behaviour relative to the reference model. In particular, these models show localised variations in peak slip rate and rupture speed (Figures 7 and 8). Models 3 and 5 exhibit a reduced moment rate release (Figure 5) and lower seismic moment (Table 2), suggesting that these heterogeneities introduce additional resistance to rupture propagation (e.g., Fang & Dunham, 2013; Ripperger et al., 2007). Although such heterogeneities modify the local rupture dynamics, their effects remain insufficient to produce substantial changes in the characteristics of the generated long-period pulses. Despite these effects on dynamic rupture propagation, within the resolved frequency range of at least $\sim$ 1 Hz, no individual model exhibits distinctly higher spectral amplitudes, with the overall frequency content remaining broadly similar across models. This is somewhat unexpected, given the established role of fault roughness and heterogeneous μ_d, and reflects limitations imposed by numerical resolution or the specific parameterisation adopted here.

Overall, these results indicate that the heterogeneities explored in this study can modify the local rupture dynamics without producing corresponding changes in the large-scale characteristics of the generated long-period pulses. The consistency of the fault-normal pulses across the models suggests that their large-scale generation is strongly influenced by the overall rupture propagation and faulting geometry, particularly the coherent S-wave radiation associated with the predominantly subshear rupture (Dunham & Bhat, 2008). The inability of these models to produce the stronger variability observed in the strong-motion data suggests that additional complexities may contribute to the fine-scale variability observed in nature.

6.2 Limitations and Future Work

The limited impact on pulse period from our heterogeneous dynamic rupture models could be related to a few additional aspects not discussed above. The first potential problem could be omitting site effects, even though the earthquake is located in a basin area. There have been a number of studies on the site effects due to the basin sediment in the area that show that these can have an amplification effect on the amplitudes and periods of such long-period pulses (e.g., Rodriguez-Marek & Bray, 2006; Koketsu et al., 2016; Yen et al., 2021; Ertuncay & Costa, 2024). Yen et al. (2025) showed that site effects can interact with near-field directivity effects when the pulse period is close to the site's dominant frequency. These effects may interact mutually or solely affect pulse generation (Cork et al., 2016; Kaneko & Goto, 2022; Cao et al., 2025), potentially leading to significant variability in pulse properties. The basin sediments have not been taken into consideration in this study due to the limited availability of 3D velocity models. In future work, this could be improved through the use of a more detailed 3D velocity model (Li et al., 2025) or through a correction for site effects on the synthetic signals as an extension of the concepts in Rodgers et al. (2020). A further limitation concerns the pulse extraction methodology itself. The Shahi and Baker (2014) method identifies pulse-like features using a wavelet-based approach, therefore, the pulse period is estimated from the pseudoperiod, i.e. the period corresponding to the maximum Fourier amplitude, of the selected wavelet. Consequently, the estimated period is dependent on the mother wavelet and its ability to represent the pulse within the ground motion. If a mother wavelet matches the broad temporal shape of a smooth peak, it may capture a longer timescale than the underlying pulse, leading to an overestimation of the apparent pulse period (Yaghmaei-Sabegh, 2010; Yen et al., 2021).

Another difficulty is properly representing the fault system geometry. It is very challenging to know the precise fault geometry beyond what is obtainable through geodetic and aftershock data, specifically at depth. Since this was not explored in this study, using an even more detailed, complex fault geometry, for example, one that includes more step-overs or larger variations in fault dip, would be interesting (Shahi & Baker, 2011; Lozos et al., 2025). Furthermore, geological observations show that fault zones host multi-scale fracture networks and damage zones, and such distributed damage is known to affect rupture dynamics and near-fault radiation (W. L. Power & Tullis, 1991; Ben-Zion & Sammis, 2003; Zhao et al., 2024; B. Wu et al., 2025; Gabriel et al., 2024; Palgunadi et al., 2024, 2025). Modelling this at the scale of the Kahramanmaraş event is currently computationally out of reach and is a priority for future work.

The choice of friction law may also influence the rupture behaviour and, consequently, the resulting ground motion variability. All simulations in this study use a linear slip-weakening friction law, and we do not assess the sensitivity of our results to alternative friction formulations. Classic formulations of rate-and-state friction (Dieterich, 1979; Ruina, 1983) exhibit an effective slip-weakening response during dynamic rupture, such that an equivalent slip-weakening distance can be formulated from the rate-and-state parameters and initial state (Cocco & Bizzarri, 2002; Bizzarri & Cocco, 2003). Furthermore, model comparisons between linear slip-weakening and such rate-and-state friction laws have shown similar behaviour in terms of slip, stress drop and frequency content when comparable parameters and fracture energy densities are used (Bizzarri, 2011). Nevertheless, assessing the sensitivity to the choice of friction law, including to fast-velocity weakening rate-and-state friction, will require additional simulations and is beyond the scope of the present study. A possible limitation could also be the length scales of the heterogeneities we explore in this study. Since some heterogeneities (e.g., Models 3 and 5) have been included to also explore their impacts on the higher frequencies around the resolved frequencies of these modes (~ 1 Hz), they are not perturbations of corresponding wavelengths to the target long periods. Furthermore, it is possible that some of the observed pulse orientation variability is due to the potential misalignment of stations and the overturning of instruments during the strong shaking, such as station 3138 (Ertuncay & Costa, 2024; Yen et al., 2025).

7 Conclusions

We investigate whether different forms of on-fault complexity in 3D dynamic rupture simulations can reproduce the observed variability of long-period near-fault velocity pulses during the 2023 M_w 7.8 Kahramanmaraş earthquake. To this end, we design a suite of rupture scenarios in which we vary fault roughness, large-scale waviness, heterogeneous fracture energy, and supershear versus subshear initiation, while maintaining comparable seismic moment rate release and moment magnitude, and a reasonable fit to observed near-fault long-period velocity pulse amplitude variability. Across the tested on-fault heterogeneities, we mostly do not observe a systematic increase in variability in modelled long-period velocity pulse orientations. In contrast, local supershear rupture speeds, when present near a station, affect pulse orientation and period, and may be a primary driver of the commonly observed long-period pulse variability. Overall, the modelled pulses remain predominantly fault-normal in most of our scenarios, implying that the orientation variability seen in observations may not be reproduced by on-fault heterogeneity alone. Nonetheless, these physics-based 3D dynamic rupture simulations provide a framework to systematically test the processes controlling near-fault ground motions and offer insight into which physical mechanisms may be responsible for observational features. The systematic absence of increased orientation variability across five distinct on-fault heterogeneities constrains where that variability must originate. This points to fault zone structure, off-fault damage and site response as the most likely candidates, with important implications for physics-based, non-ergodic ground motion models accounting for near-fault long-period velocity pulses.

Open Research Section

The dynamic rupture simulations were performed using SeisSol (`www.seissol.org`), an open-source software freely available to download from `https://github.com/SeisSol/SeisSol/`. We use SeisSol, commit 01ae1b1. All data required to reproduce the dynamic rupture scenarios (i.e. computational mesh and SeisSol input files) can be downloaded from the Zenodo repository (Preca Trapani et al., 2026). Instructions for downloading, installing, and running the code are available in the SeisSol documentation at `https://seissol.readthedocs.io/`. Downloading and compiling instructions are at `https://seissol.readthedocs.io/en/latest/build-seissol.html`. Instructions for setting up and running simulations are at `https://seissol.readthedocs.io/en/latest/configuration.html`. Quickstart containerised installations and introductory materials are provided in the Docker container and Jupyter notebooks at `https://github.com/SeisSol/Training`. Example problems and model configuration files are provided at `https://github.com/SeisSol/Examples`, many of which reproduce the SCEC 3D Dynamic Rupture benchmark problems described at `https://strike.scec.org/cvws/benchmark_descriptions.html`. The SimModeler software for meshing can be found at `https://www.simmetrix.com/simmodeler/`, and instructions for compiling PUMGen can be cloned from `https://github.com/SeisSol/PUMGen.wiki.git`. The pulse analysis code can be downloaded from `https://github.com/shocky0424/PulseClassification`. Strong ground motion data were downloaded from the ESM Database `https://esm-db.eu/#/home` (Mascandola et al., 2026). The nucleation location was taken from the Disaster and Emergency Management Authority (AFAD) database of Türkiye `https://deprem.afad.gov.tr/event-detail/408326`. The Sentinel-2 optical data is available from the European Space Agency website `https://scihub.copernicus.eu/dhus/#/home`. Maps were generated using Generic Mapping Tools v.6.5.0 (Wessel et al., 2019). All figures use colourmaps from Fabio Crameri's collection `https://www.fabiocrameri.ch/colourmaps/`.

Conflict of Interest

The authors declare no conflicts of interest relative to this study.

Acknowledgments

We thank the Editor Rachel E. Abercrombie, Associate Editor, and two anonymous reviewers for their constructive comments. We are thankful to Thomas Ulrich for his help in troubleshooting the SeisSol models, as well as Oona Scotti and Sebastien Hok for valuable discussions. This work received funding from the European Union's Horizon 2020 research and innovation programme under the Marie-Sklodowska-Curie grant agreement No. 101072699 - TREAD-ITN (https://tread-horizon.eu/). A.-A.G. acknowledges additional support from Horizon Europe (Geo-INQUIRE, grant no. 101058518, DT-Geo, grant no. 101058129, and ChEESE-2P, 101093038, EARTH-AID, grant no. 101291194), NSF (grants no. EAR-2143413, EAR-2121568, OAC-2139536, OAC-2311208, OAC-2603524, RISE-2531036), the U.S. Geological Survey (award G26AP00141), NASA (grant no. 80NSSC20K0495), the Statewide California Earthquake Center (SCEC), which is funded by NSF Cooperative Agreement EAR-2225216 and USGS Cooperative Agreement G26AC00077-00), the Cascadia Region Earthquake Science Center (CRESCENT), which is funded by NSF Cooperative Agreement EAR-2225286, and Pacific Gas and Electric Company (PG&E). B. W. acknowledges additional support from the IGPP Green's Foundation. The authors acknowledge the Gauss Centre for Supercomputing e.V. for providing computing time on the supercomputer SuperMUC-NG at the Leibniz Supercomputing Centre (www.lrz.de) in project pn49ha. Additional computing resources were provided by the Institute of Geophysics of LMU Munich (Oeser et al., 2006).

References

Abdelmeguid, M., Zhao, C., Yalcinkaya, E., Gazetas, G., Elbanna, A., & Rosakis, A. (2023). Dynamics of episodic supershear in the 2023 m7.8 kahramanmaraş/pazarcik earthquake, revealed by near-field records and computational modeling. *Communications Earth and Environment*, *4*(456). doi: https://doi.org/10.1038/s43247-023-01131-7

Akinci, A., Dindar, A. A., Bal, I. E., Ertuncay, D., Smyrou, E., & Cheloni, D. (2025). Characteristics of strong ground motions and structural damage patterns from the february 6th, 2023 kahramanmaraş earthquakes, türkiye. *Natural Hazards*, *121*, 1209–1239. Retrieved from `https://doi.org/10.1007/s11069-024-06856-y` doi: 10.1007/s11069-024-06856-y

Akkar, S., & Gülkan, P. (2002, February). A critical examination of near-field accelerograms from the sea of marmara region earthquakes. *Bulletin of the Seismological Society of America*, *92*(1), 428–447. Retrieved from `https://doi.org/10.1785/0120000814` doi: 10.1785/0120000814

Anderson, E. M. (1905). The dynamics of faulting. *Transactions of the Edinburgh Geological Society*, *8*(3), 387–402.

Anderson, E. M. (1951). *The dynamics of faulting and dyke formation with applications to britain* (2nd ed.). Edinburgh: Oliver and Boyd.

Andrews, D. (2005). Rupture dynamics with energy loss outside the slip zone. *Journal of Geophysical Research: Solid Earth*, *110*(B1). doi: 10.1029/2004JB003191

Andrews, D. J. (1976). Rupture propagation with finite stress in antiplane strain. *Journal of Geophysical Research*, *81*(32), 3575-3582. doi: 10.1029/JB081i032p05679

Aochi, H., & Madariaga, R. (2003). The 1999 izmit, turkey, earthquake: Nonplanar fault structure, dynamic rupture process, and strong ground motion. *Bulletin of the Seismological Society of America*, *93*(3), 1249–1266.

Baker, J. W. (2007, October). Quantitative classification of near-fault ground motions using wavelet analysis. *Bulletin of the Seismological Society of America*, *97*(5), 1486–1501. Retrieved from `https://doi.org/10.1785/0120060255` doi: 10.1785/0120060255

Baltzopoulos, G., Baraschino, R., Chioccarelli, E., Cito, P., Vitale, A., & Iervolino, I. (2023). Near-source ground motion in the m7. 8 gaziantep (turkey) earthquake. *Earthquake Engineering & Structural Dynamics*, *52*(12), 3903–3912. Retrieved from `https://doi.org/10.1002/eqe.3939` doi: 10.1002/eqe.3939

Barbot, S., Luo, H., Wang, T., Hamiel, Y., Piatibratova, O., Javed, M. T., ... Gurbuz, G.

(2023). Slip distribution of the february 6, 2023 mw 7.8 and mw 7.6, kahramanmaraş, turkey earthquake sequence in the east anatolian fault zone. *Seismica*, *2*(3), 1–15. Retrieved from `https://doi.org/10.26443/seismica.v2i3.502` doi: 10.26443/seismica.v2i3.502

Ben-Zion, Y., & Sammis, C. G. (2003). Characterization of fault zones. *Pure Appl. Geophys.*, *160*, 677–715.

Biemiller, J., Gabriel, A.-A., & Ulrich, T. (2022). The dynamics of unlikely slip: 3d modeling of low-angle normal fault rupture at the mai'iu fault, papua new guinea. *Geochemistry, Geophysics, Geosystems*, *23*(5), e2021GC010298.

Bizzarri, A. (2010, 05). How to promote earthquake ruptures: Different nucleation strategies in a dynamic model with slip-weakening friction. *Bulletin of The Seismological Society of America - BULL SEISMOL SOC AMER*, *100*. doi: 10.1785/0120090179

Bizzarri, A. (2011). On the deterministic description of earthquakes. *Reviews of Geophysics*, *49*(3).

Bizzarri, A., & Cocco, M. (2003). Slip-weakening behavior during the propagation of dynamic ruptures obeying rate-and state-dependent friction laws. *Journal of Geophysical Research: Solid Earth*, *108*(B8).

Bizzarri, A., & Spudich, P. (2008). Effects of supershear rupture speed on the high-frequency content of s waves investigated using spontaneous dynamic rupture models and isochrone theory. *Journal of Geophysical Research: Solid Earth*, *113*(B5). doi: 10.1029/2007JB005146

Bommer, J. J., Abrahamson, N. A., Strasser, F. O., Pecker, A., Bard, P.-Y., et al. (2004). The challenge of defining upper bounds on earthquake ground motions. *Seismological Research Letters*, *75*(1), 82–95. doi: 10.1785/gssrl.75.1.82

Bray, J. D., & Rodriguez-Marek, A. (2004). Characterization of forward-directivity ground motions in the near-fault region. *Soil Dynamics and Earthquake Engineering*, *24*(11), 815–828. doi: 10.1016/j.soildyn.2004.05.001

Breuer, A., Heinecke, A., Rettenberger, S., Bader, M., Gabriel, A.-A., & Pelties, C. (2014). Sustained petascale performance of seismic simulations with seissol on supermuc. In *Proceedings of the international supercomputing conference* (pp. 1–18). Cham: Springer International Publishing. doi: 10.1007/978-3-319-07518-1_1

Candela, T., Ampuero, J. P., Van Wees, J. D., Fokker, P., & Wassing, B. (2019). Semi-analytical fault injection model: effect of fault roughness and injection scheme on induced seismicity. In *European geothermal conference* (pp. 11–14).

Candela, T., Renard, F., Bouchon, M., Brouste, A., Marsan, D., Schmittbuhl, J., & Voisin, C. (2009). Characterization of fault roughness at various scales: Implications of three-dimensional high resolution topography measurements. In *Mechanics, structure and evolution of fault zones* (pp. 1817–1851). Springer. doi: 10.1007/s00024-009-0521-2

Candela, T., Renard, F., Klinger, Y., Mair, K., Schmittbuhl, J., & Brodsky, E. E. (2012). Roughness of fault surfaces over nine decades of length scales. *Journal of Geophysical Research: Solid Earth*, *117*(B8). doi: 10.1029/2011JB009041

Cao, Z., Wei, J., Sun, Z., & Song, W. (2025). Spatial characteristic analysis of near-fault velocity pulses based on simulation of earthquake ground motion fields. *Buildings*, *15*(8), 1363. doi: https://doi.org/10.3390/buildings15081363

Chang, Z., Wu, H., Li, W., Yan, Z., Peng, L., & Zhu, G. (2025). Analysis of near-fault ground motions in the february 2023 kahramanmaraş, türkiye, earthquake sequence. *Bulletin of Earthquake Engineering*, *23*, 1349–1369. Retrieved from `https://doi.org/10.1007/s10518-025-02101-4` doi: 10.1007/s10518-025-02101-4

Chioccarelli, E., & Iervolino, I. (2010). Near-source seismic demand and pulse-like records: A discussion for l'aquila earthquake. *Earthquake Engineering & Structural Dynamics*, *39*(9), 1039–1062. doi: https://doi.org/10.1002/eqe.987

Cocco, M., & Bizzarri, A. (2002). On the slip-weakening behavior of rate-and state dependent constitutive laws. *Geophysical Research Letters*, *29*(11), 11–1.

Cork, T. G., Kim, J. H., Mavroeidis, G. P., Kim, J. K., Halldorsson, B., & Papageorgiou, A. S. (2016). Effects of tectonic regime and soil conditions on the pulse period of

near-fault ground motions. *Soil Dynamics and Earthquake Engineering*, *80*, 102–118. doi: https://doi.org/10.1016/j.soildyn.2015.09.011

Das, S., & Aki, K. (1977, 09). A numerical study of two-dimensional spontaneous rupture propagation. *Geophysical Journal International*, *50*(3), 643-668. Retrieved from https://doi.org/10.1111/j.1365-246X.1977.tb01339.x doi: 10.1111/j.1365-246X.1977.tb01339.x

Daubechies, I. (1993). Orthonormal bases of compactly supported wavelets ii. variations on a theme. *SIAM journal on mathematical analysis*, *24*(2), 499–519.

Day, S. M. (1982, December). Three-dimensional simulation of spontaneous rupture: The effect of nonuniform prestress. *Bulletin of the Seismological Society of America*, *72*(6A), 1881–1902. Retrieved 2024-02-07, from https://doi.org/10.1785/BSSA07206A1881 doi: 10.1785/BSSA07206A1881

Delouis, B., van den Ende, M., & Ampuero, J.-P. (2024). Kinematic rupture model of the february 6th 2023 mw7.8 turkey earthquake from a large set of near-source strong motion records combined with gnss offsets reveals intermittent supershear rupture. *Bulletin of the Seismological Society of America*, *114*(2), 726–741. Retrieved from https://doi.org/10.1785/0120230077 doi: 10.1785/0120230077

Dieterich, J. H. (1979). Modeling of rock friction: 1. experimental results and constitutive equations. *Journal of Geophysical Research: Solid Earth*, *84*(B5), 2161–2168.

Dumbser, M., & Käser, M. (2006). An arbitrary high-order discontinuous galerkin method for elastic waves on unstructured meshes — ii. the three-dimensional isotropic case. *Geophysical Journal International*, *167*(1), 319–336. doi: 10.1111/j.1365-246X.2006.03120.x

Dunham, E. M., Belanger, D., Cong, L., & Kozdon, J. E. (2011). Earthquake ruptures with strongly rate-weakening friction and off-fault plasticity, part 2: Nonplanar faults. *Bulletin of the Seismological Society of America*, *101*(5), 2308–2322. doi: 10.1785/0120100076

Dunham, E. M., & Bhat, H. S. (2008). Attenuation of radiated ground motion and stresses from three-dimensional supershear ruptures. *Journal of Geophysical Research: Solid Earth*, *113*(B8). doi: https://doi.org/10.1029/2007JB005182

Ertuncay, D., & Costa, G. (2024). Analysis of impulsive ground motions from february 2023 kahramanmaraş earthquake sequence. *Bulletin of Earthquake Engineering*, *23*, 965–999. doi: https://doi.org/10.1007/s10518-024-01897-x

Fang, Z., & Dunham, E. M. (2013). Additional shear resistance from fault roughness and stress levels on geometrically complex faults. *Journal of Geophysical Research: Solid Earth*, *118*(7), 3642–3654. doi: 10.1002/jgrb.50262

Farr, T. G., Rosen, P. A., Caro, E., Crippen, R., Duren, R., Hensley, S., ... Alsdorf, D. (2007). The shuttle radar topography mission. *Reviews of Geophysics*, *45*(2). doi: https://doi.org/10.1029/2005RG000183

Fayjaloun, R., Causse, M., Voisin, C., Cornou, C., & Cotton, F. (2017). Spatial variability of the directivity pulse periods observed during an earthquake. *Bulletin of the Seismological Society of America*, *107*(1), 308–318. doi: 10.1785/0120160199

Gabriel, A.-A., Ampuero, J.-P., Dalguer, L., & Mai, P. M. (2013). Source properties of dynamic rupture pulses with off-fault plasticity. *Journal of Geophysical Research: Solid Earth*, *118*(8), 4117–4126. doi: 10.1002/jgrb.50213

Gabriel, A.-A., Ampuero, J.-P., Dalguer, L. A., & Mai, P. M. (2012). The transition of dynamic rupture styles in elastic media under velocity-weakening friction. *Journal of Geophysical Research: Solid Earth*, *117*(B9). Retrieved from https://agupubs.onlinelibrary.wiley.com/doi/abs/10.1029/2012JB009468 doi: https://doi.org/10.1029/2012JB009468

Gabriel, A.-A., Garagash, D. I., Palgunadi, K. H., & Mai, P. M. (2024). Fault size–dependent fracture energy explains multiscale seismicity and cascading earthquakes. *Science*, *385*(6707), eadj9587. doi: 10.1126/science.adj9587

Gabriel, A.-A., Kurapati, V., Niu, Z., Schliwa, N., Schneller, D., Ulrich, T., ... Bader, M. (2025, June). *Seissol*. Zenodo. Retrieved from https://doi.org/10.5281/

zenodo.15685917 doi: 10.5281/zenodo.15685917
Gabriel, A.-A., Ulrich, T., Marchandon, M., Biemiller, J., & Rekoske, J. (2023, 12). 3d dynamic rupture modeling of the 6 february 2023, kahramanmaraş, turkey mw 7.8 and 7.7 earthquake doublet using early observations. *The Seismic Record*, *3*(4), 342-356.
Galis, M., Pelties, C., Kristek, J., Moczo, P., Ampuero, J.-P., & Mai, P. M. (2015). On the initiation of sustained slip-weakening ruptures by localized stresses. *Geophysical Journal International*, *200*(2), 890–909. doi: 0.1093/gji/ggu436
Gallovič, F., & Ľ. Valentová. (2023). Broadband strong ground motion modeling using planar dynamic rupture with fractal parameters. *Journal of Geophysical Research: Solid Earth*. (First published: 16 May 2023) doi: 10.1029/2023JB026506
Galvez, P., Ampuero, J.-P., Dalguer, L. A., Somala, S. N., & Nissen-Meyer, T. (2014). Dynamic earthquake rupture modelled with an unstructured 3-d spectral element method applied to the 2011 m 9 tohoku earthquake. *Geophysical Journal International*, *198*(2), 1222–1240. doi: 10.1093/gji/ggu203
Graves, R., & Pitarka, A. (2016). Kinematic ground-motion simulations on rough faults including effects of 3d stochastic velocity perturbations. *Bulletin of the Seismological Society of America*, *106*(5), 2136–2153. Retrieved from https://doi.org/10.1785/0120160088 doi: 10.1785/0120160088
Güvercin, S. E., Karabulut, H., Konca, A. O., Doğan, U., & Ergintav, S. (2022). Active seismotectonics of the east anatolian fault. *Geophysical Journal International*, *230*(1), 50–69. doi: https://doi.org/10.1093/gji/ggac045
Harris, R. A., & Abrahamson, N. A. (2014). Strong ground motions generated by earthquakes on creeping faults. *Geophysical Research Letters*, *41*(11), 3774–3780. doi: 10.1002/2014GL060228
Harris, R. A., Barall, M., Aagaard, B., Ma, S., Roten, D., Olsen, K., ... others (2018). A suite of exercises for verifying dynamic earthquake rupture codes. *Seismological Research Letters*, *89*. doi: 10.1785/0220170222
Heaton, T. H., Hall, J. F., Wald, D. J., & Halling, M. W. (1995). Response of high-rise and base-isolated buildings to hypothetical mw 7.0 blind thrust earthquake. *Science*, *267*, 206–211. Retrieved from https://doi.org/10.1126/science.267.5195.206 doi: 10.1126/science.267.5195.206
Heidbach, O., Tingay, M., Barth, A., Reinecker, J., Kurfeß, D., & Müller, B. (2010). Global crustal stress pattern based on the world stress map database release 2008. *Tectonophysics*, *482*(1-4), 3–15. doi: 10.1016/j.tecto.2009.07.023
Heinecke, A., Breuer, A., Rettenberger, S., Bader, M., Gabriel, A.-A., Pelties, C., ... Dubey, P. (2014, Nov.). Petascale high order dynamic rupture earthquake simulations on heterogeneous supercomputers. In *Sc '14: Proceedings of the international conference for high performance computing, networking, storage and analysis.* doi: 10.1109/SC.2014.6
Hu, J., Liu, M., Taymaz, T., Ding, L., & Irmak, T. S. (2025). Characteristics of strong ground motion from the 2023 mw 7.8 and mw 7.6 kahramanmaraş earthquake sequence. *Bulletin of Earthquake Engineering*, *23*(3), 1225–1254.
Hu, Z., Olsen, K. B., & Day, S. M. (2022). 0–5 Hz deterministic 3-D ground motion simulations for the 2014 La Habra, California, Earthquake. *Geophysical Journal International*, *230*, 2162–2182. (Advance Access publication 2022 May 10) doi: 10.1093/gji/ggac174
Ida, Y. (1972). Cohesive force across the tip of longitudinal-shear crack and griffith's specific surface energy. *Journal of Geophysical Research*, *77*(20), 3796-3805. doi: 10.1029/jb077i020p03796
Ide, S., & Aochi, H. (2005). Earthquakes as multiscale dynamic ruptures with heterogeneous fracture surface energy. *Journal of Geophysical Research: Solid Earth*, *110*(B11). doi: https://doi.org/10.1029/2004JB003591
Jia, Z., Jin, Z., Marchandon, M., Ulrich, T., Gabriel, A.-A., Fan, W., ... Fialko, Y. (2023, 08). The complex dynamics of the 2023 kahramanmaraş, turkey, mw 7.8-7.7 earthquake doublet. *Science (New York, N.Y.)*, *381*, eadi0685. doi: https://doi.org/10.1126/

science.adi0685
Kaneko, Y., & Goto, H. (2022). The origin of large, long-period near-fault ground velocities during surface-breaking strike-slip earthquakes. *Geophysical Research Letters*, *49*(10). Retrieved from https://agupubs.onlinelibrary.wiley.com/doi/abs/10.1029/2022GL098029 doi: https://doi.org/10.1029/2022GL098029
Kohrangi, M., Vamvatsikos, D., & Bazzurro, P. (2019). Pulse-like versus non-pulse-like ground motion records: Spectral shape comparisons and record selection strategies. *Earthquake Engineering & Structural Dynamics*, *48*(1), 46-64. Retrieved from https://onlinelibrary.wiley.com/doi/abs/10.1002/eqe.3122 doi: https://doi.org/10.1002/eqe.3122
Koketsu, K., Miyake, H., Guo, Y., Kobayashi, H., Masuda, T., et al. (2016). Widespread ground motion distribution caused by rupture directivity during the 2015 gorkha, nepal earthquake. *Scientific Reports*, *6*, 28536. doi: 10.1038/srep28536
Krenz, L., Uphoff, C., Ulrich, T., Gabriel, A.-A., Abrahams, L. S., Dunham, E. M., & Bader, M. (2021). 3d acoustic-elastic coupling with gravity: The dynamics of the 2018 palu, sulawesi earthquake and tsunami. In *The international conference for high performance computing, networking, storage and analysis.* Association for Computing Machinery. doi: 10.1145/3458817.3476173
Lee, S.-J., Yeh, T.-Y., & Lin, Y.-Y. (2016, November). Anomalously large ground motion in the 2016 m_l 6.6 meinong, taiwan, earthquake: A synergy effect of source rupture and site amplification. *Seismological Research Letters*, *87*(6), 1319–1326. Retrieved from https://doi.org/10.1785/0220160082 doi: 10.1785/0220160082
Li, B., Palgunadi, K. H., Wu, B., Suhendi, C., Zhou, Y., Ghosh, A., & Mai, P. M. (2025). Rupture dynamics and velocity structure effects on ground motion during the 2023 türkiye earthquake doublet. *Communications Earth & Environment*, *6*(1), 228. doi: 10.1038/s43247-025-02205-4
Li, B., Wu, B., Bao, H., Oglesby, D. D., Ghosh, A., Gabriel, A.-A., ... Chu, R. (2022). Rupture heterogeneity and directivity effects in back-projection analysis. *Journal of Geophysical Research: Solid Earth*, *127*(3), e2021JB022663. doi: 0.1029/2021JB022663
Lin, P.-S., Chiou, B., Abrahamson, N., Walling, M., Lee, C.-T., & Cheng, C.-T. (2011). *Repeatable source, site, and path effects on the standard deviation for empirical ground-motion prediction models* (Journal Article No. 101(5)). U.S. Geological Survey. doi: 10.1785/0120090312
Lozos, J., Akçiz, S., & Ladage, H. (2025). Modeling the rupture dynamics of strong ground motion (¿ 1 g) in fault stepovers. *Tectonophysics*, *895*, 230580. Retrieved from https://doi.org/10.1016/j.tecto.2024.230580 doi: 10.1016/j.tecto.2024.230580
Madariaga, R. (1977, 12). High-frequency radiation from crack (stress drop) models of earthquake faulting. *Geophysical Journal International*, *51*(3), 625-651. Retrieved from https://doi.org/10.1111/j.1365-246X.1977.tb04211.x doi: 10.1111/j.1365-246X.1977.tb04211.x
Madden, E. H., Ulrich, T., & Gabriel, A.-A. (2022). The state of pore fluid pressure and 3-d megathrust earthquake dynamics. *Journal of Geophysical Research: Solid Earth*, *127*(4). doi: https://doi.org/10.1029/2021JB023382
Mai, P. M., Aspiotis, T., Aquib, T. A., Cano, E. V., Castro-Cruz, D., Espindola-Carmona, A., ... others (2023). The destructive earthquake doublet of 6 february 2023 in south-central türkiye and northwestern syria: Initial observations and analyses. *The Seismic Record*, *3*(2), 105–115. Retrieved from https://doi.org/10.1785/0320230007 doi: 10.1785/0320230007
Marchandon, M., Gabriel, A.-A., Chiaraluce, L., Tinti, E., Casarotti, E., & Biemiller, J. (2025). Forecasting 3d rupture dynamics of the alto tiberina low-angle normal fault, italy. *Seismica*, *4*(2). doi: 10.26443/seismica.v4i2.1603
Mascandola, C., Felicetta, C., Russo, E., Luzi, L., Lanzano, G., Sgobba, S., ... ORFEUS Strong-Motion SMC (2026). *Engineering Strong Motion Database (ESM), version 3.0.* Istituto Nazionale di Geofisica e Vulcanologia (INGV). doi: 10.13127/esm.3

Melgar, D., Taymaz, T., Ganas, A., Crowell, B. W., Öcalan, T., Kahraman, M., ... Altuntaş, C. (2023). Sub- and super-shear ruptures during the 2023 mw 7.8 and mw 7.6 earthquake doublet in se türkiye. *Seismica*, *2*(3), 1–10. Retrieved from https://doi.org/10.26443/seismica.v2i3.387 doi: 10.26443/seismica.v2i3.387

Ozkula, G., Dowell, R. K., Baser, T., Lin, J.-L., Numanoglu, O. A., Ilhan, O., ... Uludag, T. D. (2023). Field reconnaissance and observations from the february 6, 2023, turkey earthquake sequence. *Natural Hazards*, *119*(1), 663–700. Retrieved from https://doi.org/10.1007/s11069-023-06143-2 doi: 10.1007/s11069-023-06143-2

Palgunadi, K. H., Gabriel, A.-A., Garagash, D. I., Ulrich, T., & Mai, P. M. (2024). Rupture dynamics of cascading earthquakes in a multiscale fracture network. *Journal of Geophysical Research: Solid Earth*, *129*(3), e2023JB027578. doi: 10.1029/2023JB027578

Palgunadi, K. H., Gabriel, A.-A., Garagash, D. I., Ulrich, T., Schliwa, N., & Mai, P. M. (2025). Ground-motion characteristics of cascading earthquakes in a multiscale fracture network. *Bulletin of the Seismological Society of America*. doi: https://doi.org/10.1785/0120240281

Palmer, A. C., Rice, J. R., & Hill, R. (1973). The growth of slip surfaces in the progressive failure of over-consolidated clay. *Proceedings of the Royal Society of London. A. Mathematical and Physical Sciences*, *332*(1591), 527-548. Retrieved from https://royalsocietypublishing.org/doi/abs/10.1098/rspa.1973.0040 doi: 10.1098/rspa.1973.0040

Panella, D. S., Tornello, M. E., & Frau, C. D. (2017). A simple and intuitive procedure to identify pulse-like ground motions. *Soil Dynamics and Earthquake Engineering*, *94*, 234-243. doi: https://doi.org/10.1016/j.soildyn.2017.01.020

Paolucci, R., Pacor, F., Puglia, R., Ameri, G., Cauzzi, C., & Massa, M. (2011). Record processing in itaca, the new italian strong-motion database. In S. Akkar, P. Gülkan, & T. van Eck (Eds.), *Earthquake data in engineering seismology: Predictive models, data management and networks* (pp. 99–113). Dordrecht: Springer Netherlands. Retrieved from https://doi.org/10.1007/978-94-007-0152-6_8 doi: 10.1007/978-94-007-0152-6_8

Pelties, C., de la Puente, J., Ampuero, J.-P., Brietzke, G. B., & Käser, M. (2012). Three-dimensional dynamic rupture simulation with a high-order discontinuous galerkin method on unstructured tetrahedral meshes. *Journal of Geophysical Research: Solid Earth*, *117*(B2), B02309. doi: 10.1029/2011JB008857

Pelties, C., Gabriel, A.-A., & Ampuero, J.-P. (2014). Verification of an ader-dg method for complex dynamic rupture problems. *Geoscientific Model Development*, *7*(3), 847–866. doi: 10.5194/gmd-7-847-2014

Power, W., Tullis, T., Brown, S., Boitnott, G., & Scholz, C. (1987). Roughness of natural fault surfaces. *Geophysical Research Letters*, *14*(1), 29–32.

Power, W. L., & Tullis, T. E. (1991). Euclidean and fractal models for the description of rock surface roughness. *Journal of Geophysical Research: Solid Earth*, *96*(B1), 415–424. doi: 10.1029/90JB02107

Preca Trapani, R., Marchandon, M., Palgunadi, K. H., Wu, B., Yen, M.-H., Cotton, F., & Gabriel, A.-A. (2026). *Repository of "do 3d dynamic rupture models capture the variability in long-period velocity pulses? insights from the 2023 mw 7.8 kahramanmaraş earthquake".* Zenodo. Retrieved from https://doi.org/10.5281/zenodo.17193783 doi: 10.5281/zenodo.17193783

Reitman, N. G., Briggs, R. W., Barnhart, W. D., Hatem, A. E., Jobe, J. A. T., DuRoss, C. B., ... Akçiz, S. (2023). Rapid surface rupture mapping from satellite data: The 2023 kahramanmaraş, turkey (türkiye), earthquake sequence. *The Seismic Record*, *3*(4), 289–298. Retrieved from https://doi.org/10.1785/0320230029 doi: 10.1785/0320230029

Reitman, N. G., Briggs, R. W., Barnhart, W. D., Jobe, J. A., DuRoss, C. B., Hatem, A. E., ... Collett, C. M. (2023, June). *Fault rupture mapping of the 6 February 2023 Kahramanmaraş, Türkiye, earthquake sequence from satellite data (ver. 1.1, February 2024).* U.S. Geological Survey data release. (Version 1.1, updated February 2024) doi:

10.5066/P985I7U2

Ren, C., Wang, Z., Taymaz, T., Hu, N., Luo, H., Zhao, Z., ... Ding, H. (2024). Supershear triggering and cascading fault ruptures of the 2023 kahramanmaraş, türkiye, earthquake doublet. *Science*, *383*(6680), 305–311. Retrieved from https://doi.org/10.1126/science.adi1519 doi: 10.1126/science.adi1519

Renard, F., Voisin, C., Marsan, D., & Schmittbuhl, J. (2006). High resolution 3d laser scanner measurements of a strike-slip fault quantify its morphological anisotropy at all scales. *Geophysical Research Letters*, *33*(4). doi: 10.1029/2005GL025038

Rice, J. R. (1992). Chapter 20 fault stress states, pore pressure distributions, and the weakness of the san andreas fault. In B. Evans & T. fong Wong (Eds.), *Fault mechanics and transport properties of rocks* (Vol. 51, p. 475-503). Academic Press. Retrieved from https://www.sciencedirect.com/science/article/pii/S0074614208628351 doi: 10.1016/S0074-6142(08)62835-1

Rice, J. R., Sammis, C. G., & Parsons, R. (2005). Off-fault secondary failure induced by a dynamic slip pulse. *Bulletin of the Seismological Society of America*, *95*(1), 109–134. doi: 10.1785/0120030166

Ripperger, J., Ampuero, J.-P., Mai, P. M., & Giardini, D. (2007). Earthquake source characteristics from dynamic rupture with constrained stochastic fault stress. *Journal of Geophysical Research: Solid Earth*, *112*(B4).

Rodgers, A. J., Pitarka, A., Pankajakshan, R., Sjögreen, B., & Petersson, N. A. (2020). Regional-scale 3d ground-motion simulations of m w 7 earthquakes on the hayward fault, northern california resolving frequencies 0–10 hz and including site-response corrections. *Bulletin of the Seismological Society of America*, *110*(6), 2862–2881. Retrieved from https://doi.org/10.1785/0120200147 doi: 10.1785/0120200147

Rodriguez-Marek, A., & Bray, J. D. (2006). Seismic site response for near-fault forward directivity ground motions. *Journal of Geotechnical and Geoenvironmental Engineering*, *132*(12), 1611–1620. doi: 10.1061/(ASCE)1090-0241(2006)132:12(1611)

Rosakis, A., Abdelmeguid, M., & Elbanna, A. (2025). Near-field evidence for early supershear rupture of the m w 7.8 kahramanmaraş earthquake in turkey. *Nature Geoscience*, *18*(6), 534–541. Retrieved from https://doi.org/10.1038/s41561-025-01707-2 doi: 10.1038/s41561-025-01707-2

Roten, D., Olsen, K., Day, S., Cui, Y., & Fäh, D. (2014). Expected seismic shaking in los angeles reduced by san andreas fault zone plasticity. *Geophysical Research Letters*, *41*(8), 2769–2777. doi: 10.1002/2014GL059411

Ruina, A. (1983). Slip instability and state variable friction laws. *Journal of Geophysical Research: Solid Earth*, *88*(B12), 10359–10370.

Schliwa, N., Gabriel, A.-A., & Ben-Zion, Y. (2025). Shallow fault zone structure affects rupture dynamics and ground motions of the 2019 ridgecrest sequence to regional distances. *Journal of Geophysical Research: Solid Earth*, *130*(6), e2025JB031194. Retrieved from https://agupubs.onlinelibrary.wiley.com/doi/abs/10.1029/2025JB031194 doi: https://doi.org/10.1029/2025JB031194

Shahi, S. K., & Baker, J. W. (2011). An empirically calibrated framework for including the effects of near-fault directivity in probabilistic seismic hazard analysis. *Bulletin of the Seismological Society of America*, *101*(2), 742–755. doi: 10.1785/0120100090

Shahi, S. K., & Baker, J. W. (2014). An efficient algorithm to identify strong-velocity pulses in multicomponent ground motions. *Bulletin of the Seismological Society of America*, *104*(5), 2456-2466. doi: https://doi.org/10.1785/0120130191

Shi, Z., & Day, S. M. (2013). Rupture dynamics and ground motion from 3-d rough-fault simulations. *Journal of Geophysical Research: Solid Earth*, *118*. doi: 10.1002/jgrb.50094

Silahtar, A., Senkaya, M., & Karaaslan, H. (2025). Multi-criteria decision-making (mcdm) model for building damages in the kahramanmaraş 2023 earthquakes sequence based on soil, ground motion and earthquake source-path parameters. *Bulletin of Earthquake Engineering*, *23*(12), 5137–5159.

Simmetrix Inc. (2017). *SimModeler: Simulation Modeling Suite 11.0 Documentation* (Tech.

Rep.). Simmetrix Inc. Retrieved from https://www.simmetrix.com
Somerville, P. G., Smith, N. F., Graves, R. W., & Abrahamson, N. A. (1997). Modification of empirical strong ground motion attenuation relations to include the amplitude and duration effects of rupture directivity. *Seismological Research Letters*, *68*(1), 199–222. Retrieved from https://doi.org/10.1785/gssrl.68.1.199 doi: 10.1785/gssrl.68.1.199
Spudich, P., & Frazer, L. N. (1984). Use of ray theory to calculate high-frequency radiation from earthquake sources having spatially variable rupture velocity and stress drop. *Bulletin of the Seismological Society of America*, *74*(6), 2061–2082. doi: 10.1785/BSSA0740062061
Strasser, F. O., Abrahamson, N. A., & Bommer, J. J. (2009). Sigma: Issues, insights, and challenges. *Seismological Research Letters*, *80*(1), 40–56. doi: 10.1785/gssrl.80.1.40
Strasser, F. O., & Bommer, J. J. (2009, October). Review: Strong ground motions—have we seen the worst? *Bulletin of the Seismological Society of America*, *99*(5), 2613–2637. Retrieved from https://doi.org/10.1785/0120080300 doi: 10.1785/0120080300
Styron, R., & Pagani, M. (2020). The gem global active faults database. *Earthquake Spectra*, *36*(1_suppl), 160–180. doi: 10.1177/8755293020944182
Suppe, J. (2014). Fluid overpressures and strength of the sedimentary upper crust. *Journal of Structural Geology*, *69*, 481-492. Retrieved from https://www.sciencedirect.com/science/article/pii/S0191814114001552 (Fluids and Structures in Fold and Thrust Belts with Recognition of the Work of David V. Wiltschko) doi: https://doi.org/10.1016/j.jsg.2014.07.009
Taufiqurrahman, T., Gabriel, A.-A., Ulrich, T., Valentová, L., & Gallovič, F. (2022). Broadband dynamic rupture modeling with fractal fault roughness, frictional heterogeneity, viscoelasticity and topography: The 2016 mw 6.2 amatrice, italy earthquake. *Geophysical Research Letters*, *49*(22), e2022GL098872. doi: https://doi.org/10.1029/2022GL098872
Tinti, E., Casarotti, E., Ulrich, T., Taufiqurrahman, T., Li, D., & Gabriel, A. (2021). Constraining families of dynamic models using geological, geodetic and strong ground motion data: The Mw 6.5, October 30th, 2016, Norcia earthquake, Italy. *Earth and Planetary Science Letters*, *576*, 117237. doi: 10.1016/j.epsl.2021.117237
Türker, E., Yen, M.-H., Pilz, M., & Cotton, F. (2023, October). Significance of pulse-like ground motions and directivity effects in moderate earthquakes: The example of the mw 6.1 gölyaka-düzce earthquake on 23 november 2022. *Bulletin of the Seismological Society of America*, *114*(2), 955–964. Retrieved from https://doi.org/10.1785/0120230043 doi: 10.1785/0120230043
Ulrich, T., Gabriel, A.-A., Ampuero, J.-P., & Xu, W. (2019). Dynamic viability of the 2016 mw 7.8 kaikōura earthquake cascade on weak crustal faults. *Nature communications*, *10*(1), 1213.
Uphoff, C., Rettenberger, S., Bader, M., Madden, E. H., Ulrich, T., Wollherr, S., & Gabriel, A.-A. (2017). Extreme scale multi-physics simulations of the tsunamigenic 2004 sumatra megathrust earthquake. In *Proceedings of the international conference for high performance computing, networking, storage and analysis* (pp. 1–16). Denver, Colorado: ACM. doi: 10.1145/3126908.3126948
Vallée, M., Landès, M., Shapiro, N. M., & Klinger, Y. (2008). The 14 november 2001 kokoxili (tibet) earthquake: High-frequency seismic radiation originating from the transitions between sub-rayleigh and supershear rupture velocity regimes. *Journal of Geophysical Research: Solid Earth*, *113*(B7). doi: 10.1029/2007JB005520
Varolgüneş, S. (2026). Strong shaking, weak prediction: Design-spectrum exceedance and building damage in the 2023 kahramanmaraş earthquakes. *Applied Sciences*, *16*(19), 9529.
Vyas, J. C., Gabriel, A.-A., Ulrich, T., Mai, P. M., & Ampuero, J.-P. (2023). How does thermal pressurization of pore fluids affect 3d strike-slip earthquake dynamics and ground motions? *Bulletin of the Seismological Society of America*, *113*(5), 1992–2008. doi: 10.1785/0120220205

Wessel, P., Luis, J. F., Uieda, L., Scharroo, R., Wobbe, F., Smith, W. H. F., & Tian, D. (2019). The generic mapping tools version 6. *Geochemistry, Geophysics, Geosystems*, *20*(11), 5556–5564. doi: 10.1029/2019GC008515

Withers, K. B., Olsen, K. B., Day, S. M., & Shi, Z. (2019). Ground motion and intraevent variability from 3d deterministic broadband (0–7.5 hz) simulations along a nonplanar strike-slip fault. *Bulletin of the Seismological Society of America*, *109*(1), 229–250. Retrieved from `https://doi.org/10.1785/0120180006` doi: 10.1785/0120180006

Withers, K. B., Olsen, K. B., Shi, Z., & Day, S. M. (2019). Validation of deterministic broadband ground motion and variability from dynamic rupture simulations of buried thrust earthquakes. *Bulletin of the Seismological Society of America*, *109*(1), 212–228. doi: 10.1785/0120180005

Wollherr, S., Gabriel, A., & Mai, P. M. (2019). Landers 1992 "reloaded": Integrative dynamic earthquake rupture modeling. *Journal of Geophysical Research: Solid Earth*, *124*(7), 6666–6702. doi: 10.1029/2018JB016355

Wollherr, S., Gabriel, A.-A., & Uphoff, C. (2018). Off-fault plasticity in three-dimensional dynamic rupture simulations using a modal discontinuous galerkin method on unstructured meshes: implementation, verification and application. *Geophysical Journal International*, *214*(3), 1556–1584. doi: 10.1093/gji/ggy213

Wu, B., Li, B., Zhang, H., Huang, S., Li, G., & Gabriel, A.-A. (2025). Near-fault strong-motion of the 2023 mw7.8 kahramanmaraş earthquake: Insights into high-frequency radiation mechanisms. *Journal of Geophysical Research: Solid Earth*, *130*(11). Retrieved from `https://agupubs.onlinelibrary.wiley.com/doi/abs/10.1029/2025JB031757` doi: https://doi.org/10.1029/2025JB031757

Wu, F., Xie, J., An, Z., Lyu, C., Taymaz, T., Irmak, T. S., ... Zhou, B. (2023). Pulse-like ground motion observed during the 6 february 2023 mw7. 8 pazarcık earthquake (kahramanmaraş, se türkiye). *Earthquake Science*, *36*(4), 328–339. doi: https://doi.org/10.1016/j.eqs.2023.05.005

Yaghmaei-Sabegh, S. (2010). Detection of pulse-like ground motions based on continues wavelet transform. *Journal of seismology*, *14*(4), 715–726.

Yao, S., & Yang, H. (2023). Towards ground motion prediction for potential large earthquakes from interseismic locking models. *Earth and Planetary Science Letters*, *601*, 117905. doi: 10.1016/j.epsl.2022.117905

Yeh, T.-Y., & Olsen, K. B. (2024). Simulation of 0–7.5 hz physics-based nonlinear ground motions for maximum credible earthquake scenarios at the long valley dam, ca. *Earthquake Spectra*, *40*(2), 1479–1506. doi: https://doi.org/10.1177/87552930231226135

Yen, M., Türker, E., Ulrich, T., Marchandon, M., Gabriel, A.-A., & Cotton, F. (2025). An analysis of directivity pulses using empirical data and dynamic rupture simulations of the 2023 kahramanmaras earthquake doublet. *Earthquake Spectra*, 1–20. doi: 10.1177/87552930241305012

Yen, M., von Specht, S., Lin, Y., Cotton, F., & Ma, K. (2021, 09). Within- and between-event variabilities of strong-velocity pulses of moderate earthquakes within dense seismic arrays. *Bulletin of the Seismological Society of America*, *112*(1), 361-380. Retrieved from `https://doi.org/10.1785/0120200376` doi: 10.1785/0120200376

Yucel, B., Hernández-Aguirre, V. M., Odabasi, O., Kohrangi, M., Vanini, M., Smerzini, C., ... Bazzurro, P. (2026). Investigating the 2023 m w 7.8 kahramanmaraş earthquake ground motion through 3d physics-based numerical simulations. *Bulletin of the Seismological Society of America*, *116*(5), 2072–2090.

Zhao, C., Mia, M. S., Elbanna, A., & Ben-Zion, Y. (2024). Dynamic rupture modeling in a complex fault zone with distributed and localized damage. *Mech. Mater.*, *198*, 105139.

Supporting Information for "Do 3D Dynamic Rupture Models Capture the Variability in Long-Period Velocity Pulses? Insights from the 2023 M_w 7.8 Kahramanmaraş Earthquake"

Rachel Preca Trapani[1], Mathilde Marchandon[1], Kadek Hendrawan Palgunadi[3,4], Baoning Wu[2], Ming-Hsuan Yen[5], Fabrice Cotton[5], Alice-Agnes Gabriel[2,1]

[1]Department of Earth and Environmental Sciences, Ludwig-Maximilians-Universität (LMU), Munich, Germany

[2]Scripps Institution of Oceanography, UC San Diego, La Jolla, CA, USA

[3]Swiss Seismological Service (SED), ETH Zürich, Switzerland

[4]Department of Geophysical Engineering, Institut Teknologi Sepuluh Nopember, Indonesia

[5]GFZ, Helmholtz Centre, Potsdam, Germany

Contents of this file

1. Details on the Supplementary Heterogeneous D_c Simulations
2. Figures S1 to S36
3. Tables S1 to S12

Corresponding author: R. Preca Trapani, Department of Earth and Environmental Sciences, Ludwig-Maximilian-Universität, Munich, Theresienstraße 41, Munich, 80333, Germany. (R.Preca@lmu.de)

4. References

Additional Supporting Information (Files uploaded separately)

1. Movies S1 and S2
2. Excel File S1

Introduction

This supplementary material includes a section describing the details of the supplementary simulations with different heterogeneous D_c distributions, a table defining the computational costs and mesh sizes of the models used in this study (Table S1), and a table describing the 1D velocity model used in this study (Table S2). Included here are tables showing the extracted pulse properties for stations classified as pulse-like in all six models and the ESM observational data (Tables S3–S9), two tables showing the details of the five candidate pulses extracted for each model and the ESM data at stations 3116 and 3142 (Tables S10 and S11), and a table summarising the details of the supplementary simulations (Table S12). This supplementary material also includes supplementary figures S1 - S36. Figure S1 compares the pulse map from the pulse analysis applied to the model from Jia et al. (2023), as depicted in Yen et al. (2025), to the reference model described in this study. Figure S2a further explains the initial stress orientation field, whilst Figure S2b shows a rupture speed fault output for a special case from the waviness model in which supershear rupture speeds were reached. Figure S3 shows the relative prestress ratio, $\mathcal{R}$. Figure S4 shows examples of the extracted pulse signals during the pulse extraction method. Figure S5 is similar to Figure S1 but shows the pulse amplitude instead of the peak rotated velocity (PRV). Figures S6 – S12 show the velocity waveforms for all six models and the observational data at all stations discussed in this study. Figures S13

– S31 show the original rotated waveforms and the corresponding extracted pulses for all six models and ESM data at all stations discussed in this study. Figure S32 is the same plot as Figure 10 but showing a comparison to the observed ground motion data, Figure S33 shows a comparison between the extracted pulse amplitude and PRV, and Figure S34 shows the Fourier spectra of the models. Figure S35 shows the rupture speed outputs for the supplementary D_c runs and their difference from the reference model, and Figure S36 shows a comparison of the extracted pulse properties of the supplementary D_c runs, Model 4 and the Reference Model. The corresponding captions to the separately included files can also be found in this file.

Captions of Supplementary Files

Movie S1: Evolution of absolute slip rate (m/s) for all six dynamic rupture models explored in this study.

Movie S2: Evolution of dynamic rupture speed (m/s) for all six dynamic rupture models explored in this study.

Excel File S1: Detailed outputs from the pulse analysis per station for the six main models and the observational ESM data.

1. Supplementary Heterogeneous D_c Simulations

We run several supplementary simulations with different heterogeneous distributions of D_c following Ide and Aochi (2005) to explore the impact of different scales of D_c heterogeneities. From a suite of 21 models, four models reproduce the rupture dynamics of the M_w 7.8 Kahramanmaraş reference simulation (see Table S12). We refer to these four models as Models R1, R2, R3 and R4. Model R1 includes the same D_c range as Model 4 with 7 families on both faults instead of 7 and 8 (see Section 4.3), whilst keeping

the average $D_c = 0.5$ m, as in Model 4 and the Reference Model. In order to keep this average, the D value had to be altered to $D = 1.1$ on the NPF and 1.9 on the EAF. Models R2 and R3 have an average $D_c = 0.7$ m across the entire faulting system with different ranges of D_c. Model R2 ranges from 0.2 m to 2 m, and Model 3 ranges from 0.1 m to 1 m. Model R4 has an average of $D_c = 0.8$ m across the whole faulting system with a D_c of 0.2 m to 2 m. These three models also vary the number of families and D values to allow for these different D_c averages, as well as different ranges of D_c. The rupture speed outputs can be seen in Figure S35, along with the corresponding pulse analysis in Figure S36, and we discuss these results in the main text Section 6.1.

References

Güvercin, S. E., Karabulut, H., Konca, A. O., Doğan, U., & Ergintav, S. (2022). Active seismotectonics of the east anatolian fault. *Geophysical Journal International*, *230*(1), 50–69. doi: https://doi.org/10.1093/gji/ggac045

Ide, S., & Aochi, H. (2005). Earthquakes as multiscale dynamic ruptures with heterogeneous fracture surface energy. *Journal of Geophysical Research: Solid Earth*, *110*(B11). doi: https://doi.org/10.1029/2004JB003591

Jia, Z., Jin, Z., Marchandon, M., Ulrich, T., Gabriel, A.-A., Fan, W., ... Fialko, Y. (2023, 08). The complex dynamics of the 2023 kahramanmaraş, turkey, mw 7.8-7.7 earthquake doublet. *Science (New York, N.Y.)*, *381*, eadi0685. doi: https://doi.org/10.1126/science.adi0685

Shahi, S. K., & Baker, J. W. (2014). An efficient algorithm to identify strong-velocity pulses in multicomponent ground motions. *Bulletin of the Seismological Society of America*, *104*(5), 2456-2466. doi: https://doi.org/10.1785/0120130191

Yen, M.-H., Türker, E., Ulrich, T., Marchandon, M., Gabriel, A.-A., & Cotton, F. (2025). An analysis of directivity pulses using empirical data and dynamic rupture simulations of the 2023 kahramanmaras earthquake doublet. *Earthquake Spectra*, 1–20. doi: 10.1177/87552930241305012

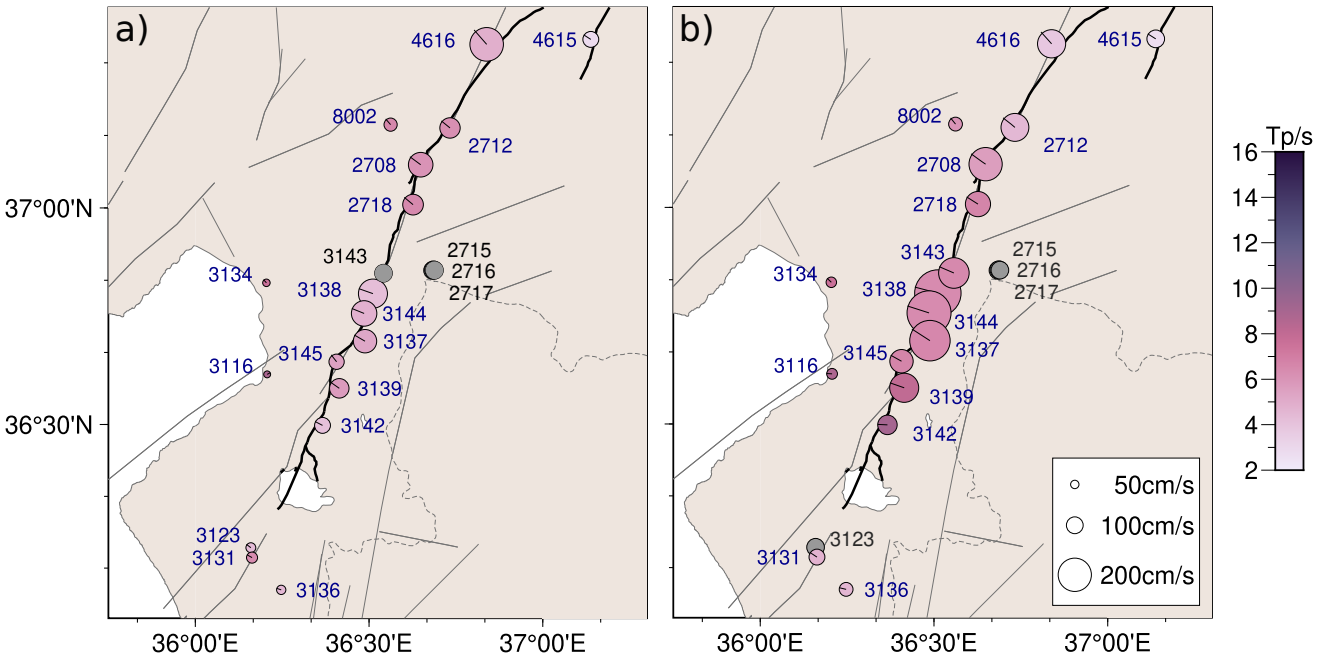


Figure S1. Comparison of the pulse maps for a) the Jia et al. (2023) model, as shown in Figure 1b and b) the reference model. There are some minor differences between a) and Figure 3a of Yen et al. (2025), such as slight variations in the precise pulse property values from the pulse analysis. This is mainly due to differences in operating systems and software versions. However, there is a notable difference in the pulse orientation for station 3116 and the negative classification of station 3143 as pulse-like here in a). These differences could be due to different approaches to the pre-processing of the synthetic data before applying the pulse analysis. In this study, no pre-processing is applied to the signals prior to the pulse analysis, whereas the signals were trimmed in the Yen et al. (2025) study. A change in total signal length can strongly influence the energy ratios used for the pulse criterion calculations, which are necessary for the Shahi and Baker (2014) pulse extraction method.

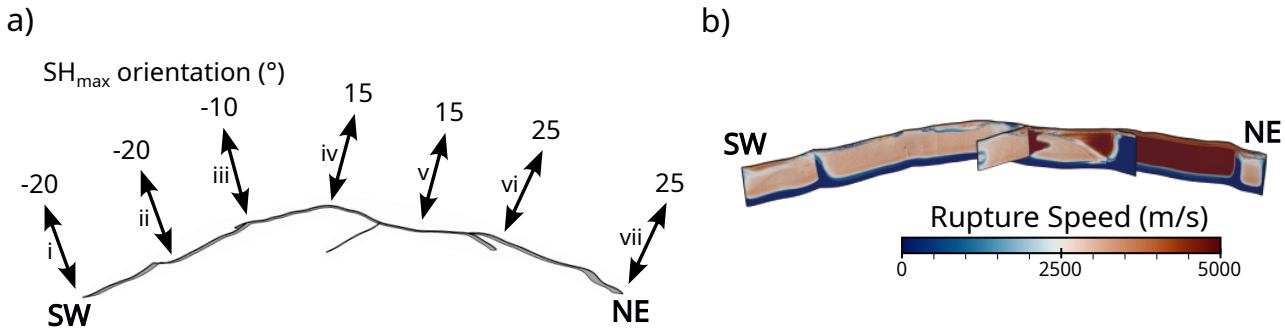


Figure S2. a) Distribution of SHmax orientations along the fault for the reference model. All models except for Model 3 follow this setup. b) A special case for Model 6 where the change in the $\mathcal{R}$ value results in supershear rupture speeds along the eastern portion of the EAF.

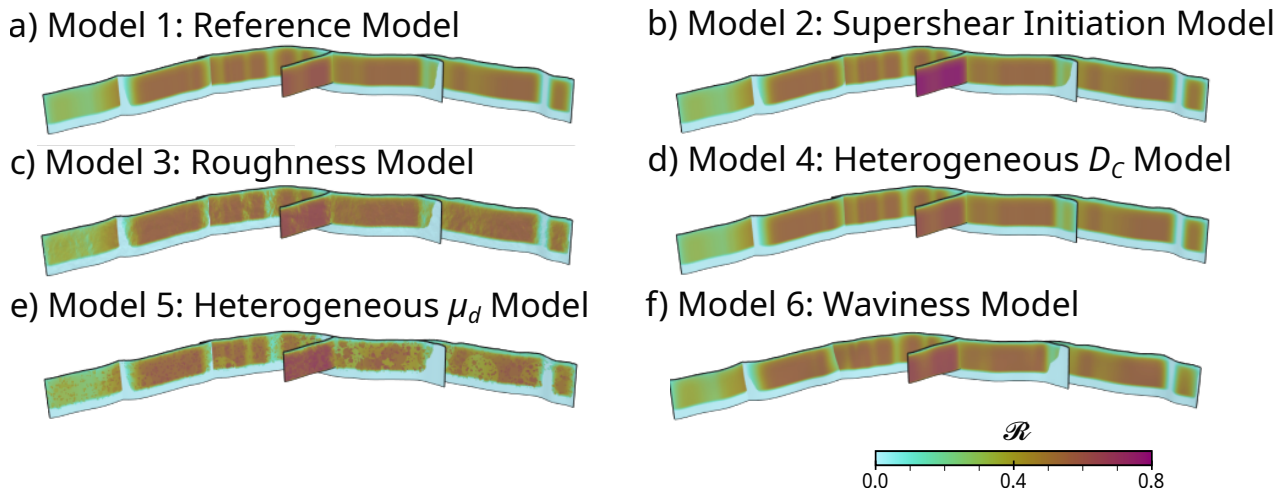


Figure S3. Relative prestress ratio ($\mathcal{R}$) for the six dynamic rupture models analysed in this study. Variations in $\mathcal{R}$ relative to the reference model (a) appear in Model 2: the supershear initiation model (b), which shows a higher $\mathcal{R}$ value along the NPF, Model 3: multi-scale roughness (c), Model 5: heterogeneous μ_d (e), and Model 6: large-scale waviness (f). Model 4: heterogeneous D_c (d) has a relative prestress ratio identical to that of the reference model.

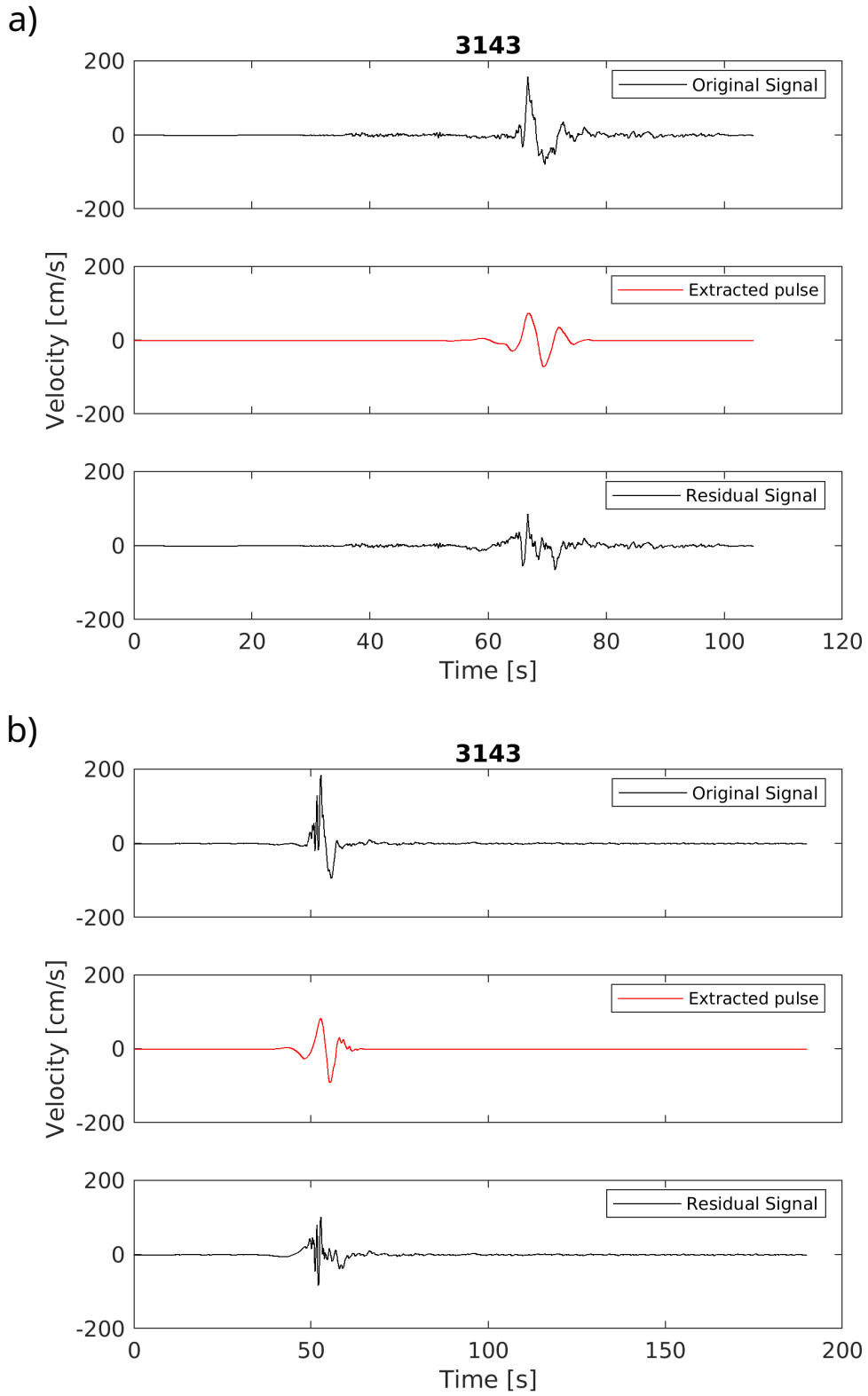


Figure S4. An example of the original signal generated during the pulse extraction method of Shahi and Baker (2014), the extracted pulse and the residual signal for station 3143 for a) the observational data and b) the reference model.

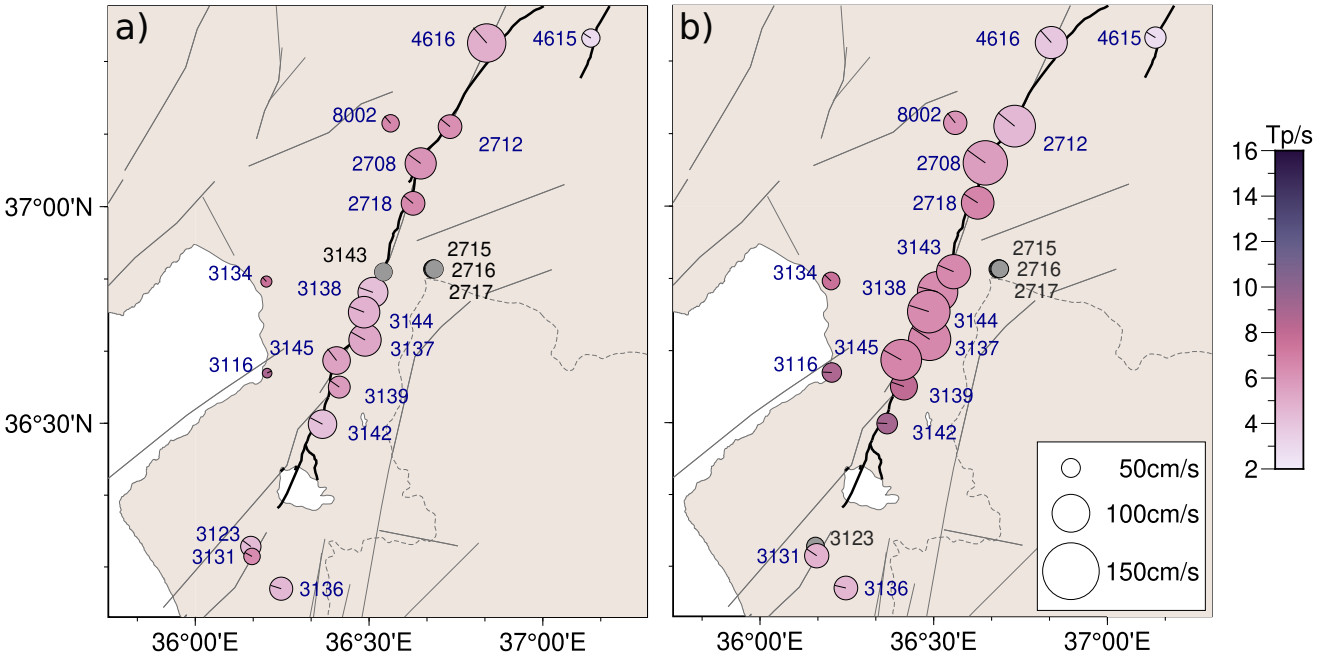


Figure S5. Comparison of the pulse maps for a) the Jia et al. (2023) model and b) the reference model as in Figure S1. Here, however, the circle size represents the extracted pulse amplitude rather than the peak rotated velocity (PRV).

Model	CPUh	Mesh Size [elements]
Model 1	10,590.0	31,452,737
Model 2	8,778.8	31,452,737
Model 3	10,680.0	52,370,578
Model 4	9,239.7	31,452,737
Model 5	8,873.8	31,452,737
Model 6	9,400.0	52,294,408

Table S1. Computational cost in CPU hours (CPUh) of all six 3D dynamic rupture models explored in this study, as well as the size of the associated computational mesh. Models 1, 2, 4, and 5 use the same computational mesh, whereas Models 3 and 6 use different meshes that incorporate the different fault roughness explored in each. All simulations are performed on 48 nodes with 48 CPUs of the supercomputer SuperMUC-NG. The computational cost is calculated as [CPUh] = [number of nodes] × [number of CPUs per node] × [computing time (hours)]

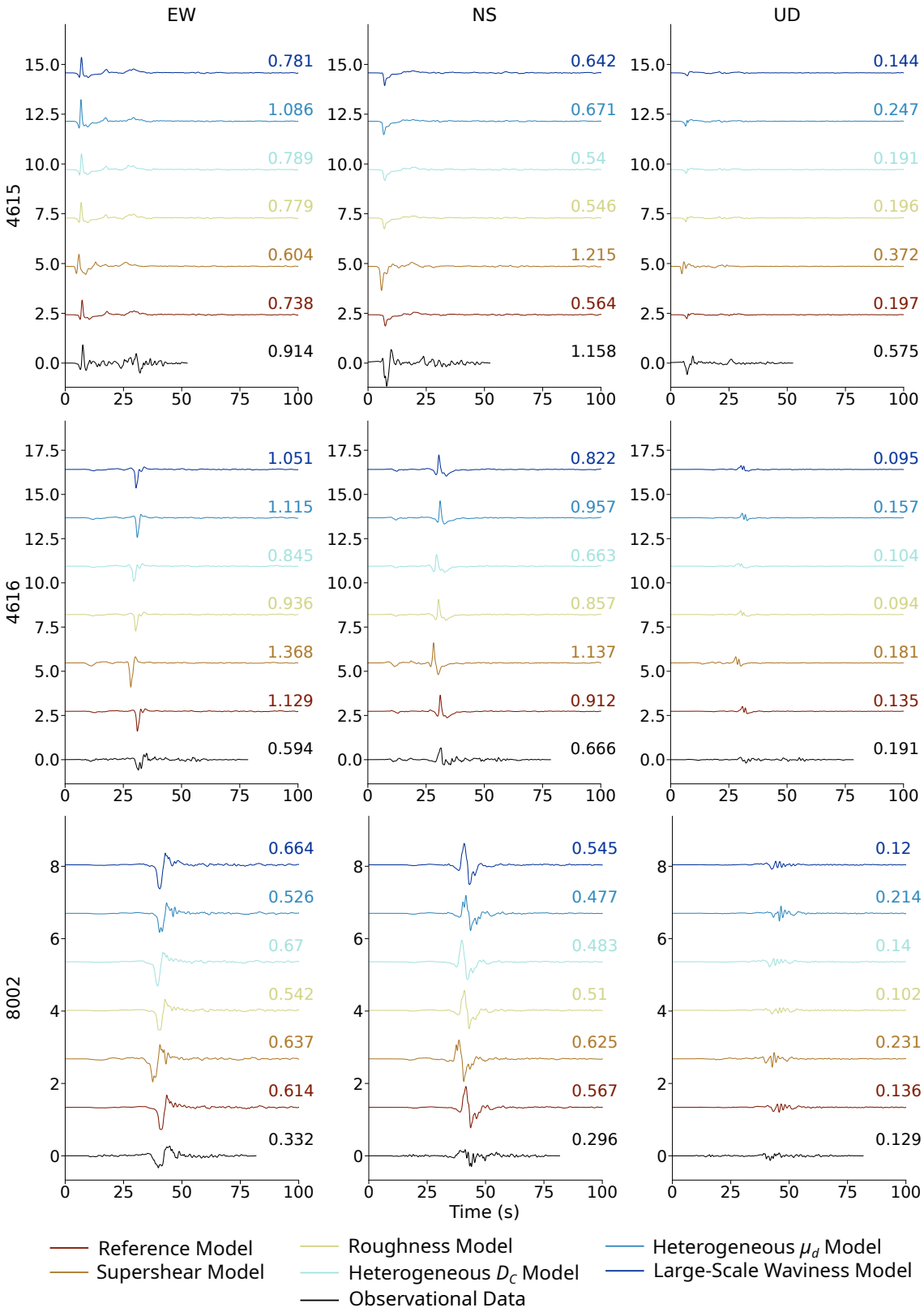


Figure S6. Velocity (m/s) waveforms for stations 4615, 4616 and 8002 from the horizontal and vertical components for the six simulations and the observational data. All waveforms are low-pass filtered at 1 Hz to align with the highest resolved frequencies of the models.

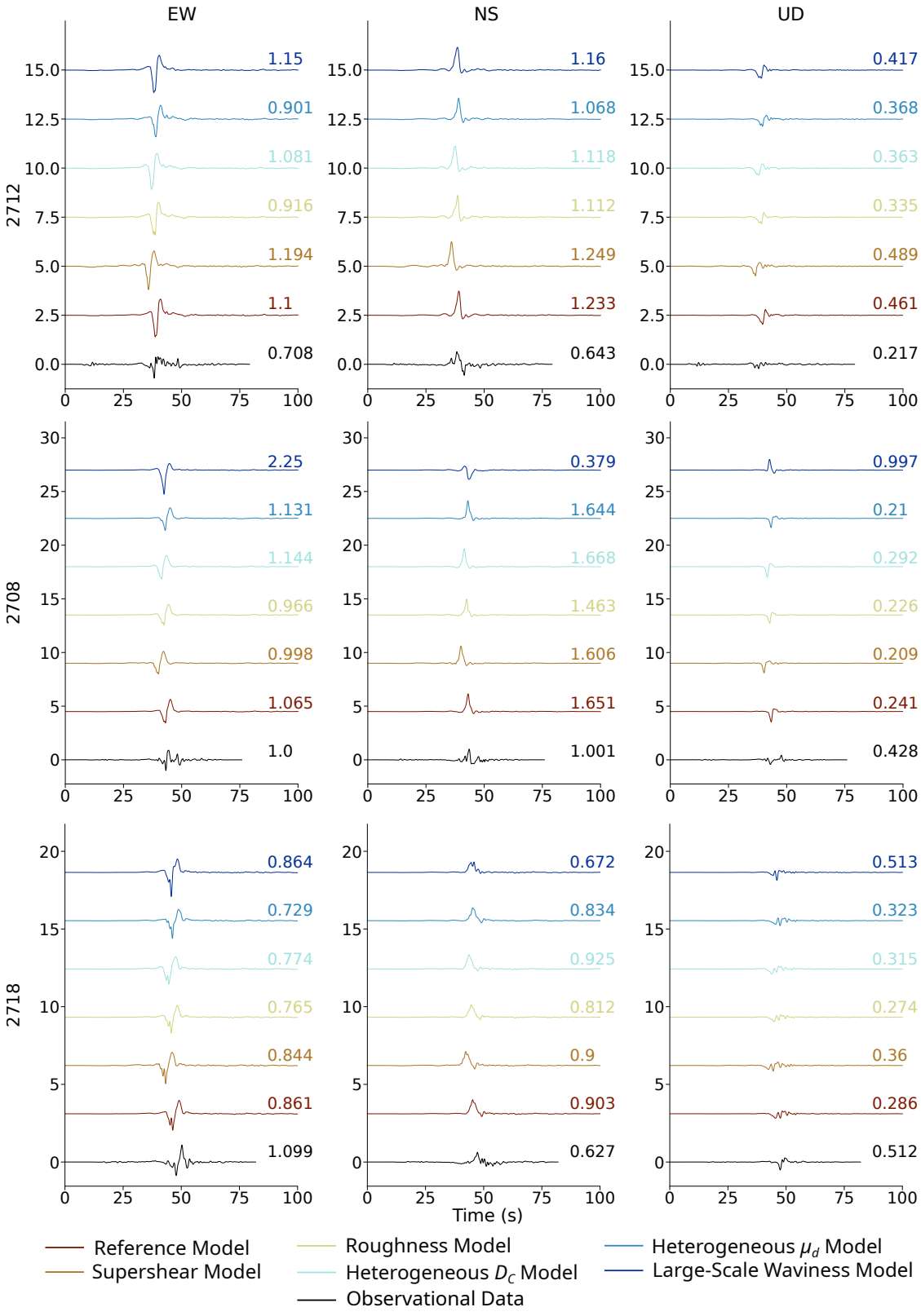


Figure S7. Velocity (m/s) waveforms for stations 2712, 2708 and 2718 from the horizontal and vertical components for the six simulations and the observational data. All waveforms are low-pass filtered at 1 Hz to align with the highest resolved frequencies of the models.

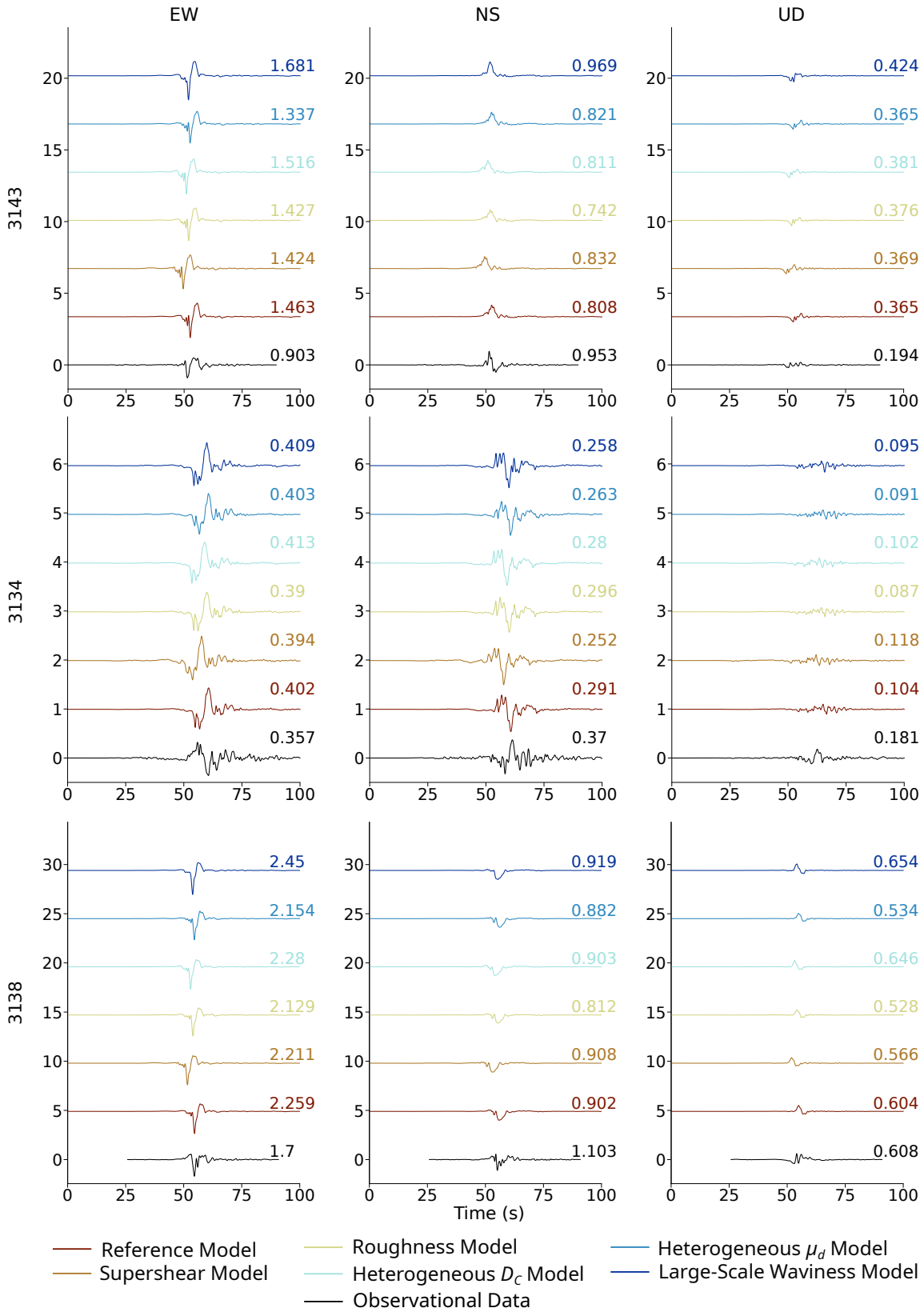


Figure S8. Velocity (m/s) waveforms for stations 3143, 3134 and 3138 from the horizontal and vertical components for the six simulations and the observational data. All waveforms are low-pass filtered at 1 Hz to align with the highest resolved frequencies of the models.

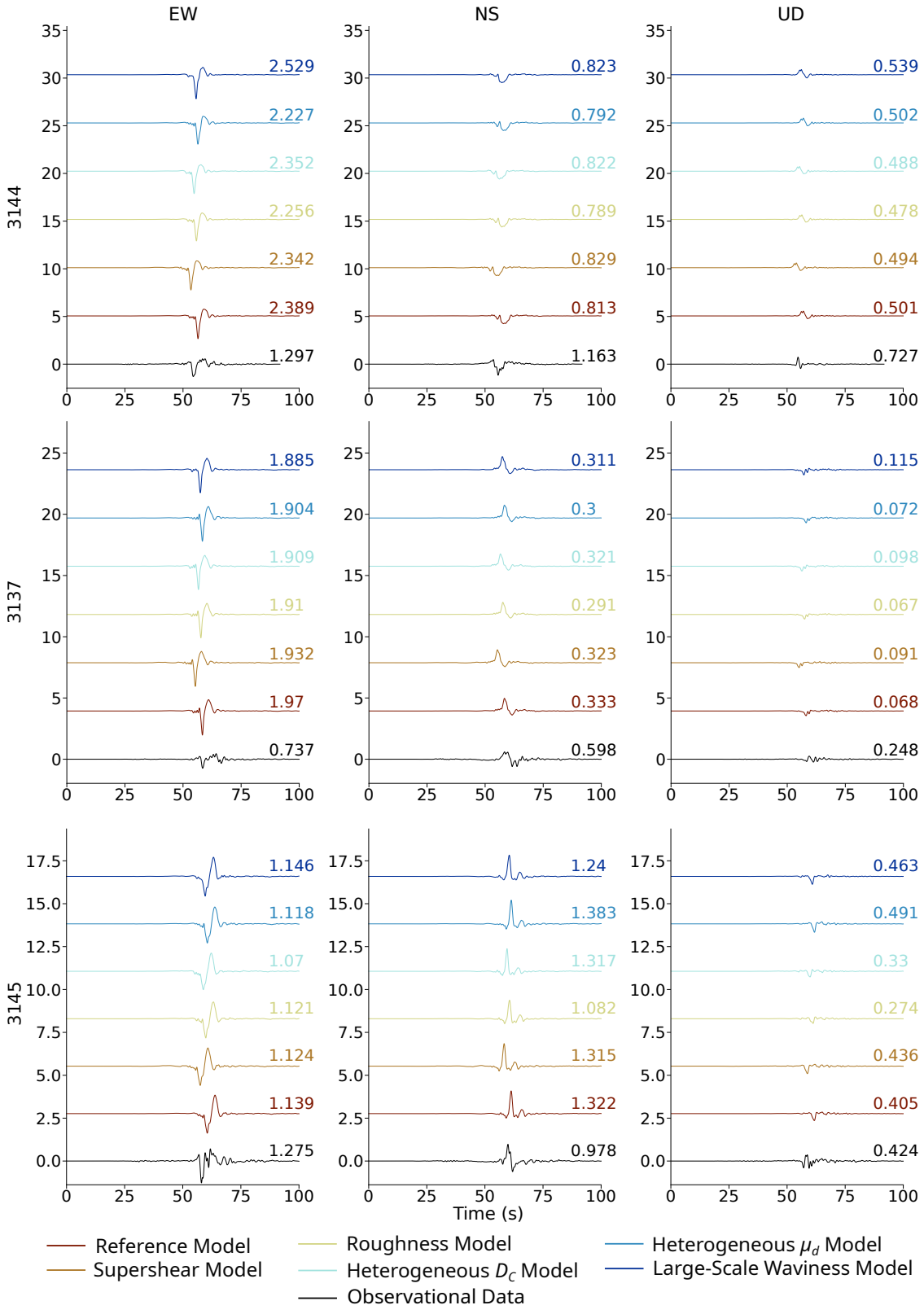


Figure S9. Velocity (m/s) waveforms for stations 3144, 3137 and 3145 from the horizontal and vertical components for the six simulations and the observational data. All waveforms are low-pass filtered at 1 Hz to align with the highest resolved frequencies of the models.

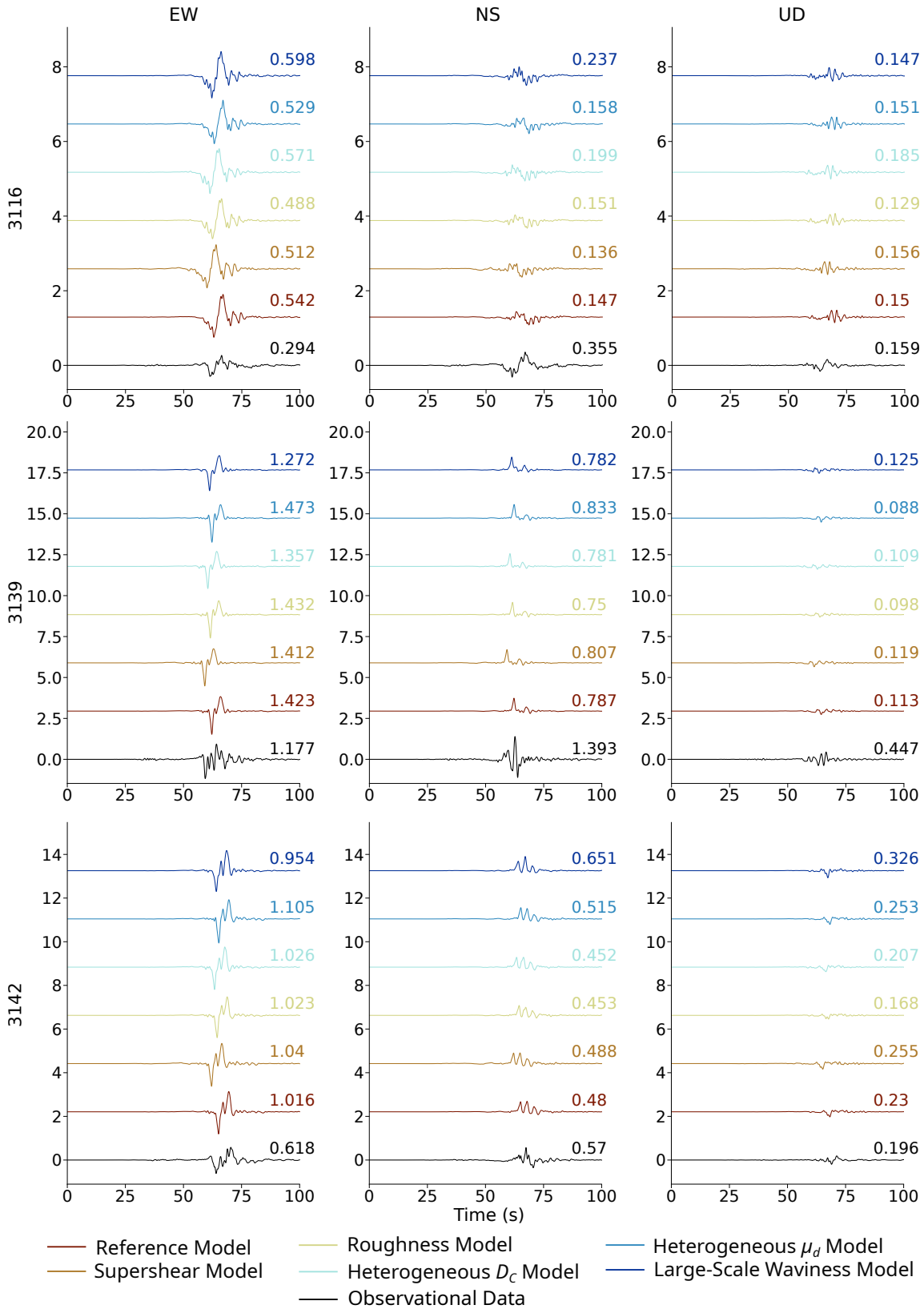


Figure S10. Velocity (m/s) waveforms for stations 3116, 3139 and 3142 from the horizontal and vertical components for the six simulations and the observational data. All waveforms are low-pass filtered at 1 Hz to align with the highest resolved frequencies of the models.

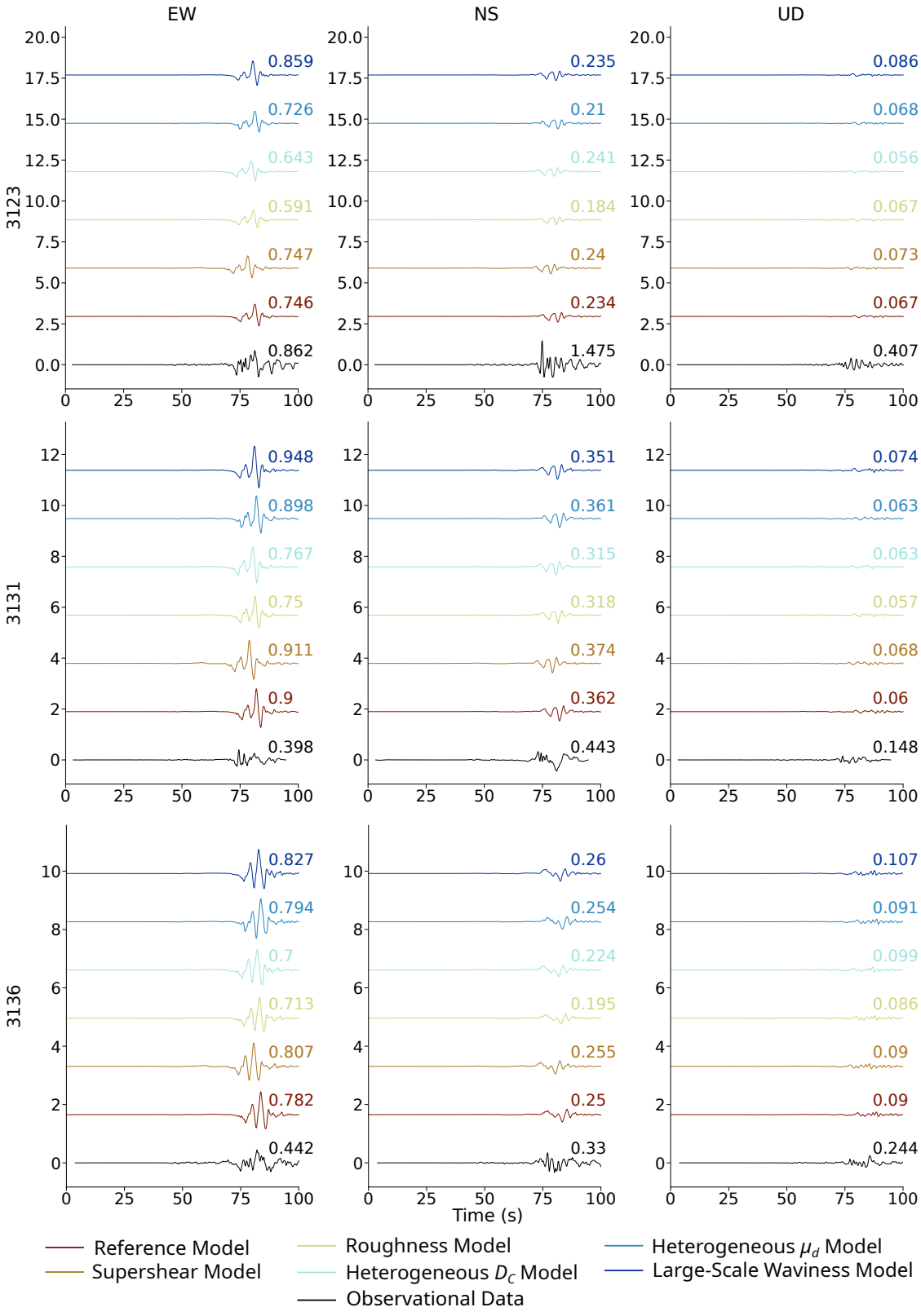


Figure S11. Velocity (m/s) waveforms for stations 3123, 3131 and 3136 from the horizontal and vertical components for the six simulations and the observational data. All waveforms are low-pass filtered at 1 Hz to align with the highest resolved frequencies of the models.

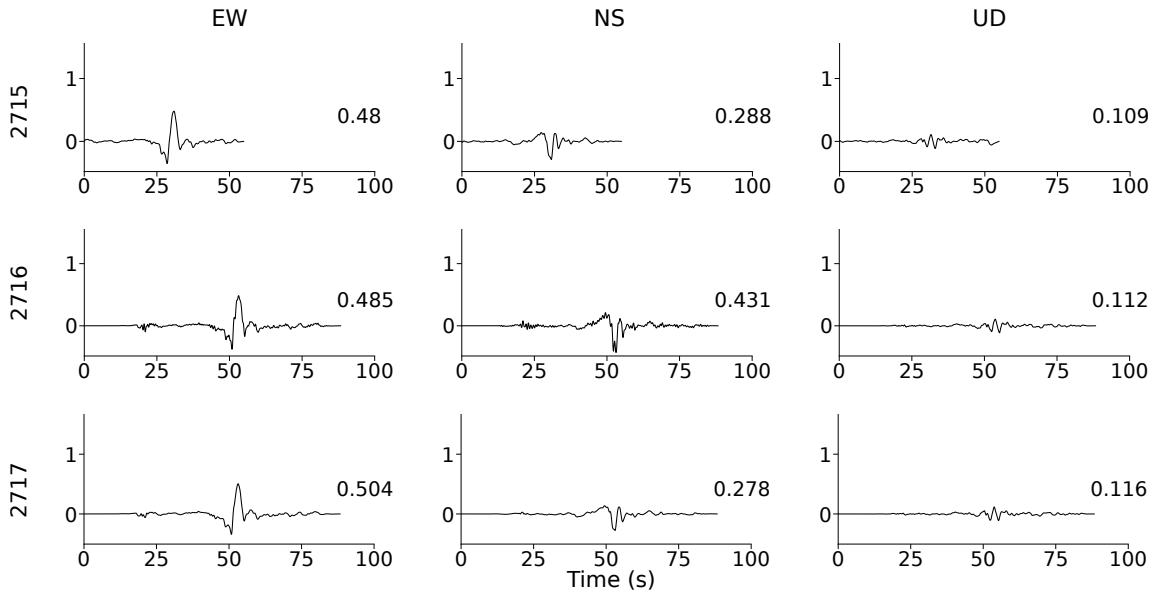


Figure S12. Velocity (m/s) waveforms for stations 2715, 2716 and 2717 from the observational dataset. These stations are included for completeness, as the corresponding synthetic waveforms are not available for these stations. All waveforms are low-pass filtered at 1 Hz to align with the highest resolved frequencies of the models.

Depth [km]	Density [kg m^{-3}]	c_s [km/s]	c_p [km/s]
1.0	2465.0	2.43	4.52
2.0	2640.2	3.03	5.62
4.0	2665.2	3.31	5.75
6.0	2685.3	3.38	5.85
8.0	2708.1	3.43	5.96
10.0	2716.7	3.44	6.00
12.0	2727.5	3.46	6.05
16.0	2789.0	3.62	6.32
20.0	2808.3	3.67	6.40
25.0	2920.1	3.92	6.83
30.0	2936.8	3.94	6.89
37.0	3221.2	4.40	7.80
45.0	3370.6	4.56	8.22
1000.0	3400.2	4.61	8.3

Table S2. Description of the 1D velocity model adapted from Güvercin et al. (2022) that we use in our models.

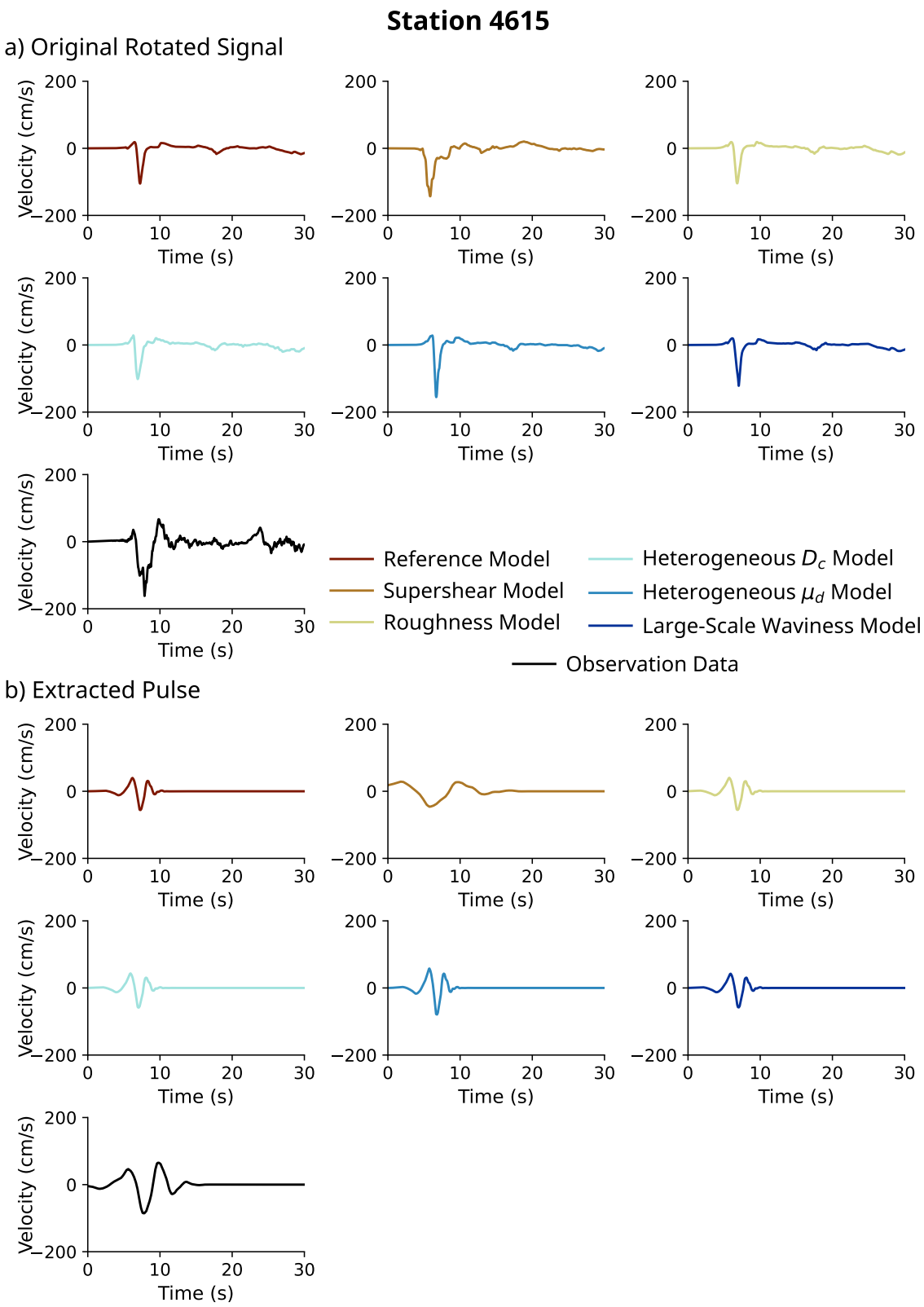


Figure S13. a) Original rotated signal and b) extracted pulse for station 4615 for the six models and the observational dataset.

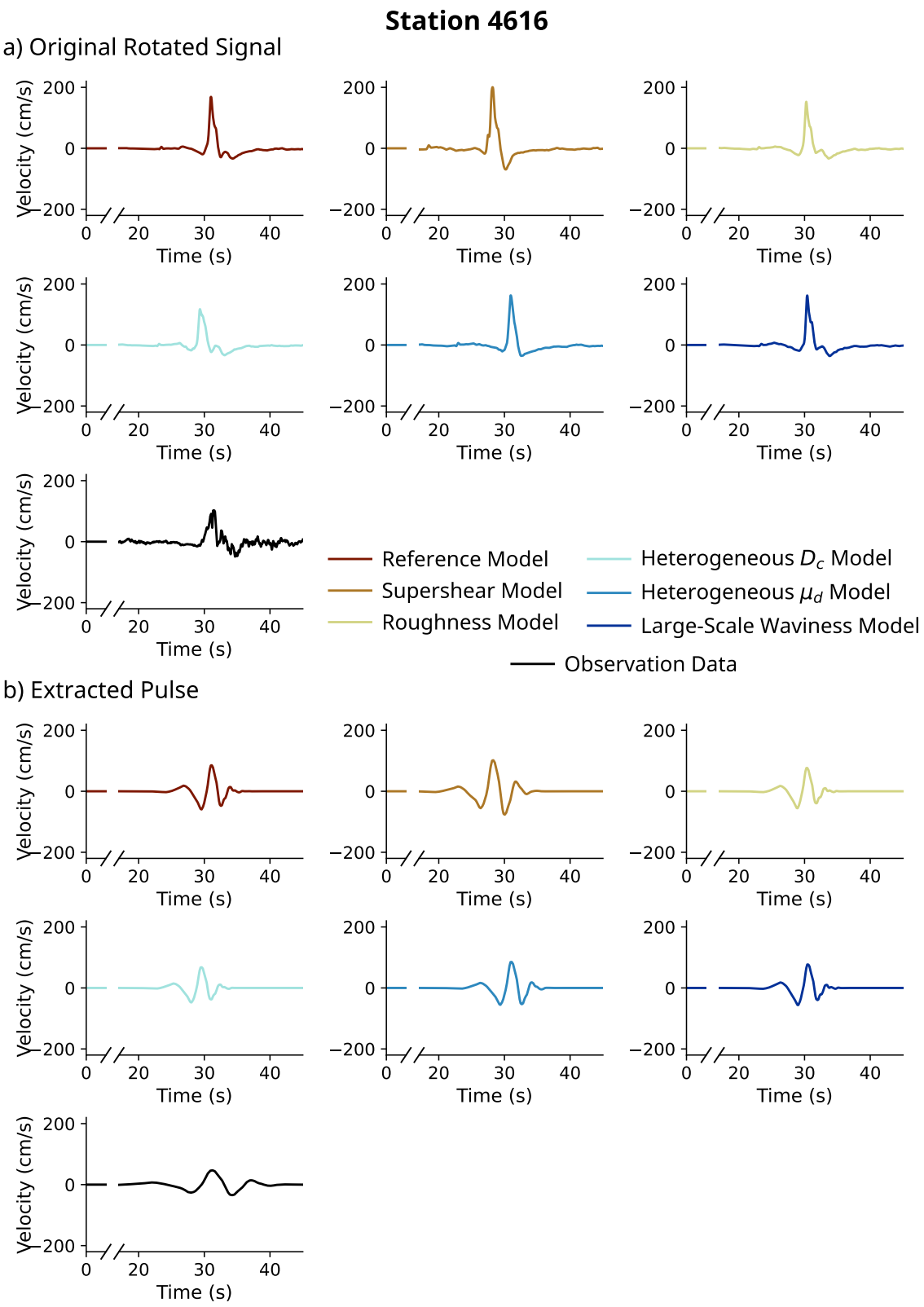


Figure S14. a) Original rotated signal and b) extracted pulse for station 4616 for the six models and the observational dataset.

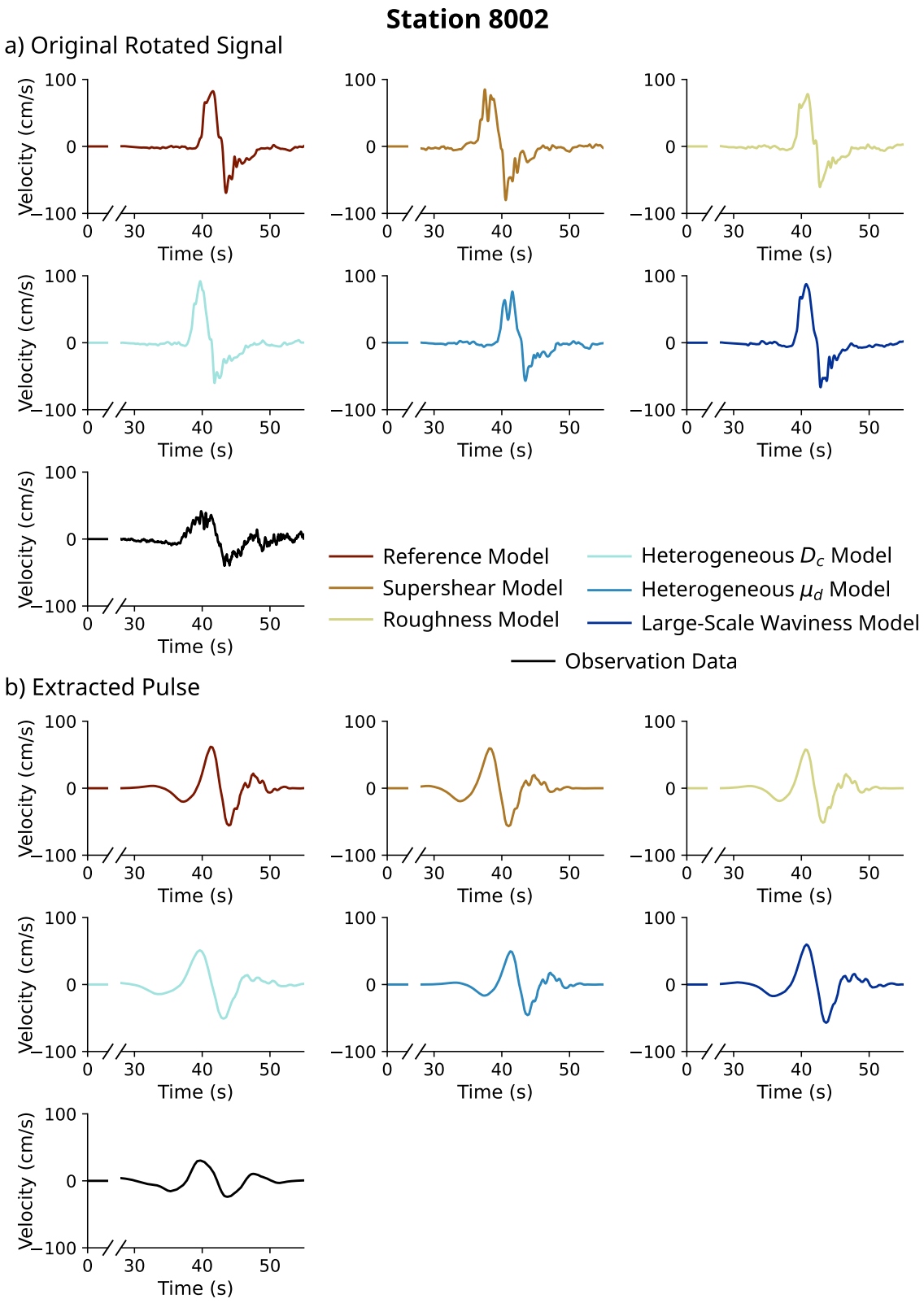


Figure S15. a) Original rotated signal and b) extracted pulse for station 8002 for the six models and the observational dataset.

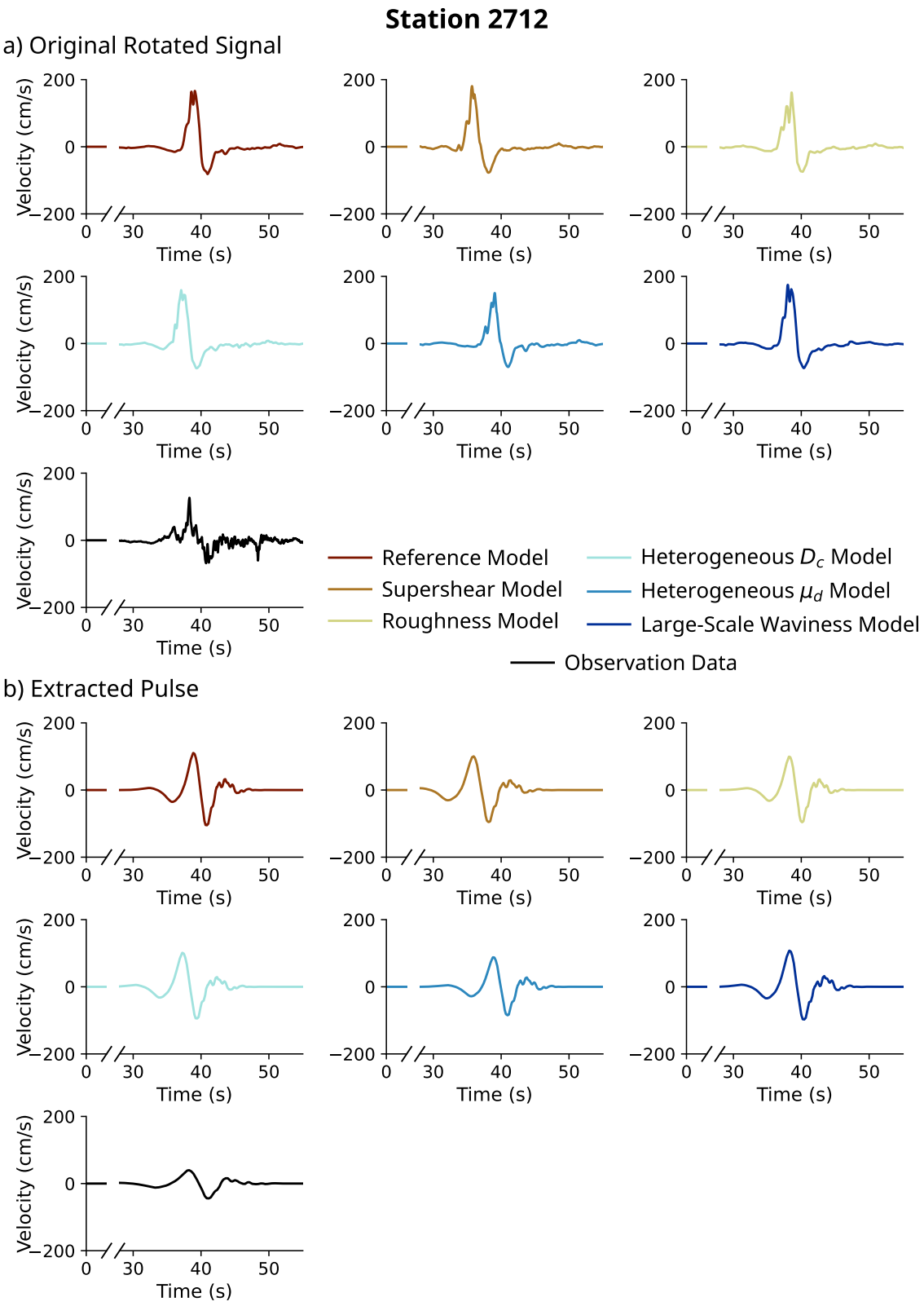


Figure S16. a) Original rotated signal and b) extracted pulse for station 2712 for the six models and the observational dataset.

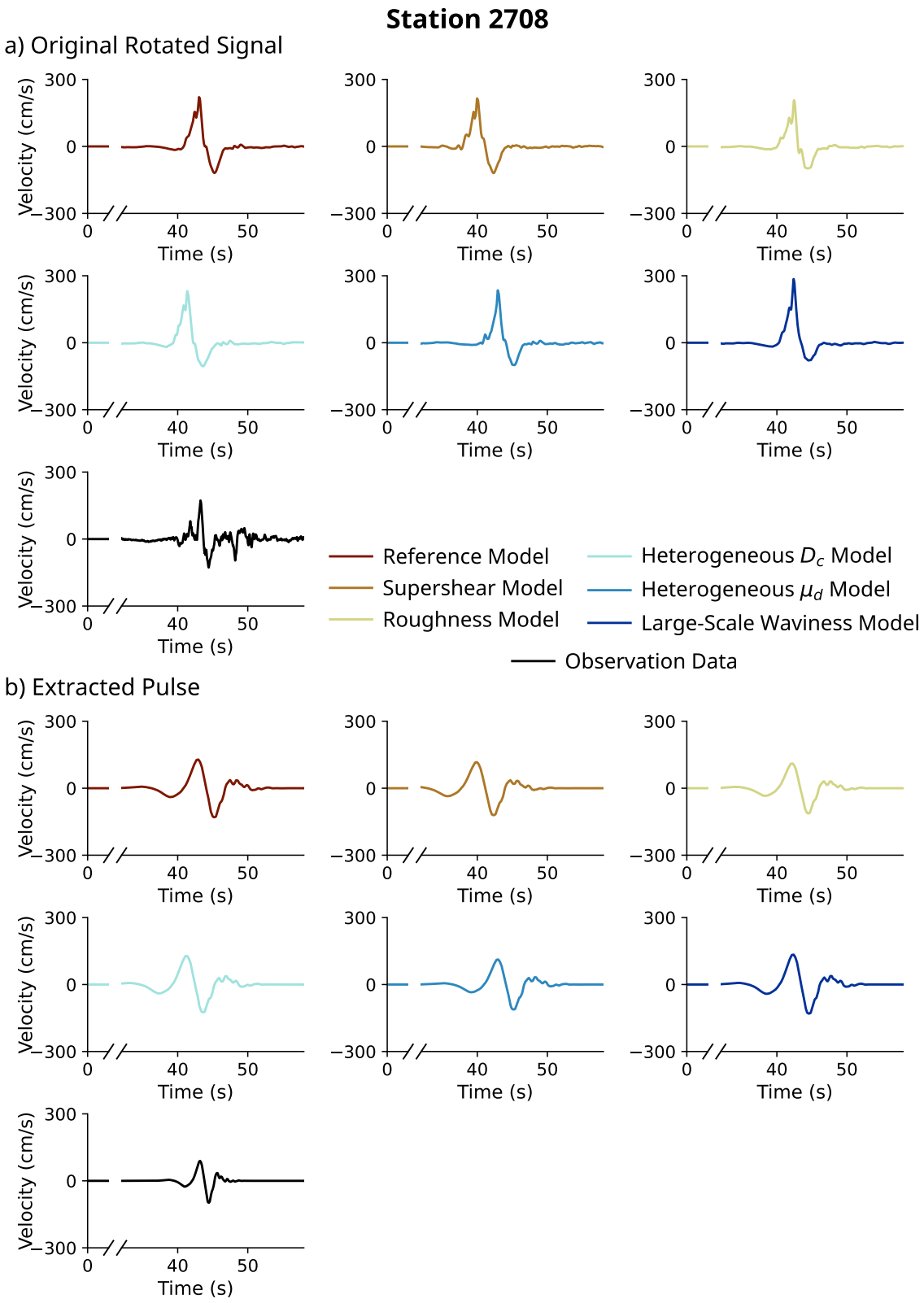


Figure S17. a) Original rotated signal and b) extracted pulse for station 2708 for the six models and the observational dataset.

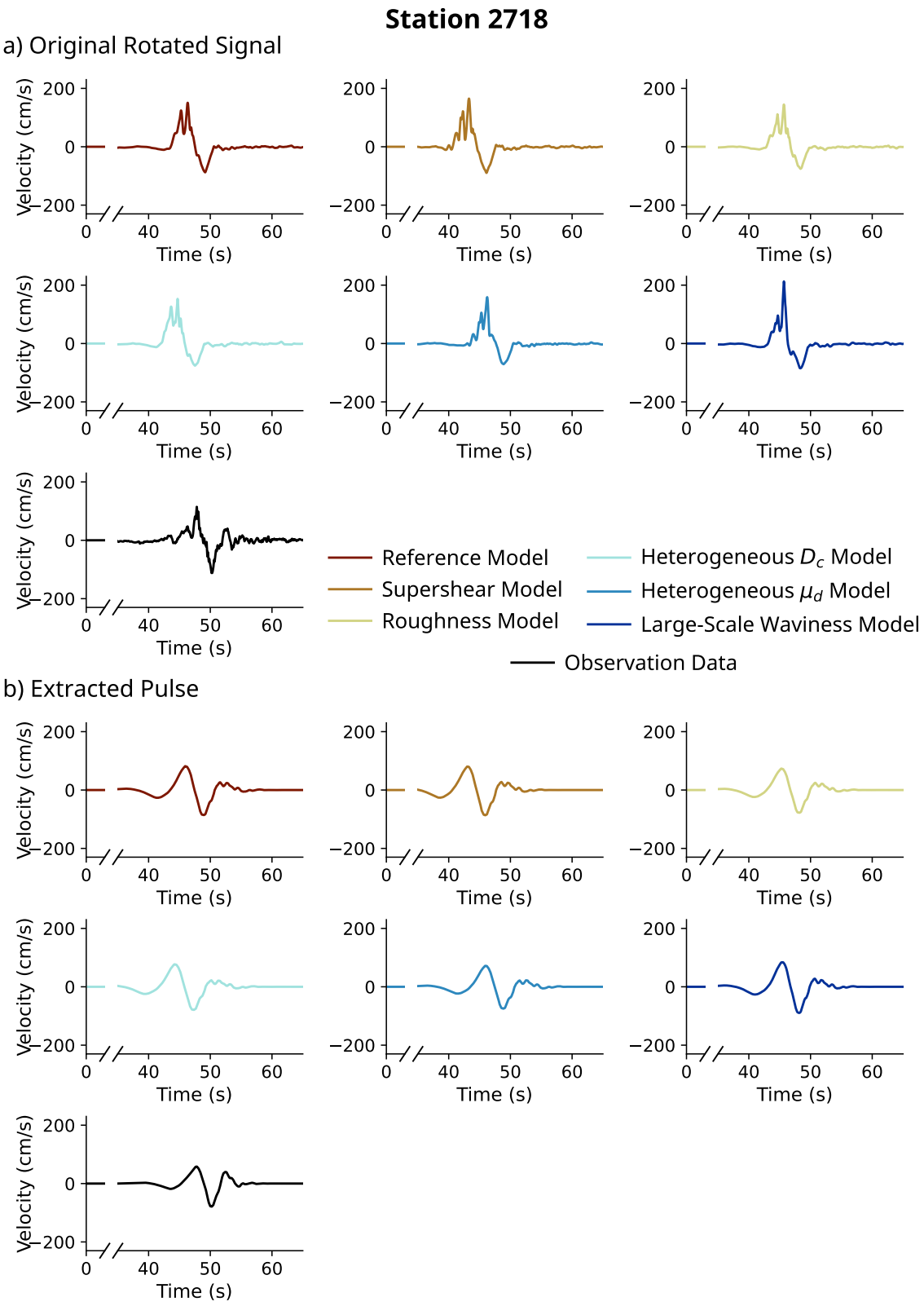


Figure S18. a) Original rotated signal and b) extracted pulse for station 2718 for the six models and the observational dataset.

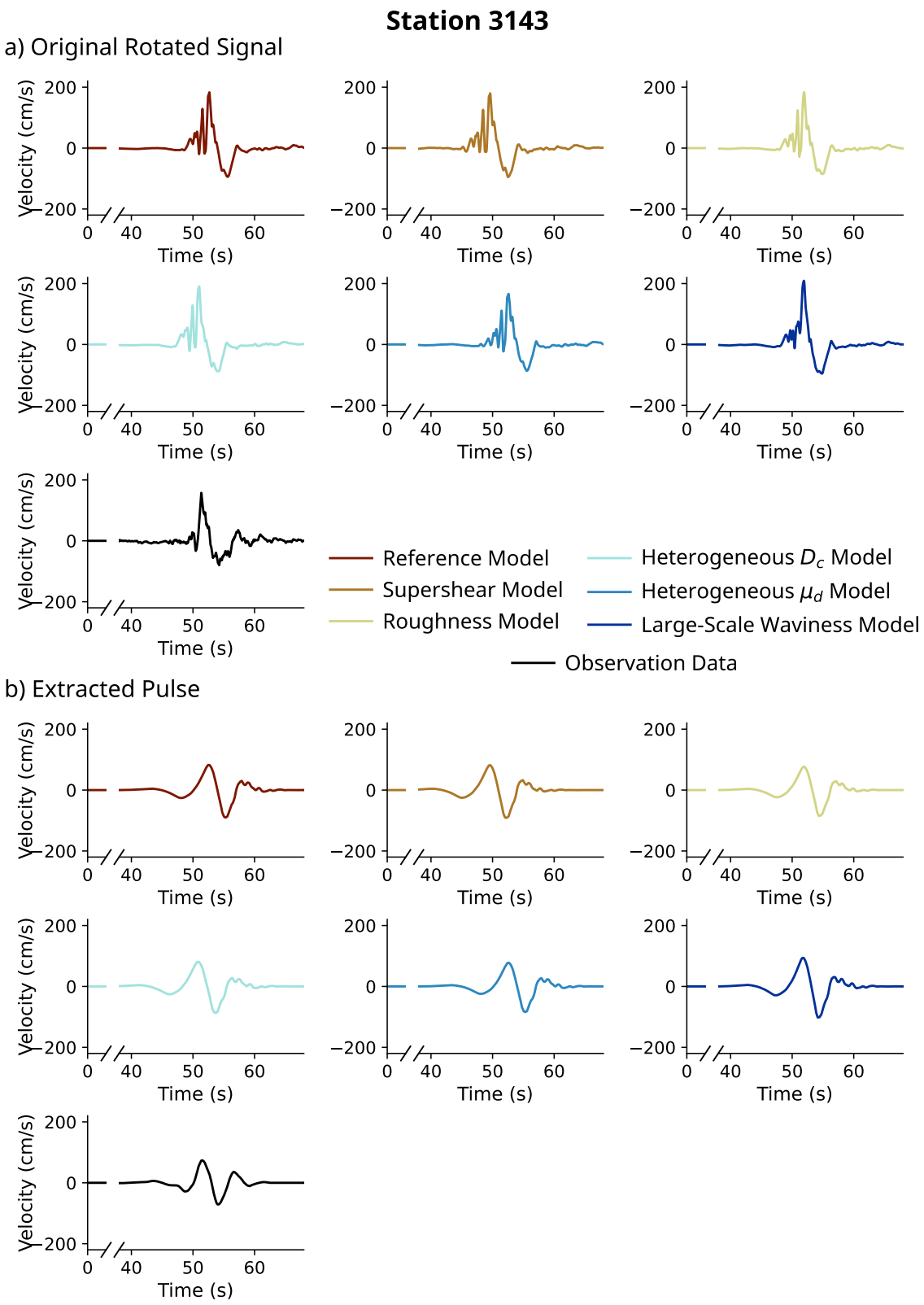


Figure S19. a) Original rotated signal and b) extracted pulse for station 3143 for the six models and the observational dataset.

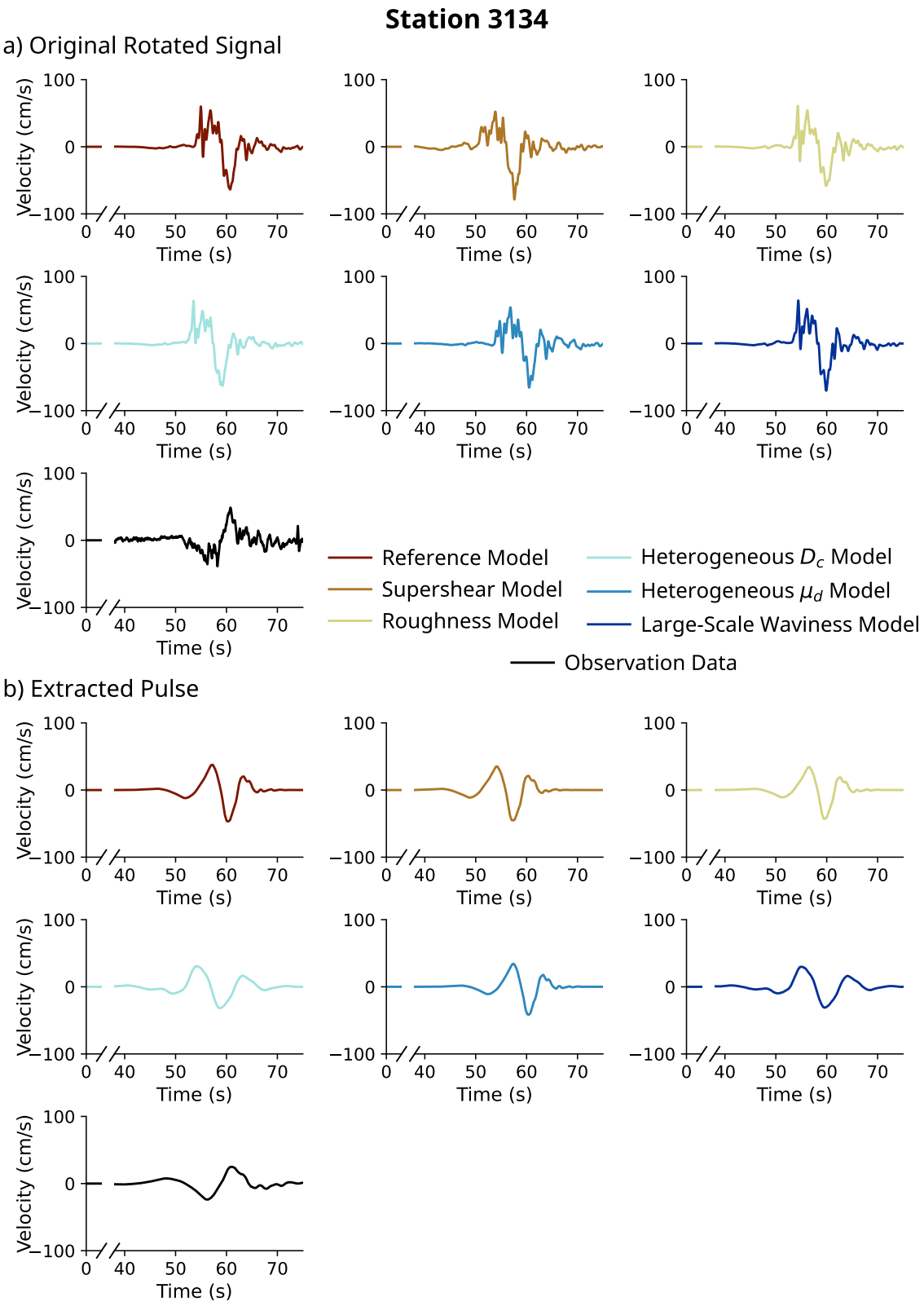


Figure S20. a) Original rotated signal and b) extracted pulse for station 3134 for the six models and the observational dataset.

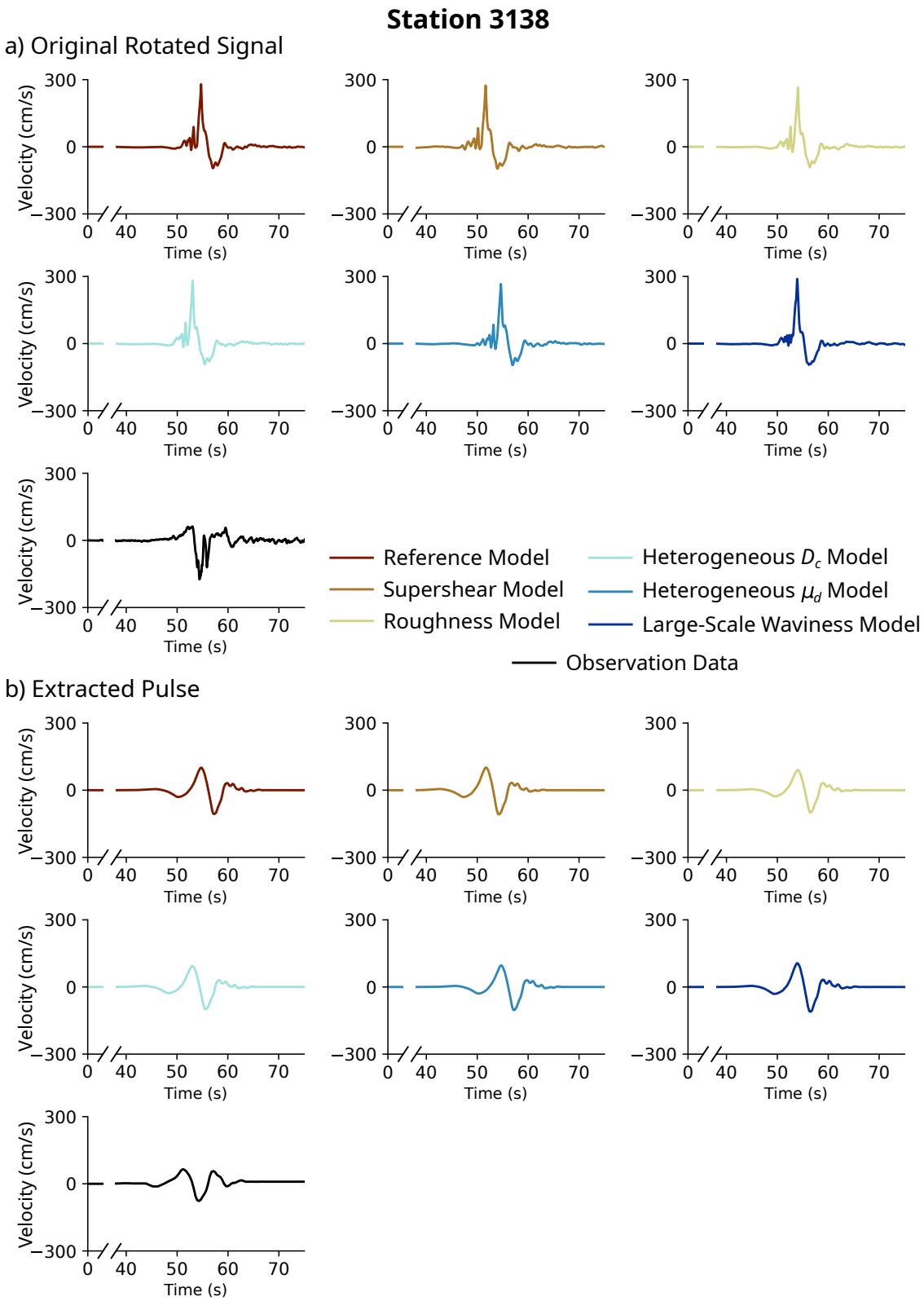


Figure S21. a) Original rotated signal and b) extracted pulse for station 3138 for the six models and the observational dataset.

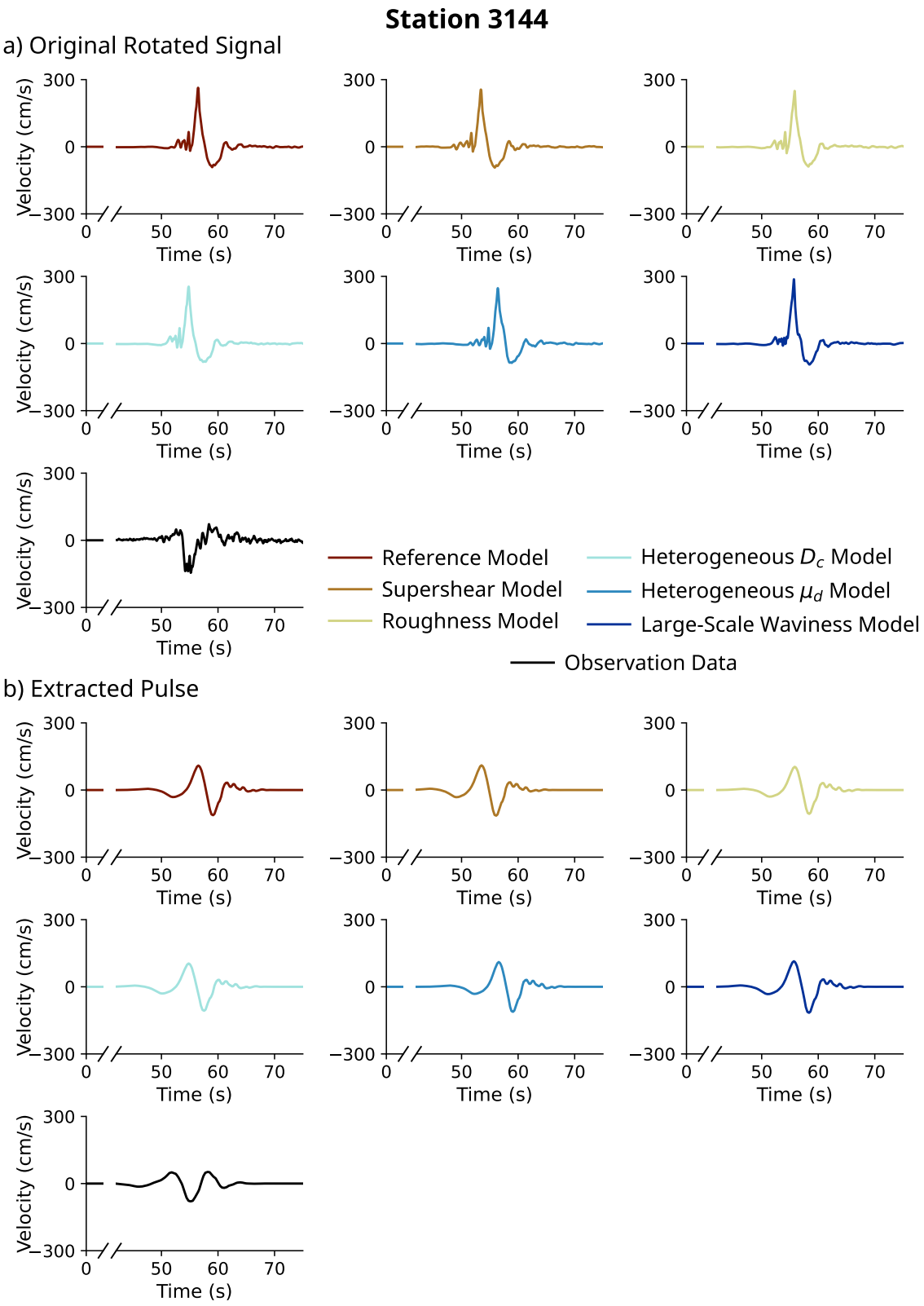


Figure S22. a) Original rotated signal and b) extracted pulse for station 3144 for the six models and the observational dataset.

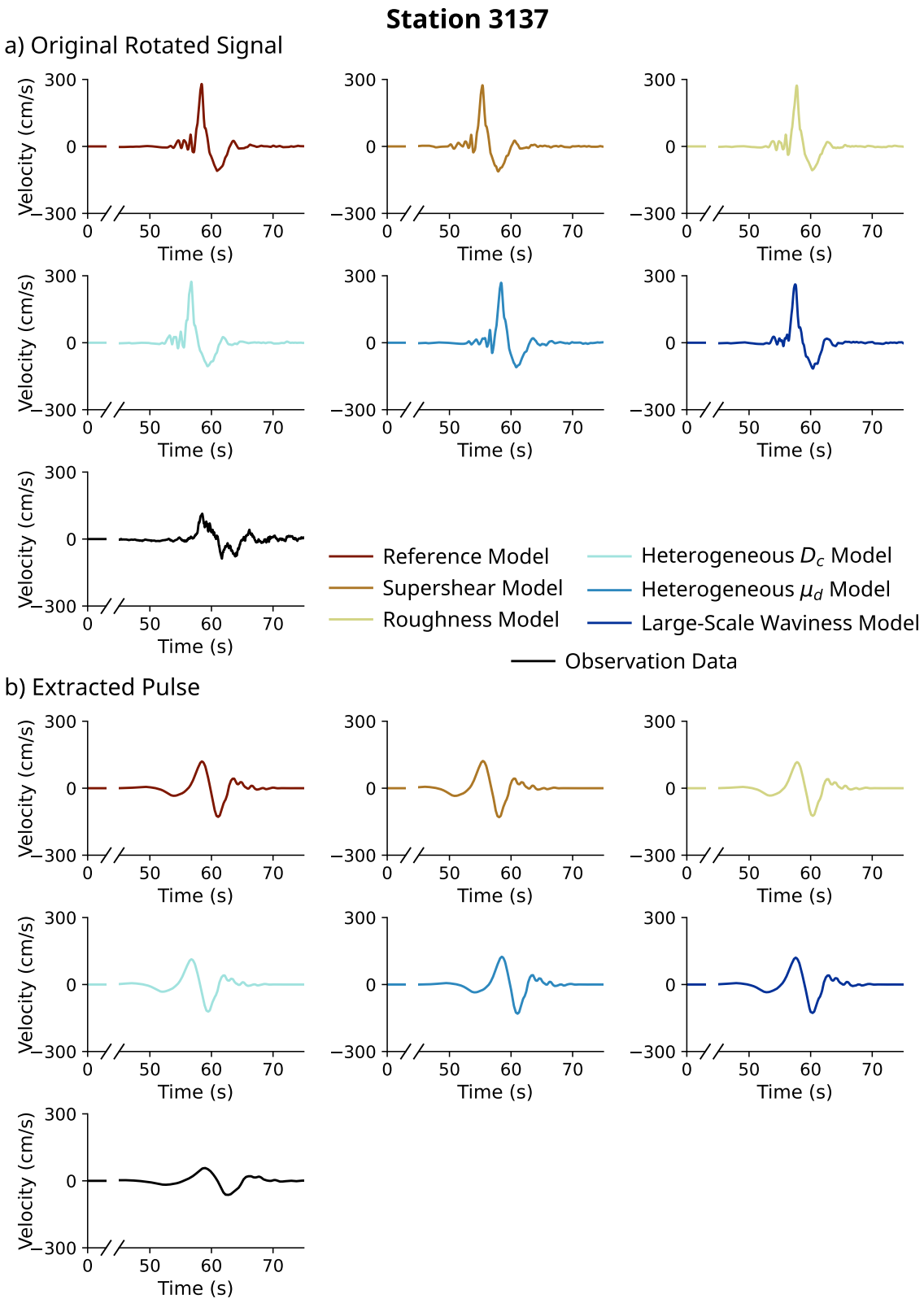


Figure S23. a) Original rotated signal and b) extracted pulse for station 3137 for the six models and the observational dataset.

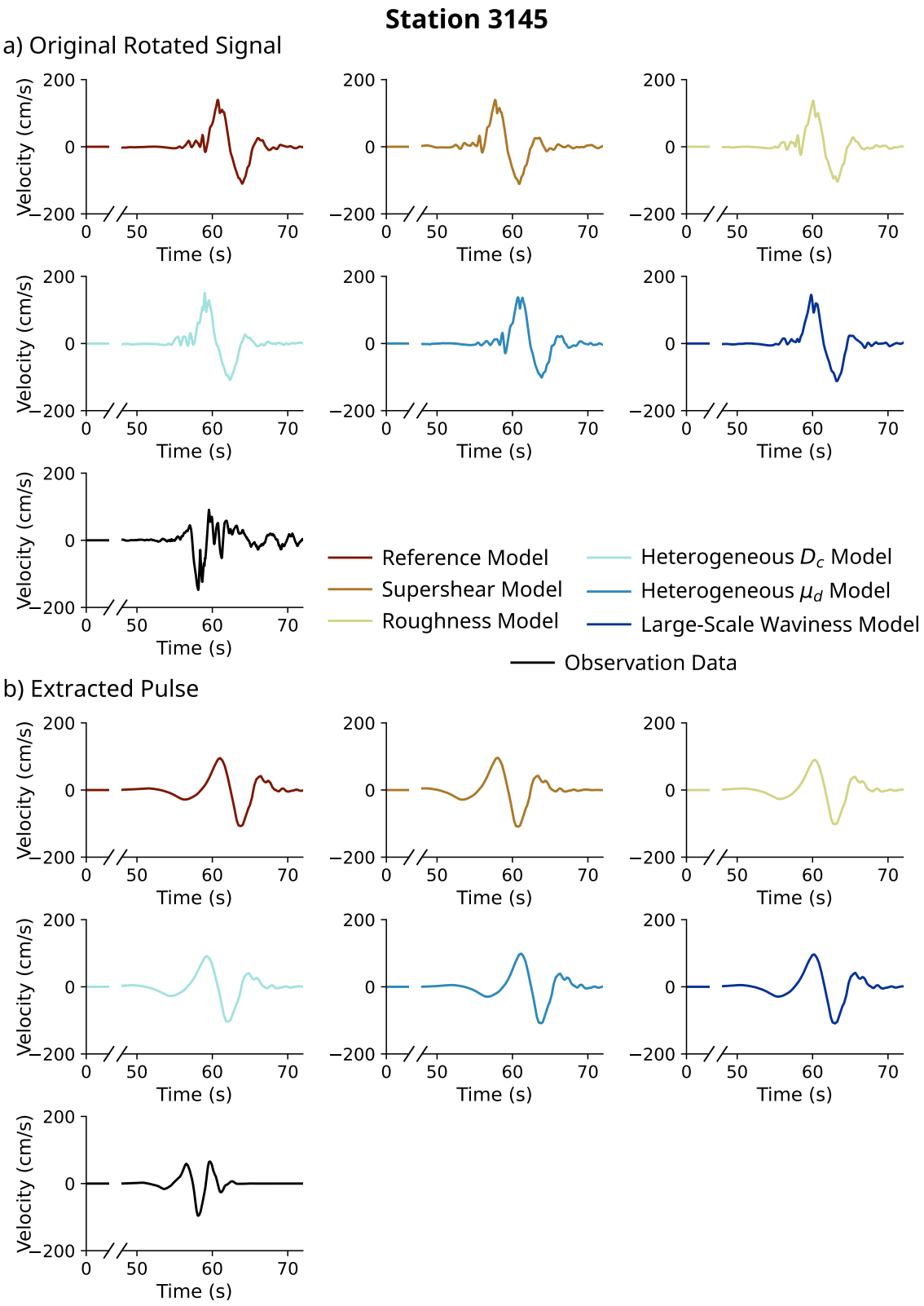


Figure S24. a) Original rotated signal and b) extracted pulse for station 3145 for the six models and the observational dataset.

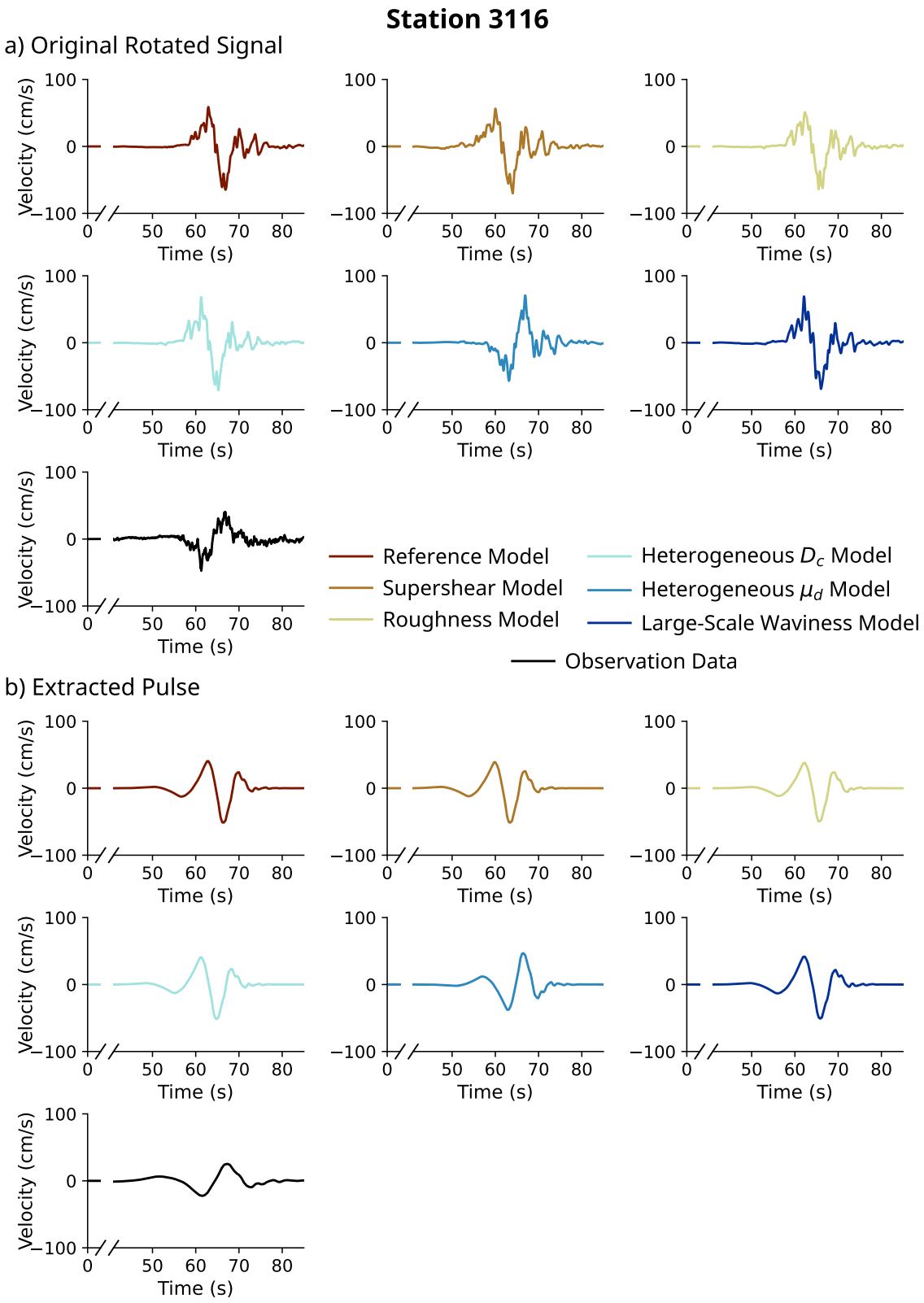


Figure S25. a) Original rotated signal and b) extracted pulse for station 3116 for the six models and the observational dataset.

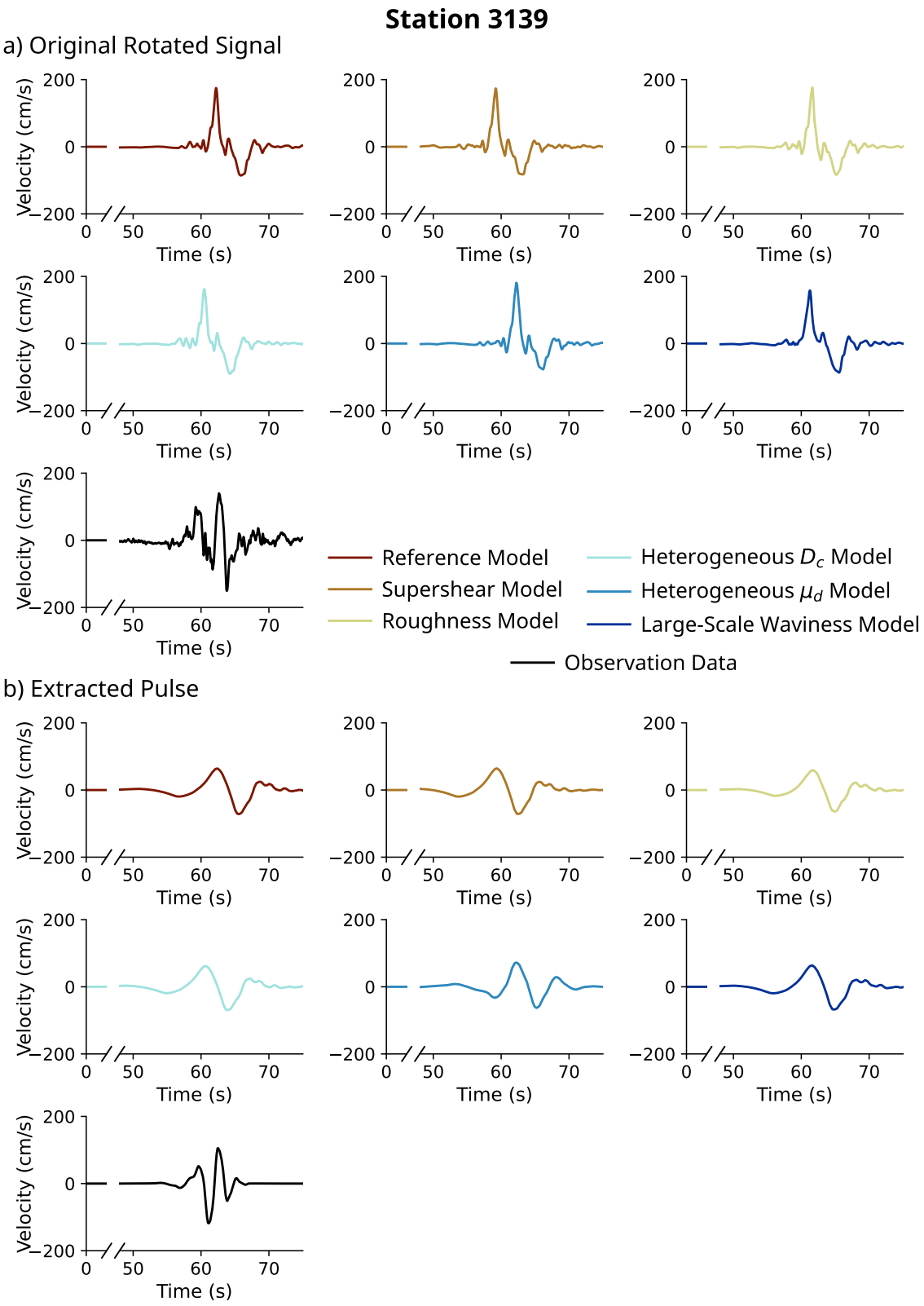


Figure S26. a) Original rotated signal and b) extracted pulse for station 3139 for the six models and the observational dataset.

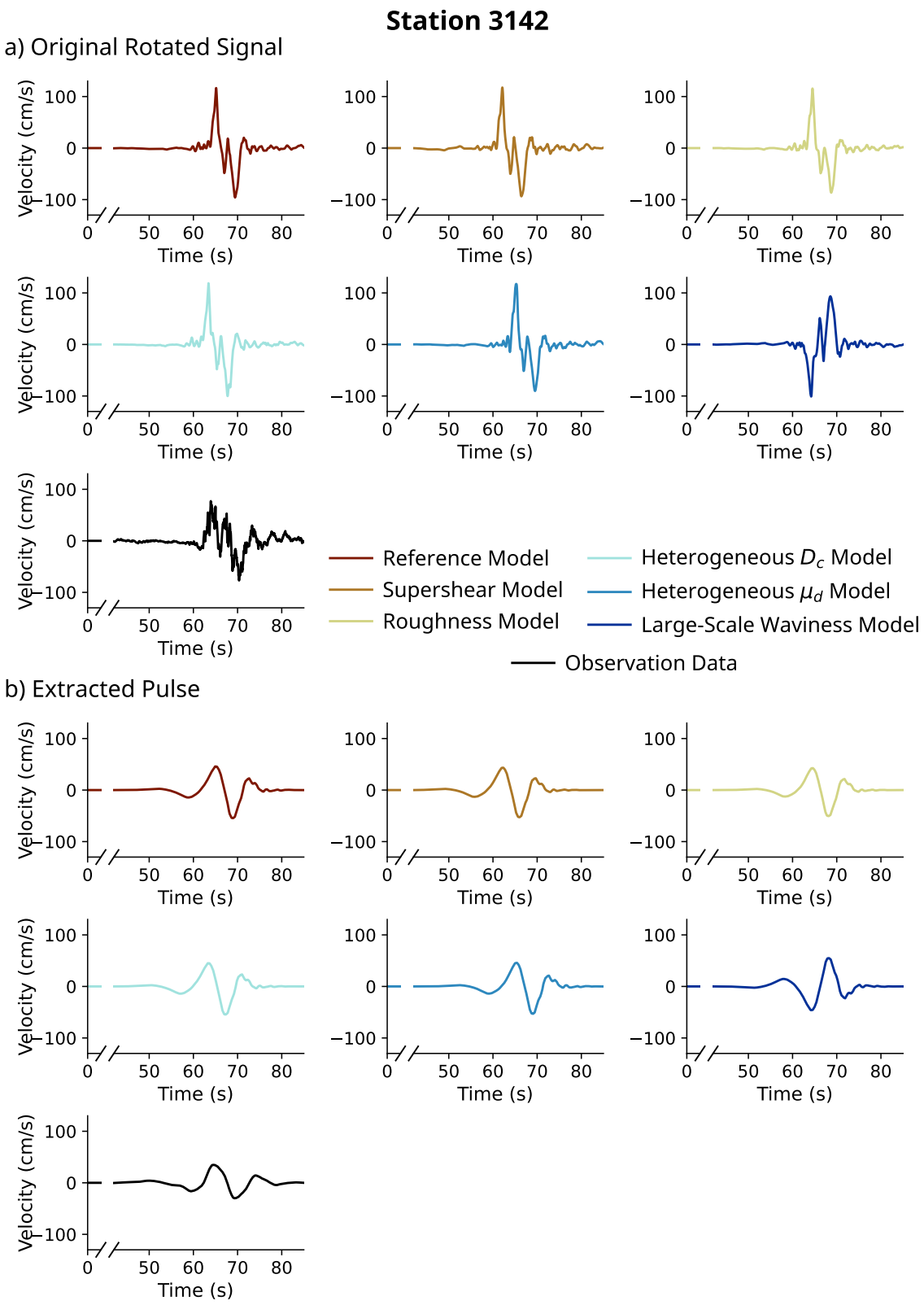


Figure S27. a) Original rotated signal and b) extracted pulse for station 3142 for the six models and the observational dataset.

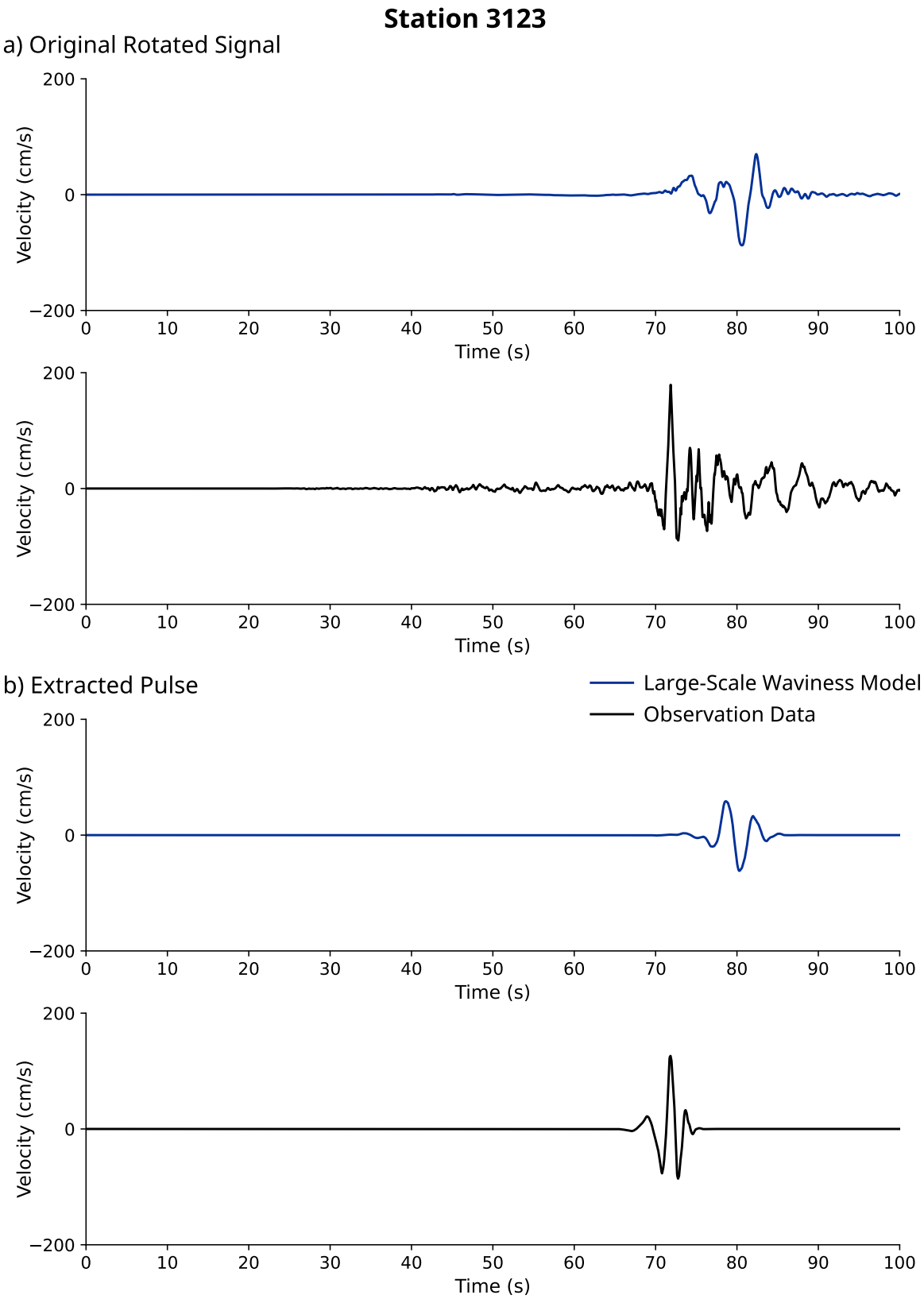


Figure S28. a) Original rotated signal and b) extracted pulse for station 3123 for the six models and the observational dataset.

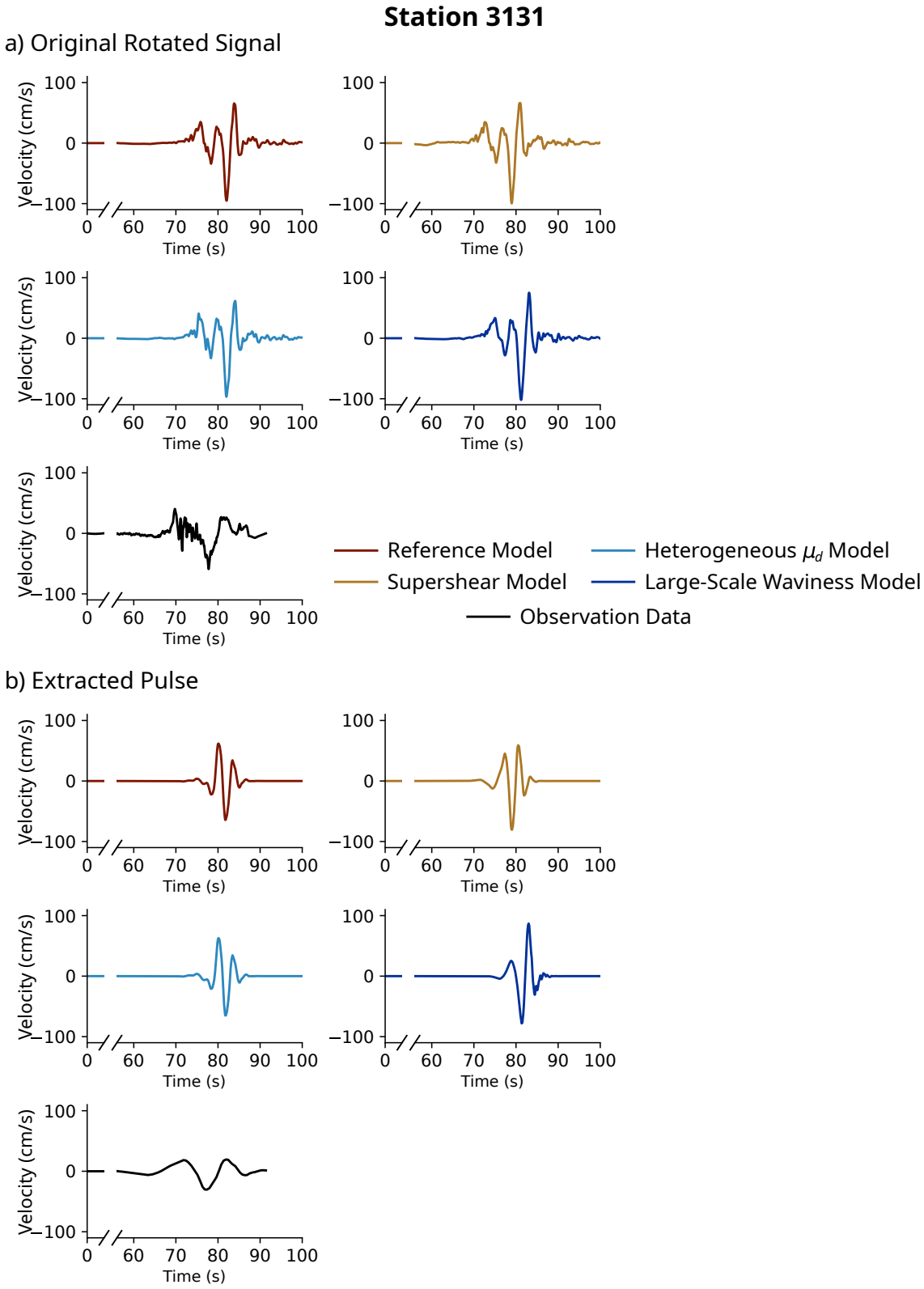


Figure S29. a) Original rotated signal and b) extracted pulse for station 3131 for the six models and the observational dataset.

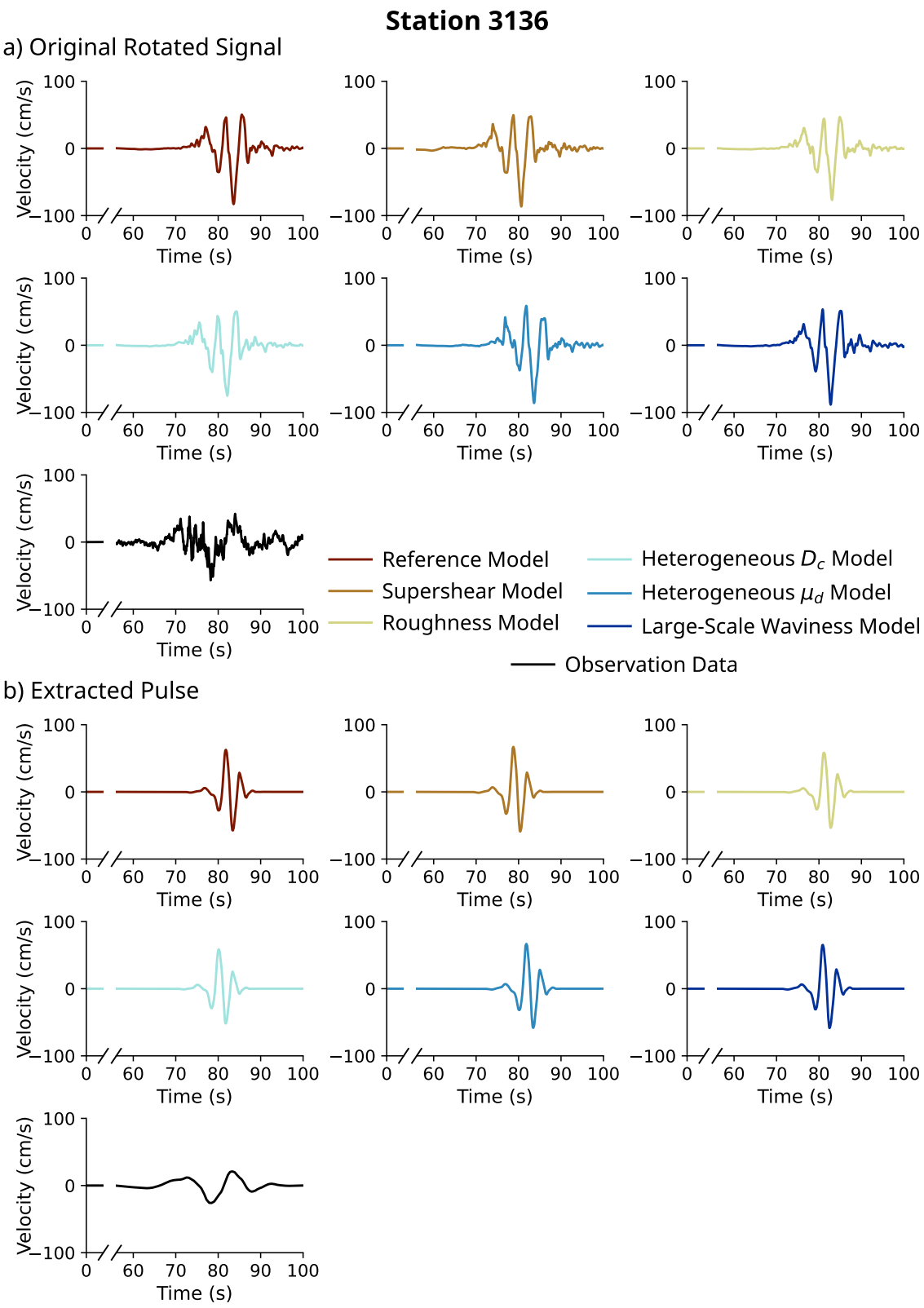


Figure S30. a) Original rotated signal and b) extracted pulse for station 3136 for the six models and the observational dataset.

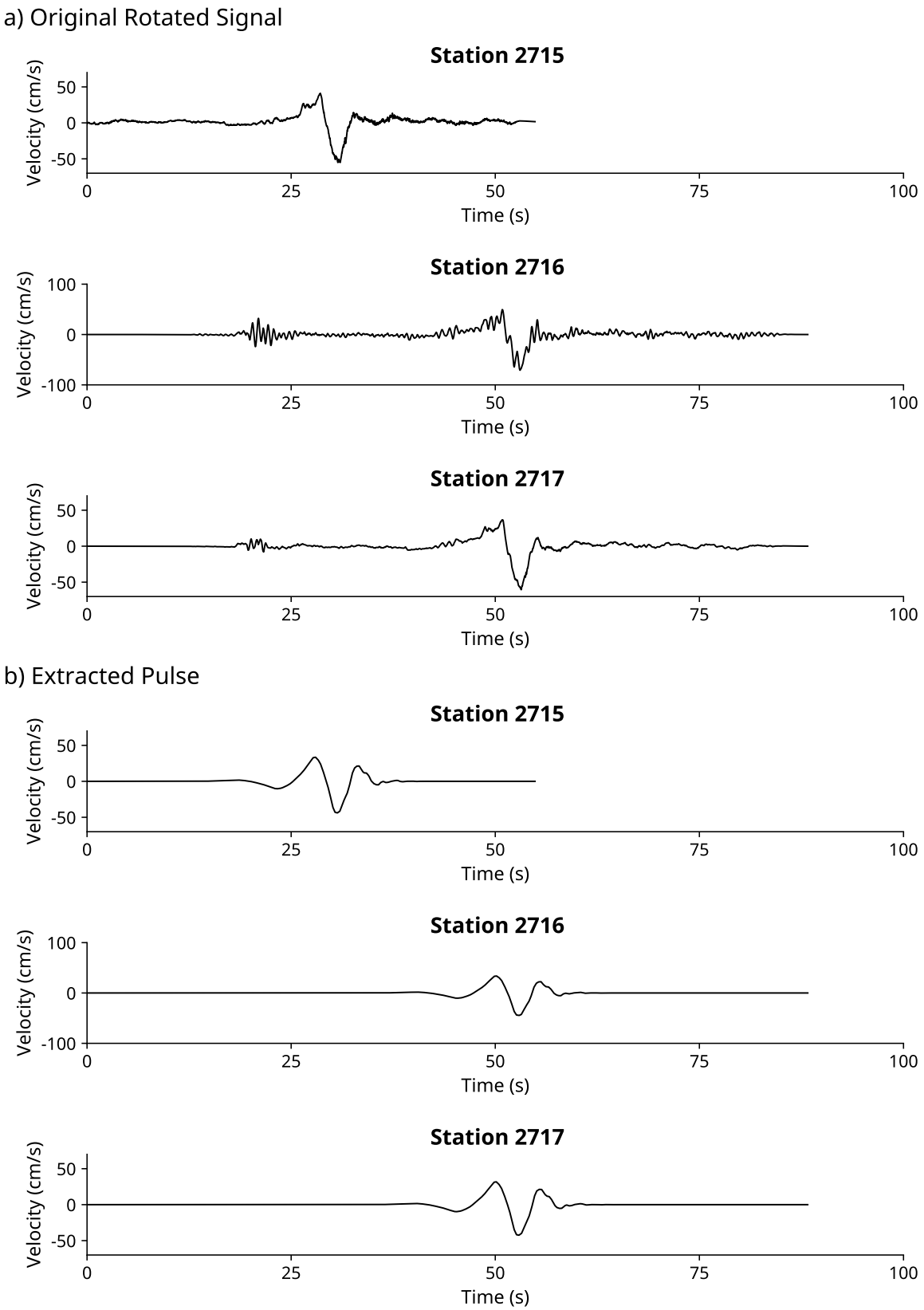


Figure S31. a) Original rotated signal and b) extracted pulse for stations 2715, 2716 and 2717 for the observational dataset.

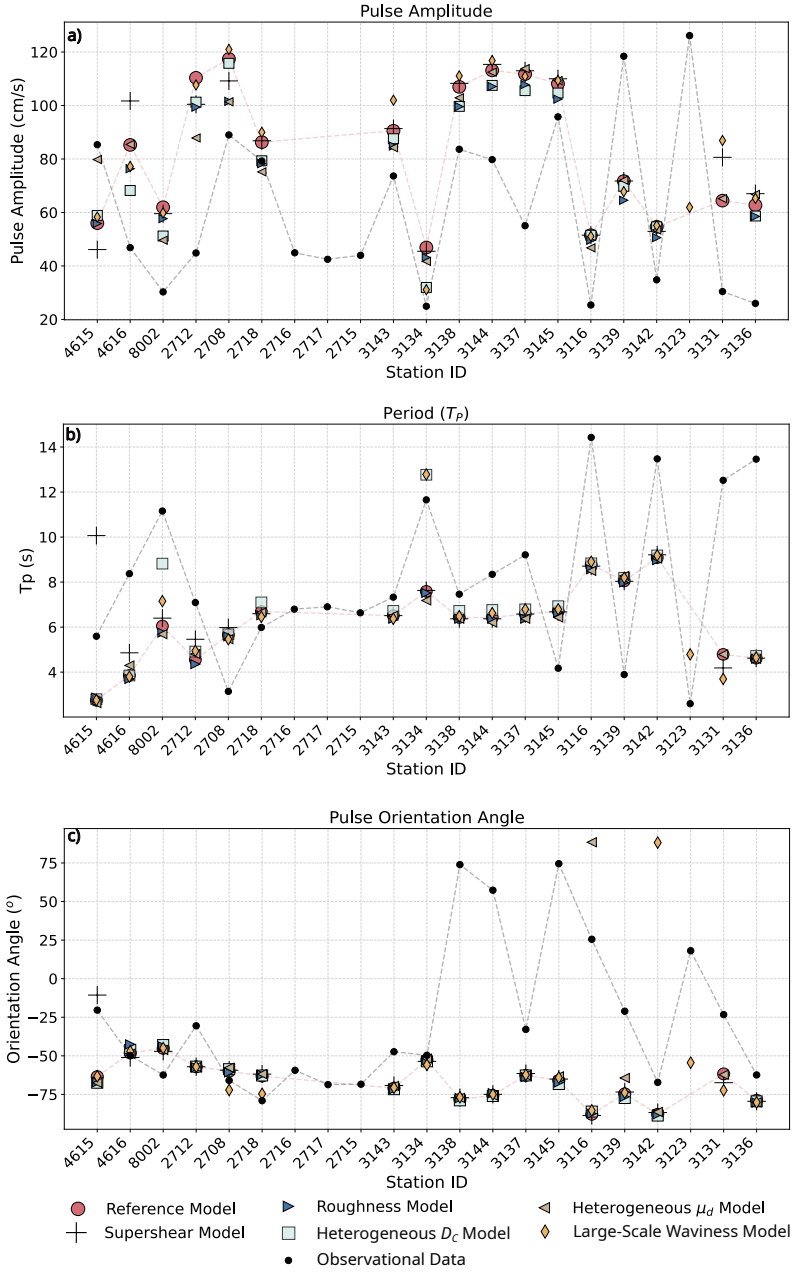


Figure S32. Comparison of a) pulse amplitude, b) pulse period (Tp), and c) pulse orientation variability for all six models and the observational data, similar to Figure 10. The pink dotted line highlights the reference model and the black dotted line highlights the observational data to better compare the variability of the models with the observational data.

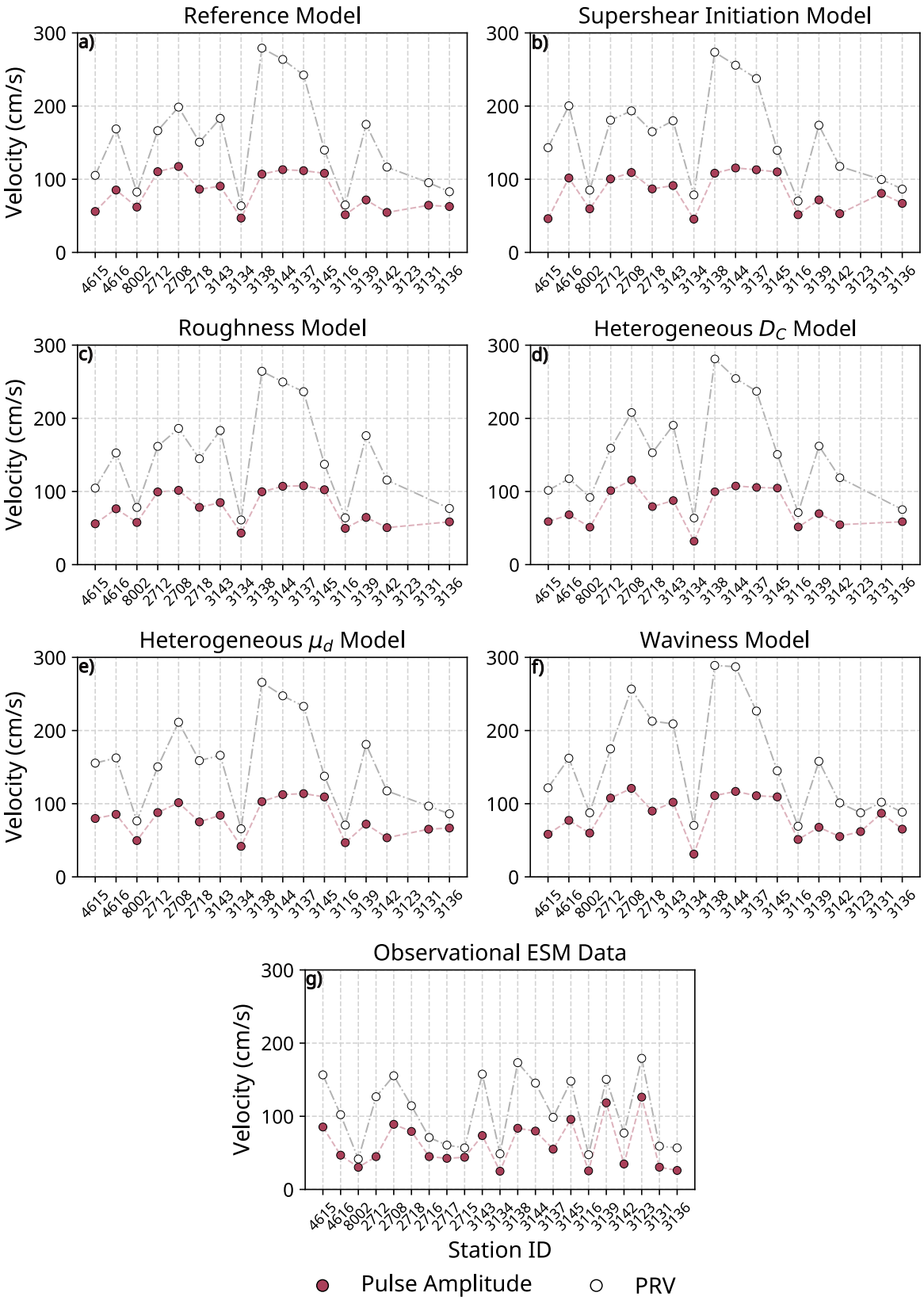


Figure S33. Comparison of the extracted Pulse Amplitude with the Peak Rotated Velocity (PVR) for the six models and the observational data at each pulse-like station.

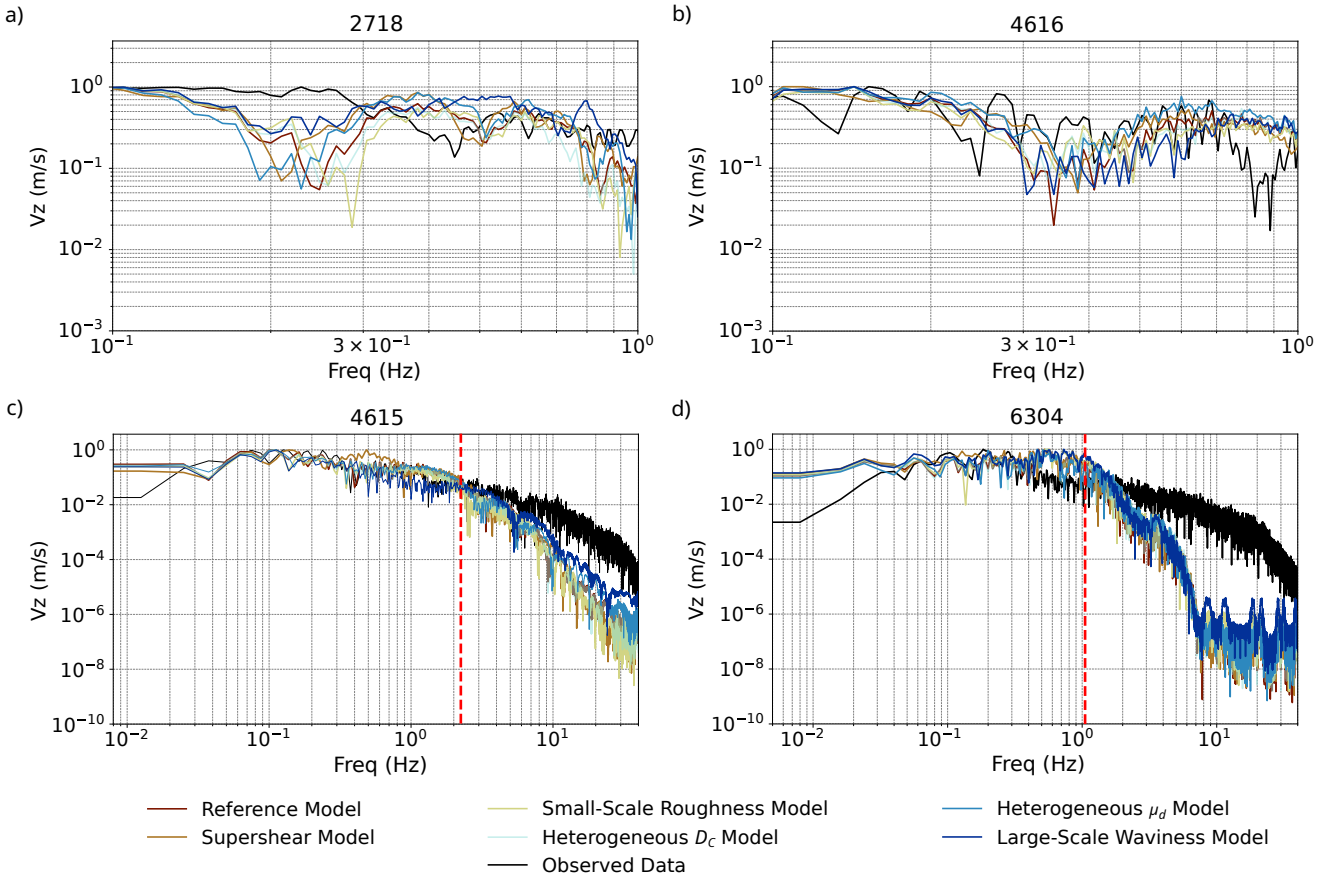


Figure S34. a) and b) show the Fourier spectra for the six synthetic models at two very near-fault stations (2718 and 4616) up to 1 Hz. c) and d) are the spectra for the six models and the observational data up to 40 Hz for stations 4615 and 6304. Station 4615 is a very near-fault station, whereas station 6304 is located ∼100 km away from the EAF. The red dotted lines depict the fall-off frequency.

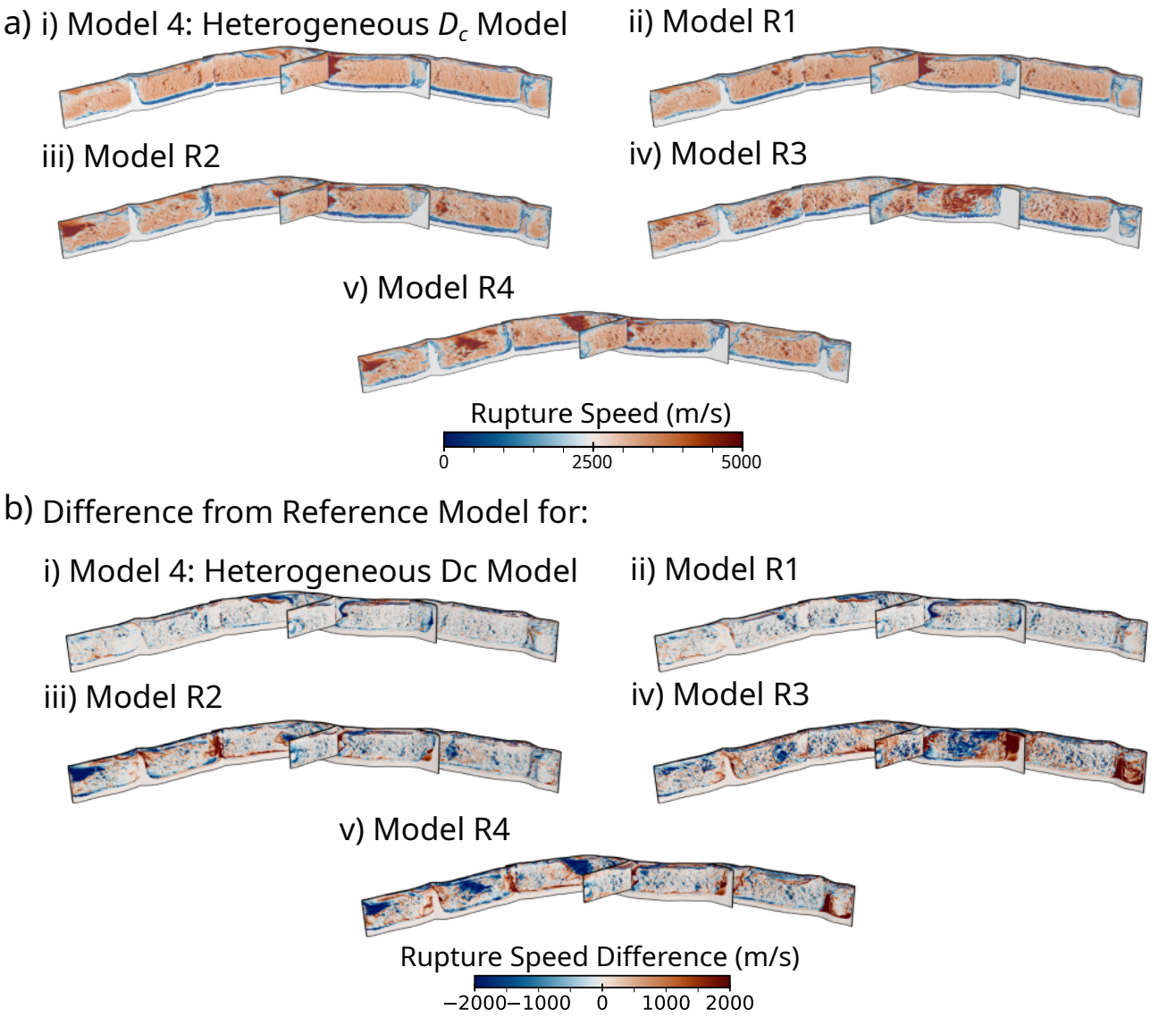


Figure S35. a) Rupture speed along the fault for the original D_c Model (Model 4) and the four new simulations involving different heterogeneous distributions of D_c (Models R1–R4, Table S12). The dark red areas highlight supershear rupture speed. b) The difference in the rupture speed between the reference model and the different D_c models (Difference = Reference Model - Complexity Model).

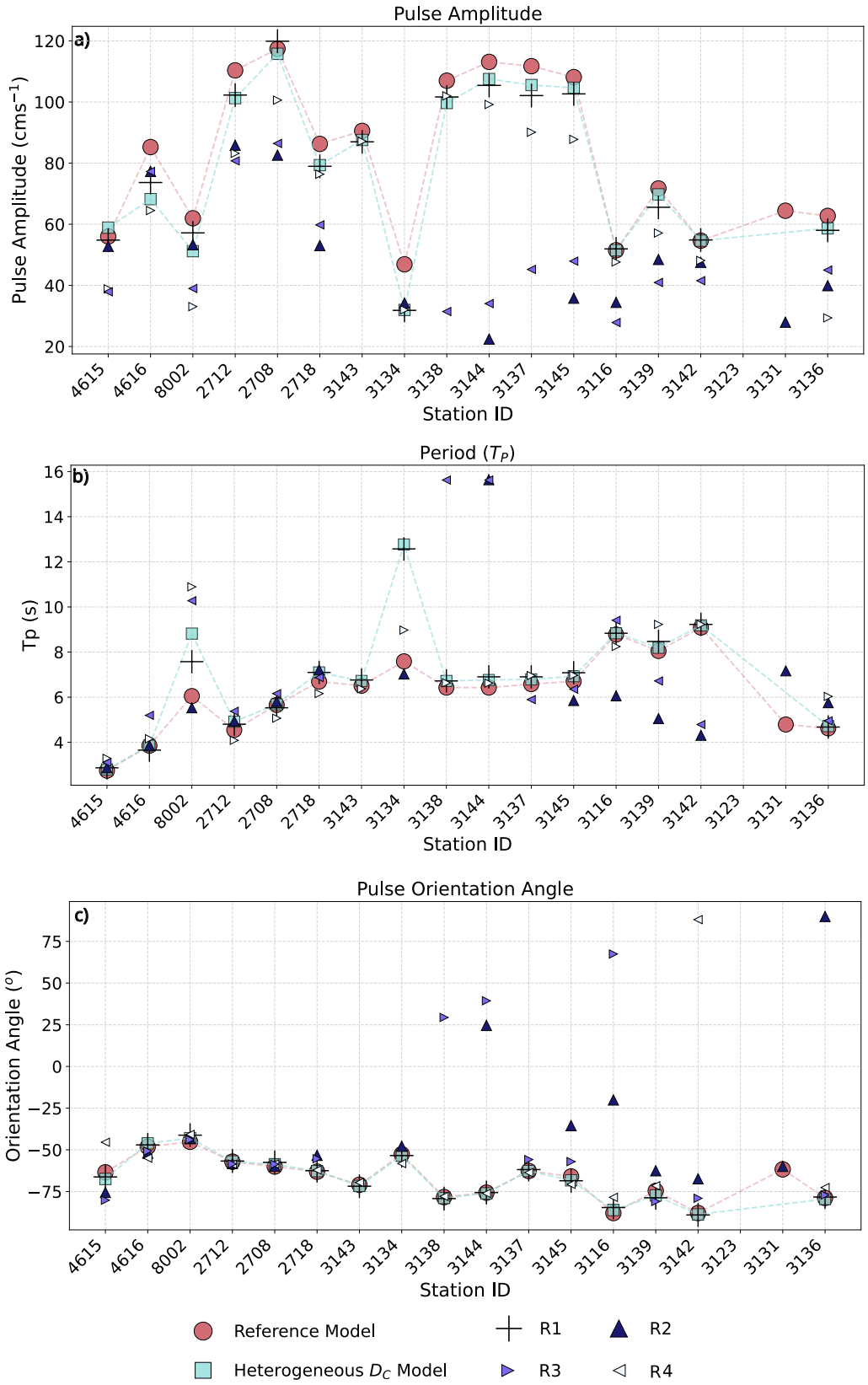


Figure S36. Comparison of the pulse properties for the extra heterogeneous D_c simulations R1–R4 with the initial Model 4 and the Reference Model. a) Pulse amplitude, b) pulse period, T_P, and c) pulse orientation.

Station	Rot. angle (°)	Amp. (cm/s)	PGV (cm/s)	T_p (s)
2708	-60.01	117.40	198.60	5.656
2712	-57.09	110.36	166.44	4.550
2718	-63.11	86.29	150.75	6.692
3116	-87.89	51.49	64.78	8.778
3131	-61.70	64.43	95.28	4.788
3134	-52.64	46.89	63.68	7.588
3136	-78.80	62.73	83.00	4.620
3137	-62.68	111.74	242.45	6.580
3138	-78.31	106.97	279.20	6.426
3139	-74.61	71.72	174.95	8.050
3142	-87.89	54.64	116.56	9.086
3143	-70.94	90.55	183.17	6.510
3144	-75.66	113.13	263.75	6.426
3145	-65.97	108.15	139.91	6.706
4615	-63.48	56.01	105.28	2.744
4616	-48.15	85.27	168.77	3.850
8002	-45.17	61.95	82.52	6.048

Table S3. Pulse properties for stations classified as pulse-like in the Reference Model. Rot. Angle is the corresponding angle by which the original signal was rotated, Amp. refers to the amplitude of the extracted pulse, PGV refers to the peak ground velocity of the original rotated signal, and T_p refers to the period.

Station	Rot. angle (°)	Amp. (cm/s)	PGV (cm/s)	T_p (s)
2708	-59.32	109.20	193.46	5.978
2712	-57.06	100.45	180.74	5.460
2718	-61.83	86.82	165.04	6.594
3116	-88.66	51.51	70.11	8.708
3131	-67.43	80.62	99.60	4.186
3134	-53.62	45.49	78.59	7.630
3136	-79.48	67.03	86.52	4.620
3137	-61.46	112.99	237.61	6.580
3138	-77.08	108.29	273.60	6.370
3139	-73.44	71.77	173.83	8.036
3142	-86.73	52.93	117.53	9.212
3143	-69.21	91.36	179.95	6.510
3144	-74.97	115.38	255.83	6.370
3145	-65.07	110.00	139.57	6.678
4615	-10.63	46.12	143.16	10.066
4616	-51.07	101.70	200.34	4.858
8002	-47.10	59.56	85.13	6.398

Table S4. Pulse properties for stations classified as pulse-like in the Supershear Initiation Model. Rot. Angle is the corresponding angle by which the original signal was rotated, Amp. refers to the amplitude of the extracted pulse, PGV refers to the peak ground velocity of the original rotated signal, and T_p refers to the period.

Station	Rot. angle (°)	Amp. (cm/s)	PGV (cm/s)	T_p (s)
2708	-60.74	101.55	186.22	5.586
2712	-57.43	99.37	161.65	4.354
2718	-62.34	78.27	144.74	6.524
3116	-87.48	49.61	63.95	8.568
3134	-52.94	43.12	61.04	7.518
3136	-80.28	58.53	76.78	4.592
3137	-63.76	107.80	236.40	6.370
3138	-77.41	99.59	264.29	6.370
3139	-76.55	64.56	176.29	7.980
3142	-87.93	50.59	115.59	8.974
3143	-71.61	84.84	183.40	6.370
3144	-74.22	107.11	249.66	6.370
3145	-67.31	102.36	137.19	6.650
4615	-67.17	55.87	104.62	2.870
4616	-42.57	76.36	152.66	3.696
8002	-43.98	57.68	78.17	5.754

Table S5. Pulse properties for stations classified as pulse-like in the Roughness Model. Rot. Angle is the corresponding angle by which the original signal was rotated, Amp. refers to the amplitude of the extracted pulse, PGV refers to the peak ground velocity of the original rotated signal, and T_p refers to the period.

Station	Rot. angle (°)	Amp. (cm/s)	PGV (cm/s)	T_p (s)
2708	-58.64	115.77	208.00	5.684
2712	-56.97	101.27	159.17	4.914
2718	-62.75	79.34	153.03	7.098
3116	-86.07	51.49	71.13	8.834
3134	-53.55	31.97	63.68	12.768
3136	-79.51	58.66	75.27	4.718
3137	-62.70	105.56	236.97	6.790
3138	-78.88	99.68	281.19	6.720
3139	-77.38	69.77	162.19	8.190
3142	-88.72	54.64	118.79	9.184
3143	-71.64	87.58	190.60	6.720
3144	-76.07	107.53	254.49	6.762
3145	-68.27	104.66	150.67	6.930
4615	-67.46	58.90	101.54	2.800
4616	-46.12	68.22	117.56	3.850
8002	-42.99	51.19	91.89	8.820

Table S6. Pulse properties for stations classified as pulse-like in the Heterogeneous D_c Model. Rot. Angle is the corresponding angle by which the original signal was rotated, Amp. refers to the amplitude of the extracted pulse, PGV refers to the peak ground velocity of the original rotated signal, and T_p refers to the period.

Station	Rot. angle (°)	Amp. (cm/s)	PGV (cm/s)	T_p (s)
2708	-57.73	101.39	211.31	5.460
2712	-57.23	87.87	150.47	4.802
2718	-61.82	75.17	158.88	6.650
3116	88.44	46.77	70.67	8.498
3131	-62.28	65.16	96.70	4.788
3134	-51.76	41.73	65.69	7.182
3136	-80.19	66.76	86.15	4.592
3137	-62.63	113.80	233.09	6.370
3138	-77.25	102.88	265.87	6.370
3139	-64.36	72.06	181.01	8.274
3142	-86.41	53.45	117.44	9.044
3143	-69.49	84.24	166.12	6.510
3144	-75.68	112.47	247.47	6.202
3145	-63.30	109.30	137.60	6.426
4615	-67.48	79.78	155.48	2.618
4616	-48.61	85.44	162.63	4.298
8002	-46.13	49.62	76.44	5.684

Table S7. Pulse properties for stations classified as pulse-like in the Heterogeneous μ_d Model. Rot. Angle is the corresponding angle by which the original signal was rotated, Amp. refers to the amplitude of the extracted pulse, PGV refers to the peak ground velocity of the original rotated signal, and T_p refers to the period.

Station	Rot. angle (°)	Amp. (cm/s)	PGV (cm/s)	T_p (s)
2708	-72.14	120.97	256.74	5.460
2712	-57.07	107.68	174.92	4.942
2718	-74.60	90.00	212.79	6.454
3116	-85.40	51.06	69.17	8.904
3123	-54.43	61.93	87.59	4.788
3131	-72.33	86.90	102.02	3.696
3134	-55.85	31.12	70.29	12.782
3136	-80.16	65.26	88.52	4.648
3137	-62.34	110.92	226.67	6.790
3138	-76.82	111.07	289.00	6.482
3139	-73.86	67.77	158.04	8.190
3142	88.18	55.11	101.06	9.184
3143	-70.63	102.00	209.15	6.370
3144	-75.01	116.79	287.21	6.622
3145	-64.15	109.35	144.98	6.790
4615	-63.27	58.29	121.70	2.758
4616	-47.10	77.20	162.20	3.794
8002	-45.04	59.81	87.53	7.154

Table S8. Pulse properties for stations classified as pulse-like in the Waviness Model. Rot. Angle is the corresponding angle by which the original signal was rotated, Amp. refers to the amplitude of the extracted pulse, PGV refers to the peak ground velocity of the original rotated signal, and T_p refers to the period.

Station	Rot. angle (°)	Amp. (cm/s)	PGV (cm/s)	T_p (s)
2708	-65.93	88.99	155.39	3.143
2712	-30.54	44.85	126.59	7.091
2715	-68.37	43.97	55.14	6.636
2716	-59.40	44.92	70.98	6.797
2717	-68.66	42.49	60.55	6.902
2718	-79.06	79.24	114.62	5.985
3116	25.54	25.39	47.36	14.427
3123	18.12	126.14	179.16	2.597
3131	-23.29	30.42	59.05	12.523
3134	-49.65	24.92	48.74	11.655
3136	-62.38	25.98	56.87	13.461
3137	-32.89	55.04	98.52	9.212
3138	73.90	83.64	173.22	7.462
3139	-21.09	118.43	150.48	3.892
3142	-67.23	34.80	77.04	13.475
3143	-47.34	73.64	157.59	7.329
3144	57.34	79.76	145.38	8.344
3145	74.51	95.75	147.92	4.172
4615	-20.36	85.60	161.74	5.593
4616	-49.77	46.85	102.33	8.372
8002	-62.41	30.28	41.71	11.158

Table S9. Pulse properties for stations classified as pulse-like from the ESM observational data. Rot. Angle is the corresponding angle by which the original signal was rotated, Amp. refers to the amplitude of the extracted pulse, PGV refers to the peak ground velocity of the original rotated signal, and T_p refers to the period.

Dataset	Candidate	T_p (s)	PGV (cm/s)	Rot. Angle (°)	PI	Is-Pulse	Chosen
Reference Model	1	8.778	64.78	-87.89	13.54	1	YES
	2	11.676	65.40	-84.29	10.29	1	No
	3	5.964	63.59	87.13	2.33	0	No
	4	9.716	64.29	89.84	-0.89	0	No
	5	15.638	61.83	81.47	4.59	1	No
Supershear Initiation Model	1	8.708	70.11	-88.65	15.30	1	YES
	2	5.964	69.89	89.63	2.77	0	No
	3	12.194	70.20	-87.68	8.55	1	No
	4	4.424	69.28	86.22	-13.27	0	No
	5	13.132	70.17	-79.41	-8.77	0	No
Roughness Model	1	8.568	63.95	-87.50	12.50	1	YES
	2	11.312	63.57	-84.16	8.50	1	No
	3	5.908	64.09	89.74	3.45	0	No
	4	9.548	64.09	87.18	2.31	1	No
	5	15.638	63.71	82.05	3.73	1	No
Heterogeneous D_c Model	1	8.834	71.13	-86.08	16.06	1	YES
	2	12.292	71.82	-83.17	9.21	1	No
	3	6.076	69.45	88.76	0.67	0	No
	4	9.716	70.18	-89.21	-2.21	0	No
	5	15.638	71.93	-82.64	0.77	1	No
Heterogeneous μ_d Model	1	8.498	70.67	88.41	15.21	1	YES
	2	11.662	71.12	-86.84	9.12	1	No
	3	5.782	69.73	83.58	3.83	0	No
	4	9.548	69.67	83.37	-0.14	0	No
	5	15.638	65.82	72.60	3.86	1	No
Waviness Model	1	8.904	69.17	-85.39	14.88	1	YES
	2	11.676	70.13	-81.79	10.59	1	No
	3	5.922	67.61	-89.86	-1.09	0	No
	4	9.576	68.10	-88.56	-4.05	0	No
	5	15.638	62.82	79.61	3.83	1	No
ESM Data	1	14.427	47.36	25.54	6.42	1	YES
	2	15.295	49.23	32.96	5.31	1	No
	3	12.649	42.11	11.51	-5.91	0	No
	4	15.295	50.44	42.65	3.87	1	No
	5	15.288	50.45	49.04	-10.52	0	No

Table S10. Properties of the five candidate pulses for station 3116 for the six dynamic rupture models shown in the main text and the ESM data. T_p is the period, PGV is the peak ground velocity of the original rotated signal, and Rot. Angle is the corresponding angle by which the signal is rotated. PI is the pulse indicator, and Is-Pulse shows a candidate classified as a pulse when = 1 and not a pulse when = 0. 'Chosen' depicts which candidate is the chosen pulse. The details of the coefficients for each candidate can be seen in the Supplementary Excel File S1 included in the Zenodo repository.

Dataset	Candidate	T_p (s)	PGV (cm/s)	Rot. Angle (°)	PI	Is-Pulse	Chosen
Reference Model	1	9.086	116.56	-87.89	10.65	1	YES
	2	10.234	122.73	-79.04	8.13	1	No
	3	5.502	120.43	-82.85	-9.29	0	No
	4	15.638	114.69	-89.98	-3.97	0	No
	5	8.456	105.85	81.78	-10.76	0	No
Supershear Initiation Model	1	9.212	117.53	-86.77	8.28	1	YES
	2	9.814	123.93	-77.01	6.13	1	No
	3	5.530	121.58	-81.26	-10.61	0	No
	4	15.638	114.51	89.85	-4.71	0	No
	5	8.456	105.76	81.81	-11.55	0	No
Roughness Model	1	8.974	115.59	-87.91	9.82	1	YES
	2	9.240	121.12	-79.99	7.17	1	No
	3	5.810	117.18	-85.94	-8.72	0	No
	4	15.638	116.44	-86.89	-6.53	0	No
	5	8.708	105.61	82.20	-12.74	0	No
Heterogeneous D_c Model	1	9.184	118.79	-88.73	10.48	1	YES
	2	10.234	124.68	-80.55	7.31	1	No
	3	5.726	121.19	-85.80	-7.98	0	No
	4	15.638	118.00	-89.62	-3.39	0	No
	5	8.820	109.46	82.21	-11.41	0	No
Heterogeneous μ_d Model	1	9.044	117.44	-86.39	7.94	1	YES
	2	4.004	126.23	-69.08	1.71	1	No
	3	11.662	123.32	-77.56	7.74	1	No
	4	5.502	120.30	-82.62	-12.94	0	No
	5	8.204	105.88	82.30	-14.16	0	No
Waviness Model	1	9.184	101.06	88.18	10.09	1	YES
	2	11.270	109.13	-79.83	7.05	1	No
	3	5.768	102.55	89.97	-5.38	0	No
	4	8.736	94.17	81.08	-8.90	0	No
	5	15.638	99.04	85.93	-1.62	0	No
ESM Data	1	9.758	77.14	-65.61	-0.22	0	No
	2	13.475	77.04	-67.20	0.61	1	YES
	3	6.566	77.01	-67.02	-10.51	0	No
	4	15.295	77.03	-66.50	-0.85	0	No
	5	4.837	77.12	-67.68	-21.36	0	No

Table S11. Properties of the five candidate pulses for station 3142 for the six dynamic rupture models shown in the main text and the ESM data. T_p is the period, PGV is the peak ground velocity of the original rotated signal, and Rot. Angle is the corresponding angle by which the signal is rotated. PI is the pulse indicator, and Is-Pulse shows a candidate classified as a pulse when = 1 and not a pulse when = 0. 'Chosen' depicts which candidate is the chosen pulse. The details of the coefficients for each candidate can be seen in the Supplementary Excel File S1 included in the Zenodo repository.

Model	D_{NPF}	$\mathrm{Families}_{(\mathrm{NPF})}$	D_{EAF}	$\mathrm{Families}_{(\mathrm{EAF})}$	D_c Range	Background	$\mathrm{Avg}_{(\mathrm{NPF})}$	$\mathrm{Avg}_{(\mathrm{EAF})}$	M_w
Model 4	1.12	7	1.52	8	0.2–0.9	1	0.5	0.5	7.860
R1	1.10	7	1.90	7	0.2–0.9	1	0.5	0.5	7.859
R2	2.17	5	2.5	6	0.2–0.9	2	0.7	0.7	7.859
R3	2	5	1.85	7	0.1–1.5	1	0.7	0.7	7.861
R4	2.07	5	2.44	6	0.2–0.9	2	0.8	0.8	7.859

Table S12. Parameters of the supplementary heterogeneous D_c models following Ide and Aochi (2005), including the D value and the number of families along the NPF and EAF, the range of D_c values, the background D_c value, the average D_c values for the NPF and EAF, and the resulting moment magnitude, M_w, of the simulated seismic event.